

Differential Optical Absorption Spectroscopy of Trace Gas Species and Aerosols in the
Upper Ohio River Valley

Dissertation

Presented in Partial Fulfillment of the Requirements for the Degree Doctor of Philosophy
in the Graduate School of The Ohio State University

By

Christopher Paul Beekman, B.S.

Environmental Science Graduate Program

The Ohio State University

2010

Dissertation Committee:

Heather C. Allen, Advisor

Catherine A. Calder

Bryan G. Mark

Franklin W. Schwartz

Copyright by
Christopher P. Beekman
2010

Abstract

In this research, it is hypothesized that recently developed theoretical considerations of atmospheric radiative transfer in horizontally in-homogeneous atmospheres can be applied to the remote measurement of anthropogenic plumes. To this end, a MAX-DOAS spectrometer, designed around a B&W-TEK BTU142 spectrometer was constructed and characterized. It was found that the MAX-DOAS spectrometer has a measured resolution of 0.282 nm, and a noise level of 178 counts at 75% pixel saturation, sufficient to resolve accurately the absorptions of important atmospheric species, including SO₂, NO₂, HCHO, and O₄. The theory of MAX-DOAS spectral analysis was examined in detail, in particular the processing of reference absorption cross-section spectra for use in regression analyses of scattered solar radiation. For the purposes of inversion, optimal estimation software was designed and investigated for suitability in retrieving vertical profiles of atmospheric species. This software is shown to perform well under conditions of both typical and non-typical noise levels using synthetic spectral data and known profiles of three atmospheric species. Furthermore, an extensive examination of the residuals of DOAS spectral analysis was performed, to validate the assumption of normally distributed errors in the inversion process. Investigated methodologies were applied to spectral data collected over nine days in 2008 in the Upper Ohio River Valley. Aerosol extinction coefficient profiles were successfully retrieved, with an average peak value of 0.549 km⁻¹. For the same measurement period, in-plume measurements of SO₂ and NO₂ concentration from a coal-fired power plant were conducted using recently developed methodologies to account for in-plume solar radiative transfer effects.

Dedication

Dedicated to my wife, Gina, who has been a bottomless well of love and patience, and to my son, Troy Benjamin, for providing me with all the motivation I could ever need.

Acknowledgements

My sincerest thanks to Dr. Catherine A. Calder and Dr. Radu Herbei of the Statistics Department of The Ohio State University, for their input and attention to detail concerning the spectral analysis portion of this research and the development of the Markov Chain Monte Carlo inversion of atmospheric profiles, the subject of a future paper. Additionally, I thank Gerald Allen and Dr. Franklin Schwartz for their assistance in the mapping portions of this dissertation.

Vita

1998.....Shadyside High School
2002.....B.S. Chemistry and Environmental Science,
Muskingum College
2004 to present.....Graduate Teaching Associate,
Department of Chemistry, The Ohio State University

Publications

L. F. Voss, M. F. Bazerbashi, C. P. Beekman, C. M. Hadad, and H. C. Allen, "Oxidation of oleic acid at air/liquid interfaces." *Journal of Geophysical Research-Atmospheres*, 112, 2007.

C. P. Beekman and William J. Mitsch, "Soil Characteristics in a bottomland hardwood forest five years after hydrologic restoration." *William H. Schiermeier Olentangy River Wetland Research Park at The Ohio State University Annual Report 2005, 2006.*

Fields of Study

Major Field: Environmental Science Graduate Program

Table of Contents

Abstract.....	ii
Dedication.....	iii
Acknowledgements.....	iv
Vita.....	v
List of Figures.....	x
List of Tables.....	xix
Chapter 1: Introduction.....	1
Chapter 2: Important Tropospheric Chemistries.....	7
2.1: Introduction to Relevant Tropospheric Chemistry.....	7
2.2: The HO _x , NO _x , and O ₃ cycles.....	7
2.3: Tropospheric Formaldehyde.....	11
2.4: Sulfur Dioxide Chemistry.....	12
Chapter 3: Structure and Physics of the Atmosphere.....	16
3.1: Introduction to Atmospheric Structure and Physics.....	16
3.2: Delineation of Atmospheric Regions.....	16
3.3: Solar Radiation and Radiative Transfer.....	20

3.4: Mathematical Description of Atmospheric Scattering.....	22
3.5: Absorption by Atmospheric Gases.....	24
3.6: Radiative Transfer Modeling.....	25
3.6a: MCARaTS.....	26
3.6b: SCIATRAN.....	27
Chapter 4: Instrumentation.....	29
4.1: Introduction.....	29
4.2: Instrument Components and Construction.....	29
4.3: Instrument Function.....	31
4.4: Electronic Offset.....	33
4.5: Dark Current.....	36
4.6: Noise Considerations.....	38
Chapter 5: Spectral Analysis.....	41
5.1: Introduction: Principles of Differential Optical Absorption Spectroscopy...	41
5.2: Species Measurable by Differential Techniques.....	47
5.3: Analysis Window Selection.....	51
5.4: Processing of Absorption Cross-section Spectra.....	55
5.4a: Recording of spectral data by spectrophotometers.....	56
5.4b: Convolution with the instrument function.....	60
5.4c: Spline to grid of spectrometer.....	66
5.4d: Absorption cross-section processing in practice.....	70
5.5: Determination of Optical Depth.....	73
5.6: Determination of Differential Optical Depth.....	75

5.7: Determination of Differential Absorption Cross-Sections.....	78
5.8: Least-squares Regression to Derive Concentration or Slant Column Density.....	80
5.9: Least-squares Regression with Calibration Correction.....	89
5.10: The Ring Effect.....	98
5.11: Concluding Remarks on DOAS Data Analysis.....	98
5.12: Summary of Methodology: Spectral Analysis.....	100
Chapter 6: Profile and Concentration Retrieval of Atmospheric Species.....	109
6.1: Slant Column Density.....	109
6.2: Classical (geometric) Air Mass Factors.....	111
6.3: Layer Air Mass Factors.....	113
6.4: Statistical Inversion, Maximum A-posteriori Solution.....	117
6.4a: Mathematical Description.....	117
6.4b: Noise Consideration in Profile Inversion.....	120
6.4c: Inversion of Synthetic Data.....	127
Chapter 7: Aerosol Extinction Profiles and Trace Gas Concentrations in the Ohio River Valley.....	140
7.1: Introduction.....	140
7.2: Aerosol Optical Properties and Prior Profile Determination.....	143
7.3: DOAS Analysis of O ₄	148
7.4: Inversion of Aerosol Extinction Coefficient Profiles.....	149
7.5: Conclusions, Aerosol Extinction Coefficient Inversion.....	155
7.6: DOAS Analysis of SO ₂ , NO ₂ , and HCHO.....	159

7.6a: SO ₂ Fitting Window.....	159
7.6b: NO ₂ Fitting Window.....	160
7.6c: HCHO Fitting Window.....	160
7.7: Gaussian Plume Modeling of NO ₂ and SO ₂	161
7.8: Radiative Transfer Modeling of NO ₂ and SO ₂ Air Mass Factors.....	163
7.9: Plume Mixing Ratios, NO ₂ and SO ₂	166
7.10: Formaldehyde.....	170
Chapter 8: Summary and Conclusions.....	173
8.1: Summary.....	173
8.2: Recommendations for Future Work.....	176
References.....	179

List of Figures

Figure 3.1: Vertical profiles of atmospheric temperature and pressure, shown with atmospheric layers as delineated by temperature. Data from the U.S. Standard Atmosphere, 1976.....	19
Figure 4.1: Multi-Axis Differential Optical Absorption Spectrometer used in this research.....	31
Figure 4.2: Emission line of a mercury vapor penlamp at 334 nm, measured with a differential optical absorption spectrometer, shown with a Lorentzian lineshape. FWHM is 0.282 nm.....	33
Figure 4.3: Electronic offset for the BWTEK spectrometer used in this research. Offset was recorded from 10,000 spectra using a 6 ms integration time, with no light reaching the detector.....	35
Figure 4.4: Dark current correction for the BWTEK spectrometer recorded with no light reaching the detector, using a 60 second integration time.....	37
Figure 4.5: Root mean squared error of the B&W-TEK spectrometer used in this research. The total noise was calculated as the root mean squared error of thirty spectra of an Ocean Optics deuterium-tungsten light source, Mini-D2T.	39
Figure 5.1: An absorption band shown as a departure from the true $I_0(\lambda)$ as in laboratory spectroscopy and as a departure from $I'_0(\lambda)$, as in differential spectroscopy.....	43

Figure 5.2: Pre-processing of both collected atmospheric intensities (left) and reference absorption cross-sections (right), shown with references to relevant sections of this document. The necessary output for subsequent analysis procedures are the design matrix A, data matrix B, the wavelength pixel mapping function for the j species to be analyzed, as well as the convolved reference absorption cross-sections with their original wavelength grids. 46

Figure 5.3: Absolute absorption cross-section of nitric acid. The lack of peaked structure necessary for differential analysis is clearly evident. 48

Figure 5.4: Absolute and differential absorption of NO_2 . Two strong differential features are indicated by the arrows. 49

Figure 5.5: Differential absorption cross-sections of 10 species commonly found in DOAS analysis. The spectra were taken from: NO^{37} , NO_2^{38} , HONO^{39} , SO_2^{40} , HCHO^{41} , Benzene⁴², ClO^{43} , BrO^{44} , O_3^{45} , and O_4^{46} 51

Figure 5.6: Attenuation of the solar spectrum during collection and pixelation by a spectrophotometer 58

Figure 5.7: Convolution of the absorption cross-section of NO_2 by the instrument function of a DOAS spectrophotometer. In this case, the convolution was implemented by multiplication in the frequency domain. 64

Figure 5.8: Convolution of a spectral line with low and high resolution Gaussian instrument functions. In trace a , a spectral line is convolved with the instrument function of the DOAS instrument, with full-width at half maximum 0.8 nm. b shows the convolution of the same spectral line with a theoretical instrument function of full-width at half maximum 0.2 nm. c demonstrates the convolution of the product in b with the

lower resolution instrument function of a . It can be seen that the product of c is identical to the product of a . Thus, the instrument function of the high resolution spectrum does not need to be removed prior to convolution. 65

Figure 5.9: Results of a cubic spline interpolation of the high resolution NO₂ absorption cross-section to the wavelength grid of a lower resolution DOAS spectrometer. Traces a and b show the original spectrum plotted as discrete data points and as a continuous spectrum, respectively. Traces c and d show the spectrum after a cubic spline interpolation to the relatively rough grid of the DOAS instrument, as discrete data points and as a continuous spectrum, respectively. The reduction in information content between traces a and c is clearly visible. 67

Figure 5.10: Differential absorption cross-section of NO₂ collected by a low-resolution DOAS spectrometer (blue trace) and a spectrum processed from a high resolution spectrum after convolution and cubic spline interpolation (red trace). For comparison, a 4th order polynomial, representing the broad-band instrument function of each instrument, has been removed from both spectra. The slight differences can be attributed to variations in calibration between the two instruments, and can be corrected in the fitting process. 72

Figure 5.11: Optical depth spectrum, collected on August 14, 2007. The spectrum shown here represents the natural log of I_0 and I , a Fraunhofer reference spectrum and off axis spectrum, respectively, shown in the inset, according to the Beer-Lambert Law. The strong overall slant of the optical depth spectrum is the result of Rayleigh and Mie scattering, as well as the slowly varying components of atmospheric absorbers. It is this

slowly varying trend that must be separated prior to least squares analysis to determine concentrations or slant column densities. 74

Figure 5.12: Broad-band component of an optical depth spectrum, determined by three methods. The top row of traces show the slowly varying component of the optical depth spectrum, determined by least squares regression of a 4th order polynomial, a moving average smoothed optical depth spectrum, and a Bartlett (triangular) windowing smooth. Below each function is the differential optical depth, calculated as the difference between the optical depth and the respective slowly varying function. Although minor differences are present in each of the three differential absorption spectra, these are largely confined to the end regions. 77

Figure 5.13: The differential absorption cross-section of NO₂. A polynomial of 4th order (blue trace) was fit by linear least squares regression to the absolute absorption cross-section of NO₂ (red trace). Subtraction of this polynomial, representative of the broad-band absorption features as well as the instrumental effects, yields the desired differential absorption cross-section. 79

Figure 5.2: Pre-processing of both collected atmospheric intensities (left) and reference absorption cross-sections (right), shown with references to relevant sections of this document. The necessary output for subsequent analysis procedures are the design matrix A, data matrix B, the wavelength pixel mapping function for the j species to be analyzed, as well as the convolved reference absorption cross-sections with their original wavelength grids. 81

Figure 5.14: The derivation of differential optical depth from measured intensity spectra. 85

Figure 5.15: Construction of design matrix A , for least squares analysis. The matrix is composed of the convolved, interpolated differential absorption cross-sections of NO_2 , O_4 , and a synthetic Ring spectrum..... 86

Figure 5.16: Measured and modeled differential optical depth spectra. The modeled spectrum was obtained through a linear least squares regression of NO_2 , O_4 , and a synthetic Ring spectrum to a measured differential optical depth spectra. Residuals (lower trace) were calculated as the difference between the measured and modeled spectra. For this wavelength interval, where NO_2 is the primary absorber of solar radiation as discussed in Section 5.3, the residuals are unlikely to be the result of the exclusion of an absorbing species from the design matrix²⁷. The cause of these relatively large residuals is likely due to slight misalignments between the measured data and the reference differential absorption cross-sections and the incomplete removal of solar features, a common problem in the analysis of solar spectroscopic data. This misalignment was illustrated previously in Figure 5.9. 88

Figure 5.17: NO_2 differential cross-section with altered wavelength pixel mapping functions. Altering the wavelength pixel mapping functions can shift, stretch, and squeeze a spectrum, analogous to changing the wavelength calibration of an instrument. The spectra shown were calculated by first altering the wavelength pixel mapping function as shown, then interpolated by cubic spline to the wavelength grid of the DOAS spectrophotometer..... 93

Figure 5.18: Logic flow for a typical DOAS analysis including correction for wavelength misalignment. The process of determining wavelength pixel mapping coefficients is

performed as a separate step from the linear least squares analysis to determine concentrations, in accordance with the Beer-Lambert Law of absorption.	94
Figure 5.19: Analysis of a differential optical depth spectrum with and without correction for wavelength misalignment. The improvement in the magnitude of the residuals is clearly visible, although the improvement is modest.....	96
Figure 5.2: Pre-processing of both collected atmospheric intensities (left) and reference absorption cross-sections (right), shown with references to relevant sections of this document. The necessary output for subsequent analysis procedures are the design matrix A, data matrix B, the wavelength pixel mapping function for the j species to be analyzed, as well as the convolved reference absorption cross-sections with their original wavelength grids.	101
Figure 5.20: Least squares regression analysis of collected differential optical depth spectrum to derive individual slant column densities for the j th species included in the regression model.	104
Figure 5.21: Regression analysis, including iterative calibration procedure.	106
Figure 6.1: Flow-diagram of interpretation of scattered solar radiation data.	111
Figure 6.2: Geometries of ground-based MAX-DOAS, considering the single scattering case for an absorber located in the stratosphere (Top) and for an absorber in the troposphere (Bottom).	112
Figure 6.3: Schematic of the Layer Air Mass Factor concept with discrete vertical layers of the atmosphere indicated as Layer 1, 2, and 3, with concentrations c_1 , c_2 and c_3 , within each layer, respectively.....	115
Figure 6.4: Histograms of the residuals from the MAX-DOAS analysis of NO ₂	123

Figure 6.5: Histogram of the full NO ₂ analysis for the July 16, 2008 data set.	124
Figure 6.6: Amplitudes of Fourier Transformed synthetic white noise, the residuals resulting from a DOAS analysis of NO ₂ from the July 16, 2008 data set, and a synthetic absorption spectra.	126
Figure 6.7: NO ₂ , HCHO, and ozone profiles used to generate synthetic MAX-DOAS data. The synthetic differential optical depth spectra for the 2.5° line of sight is also shown in the lower two traces, both before and after addition of random noise.	128
Figure 6.8: A-priori profiles for each of the three species included in the retrieval. Also shown in the figures (light gray traces) are the upper and lower boundaries of the climatology used here. These traces represent the first standard deviation for each species.	130
Figure 6.9: True, a-priori, and retrieved profiles retrieved from synthetic differential optical depth spectra with a small degree of Gaussian noise, mean zero, standard deviation 0.000035.	131
Figure 6.10: Percent difference between the true and retrieved profiles inverted from synthetic spectral data with a small degree of added white noise.	132
Figure 6.11: Retrieved differential optical depths resulting from the inversion of synthetic data with a small degree of added Gaussian noise, shown with the corresponding measured synthetic data, at the 2.5° and 20° lines of sight.	134
Figure 6.12: True, a-priori, and retrieved profiles resulting from the inversion of synthetic spectral data to which a higher degree of Gaussian noise has been added.	135
Figure 6.13: Percent difference between the true and retrieved profiles to 12 km, for synthetic spectral data to which a higher degree of Gaussian noise has been added.	136

Figure 6.14: Retrieved differential optical depths to which a high degree of Gaussian noise has been added, for the 2.5° and 20° lines of sight.	137
Figure 7.1: Topographic map of the study area. Blue dots represent the two sampling locations, where the MAX-DOAS instrument was deployed. Red dots represent coal fired power plants.	141
Figure 7.2: Aerosol extinction coefficient profile as derived from Gaussian plume model AERMOD and scaled to previously measured optical properties of aerosols in the Ohio River Valley.	147
Figure 7.3: Aerosol extinction coefficient profiles for September 17, 2008. The peak value of each profile is shown in the upper right corner of each trace. The profiles are inverted from O ₄ absorption spectra collected at viewing angles 2.5°, 5°, 7°, 10°, and 15°.	150
Figure 7.4: Aerosol extinction coefficient profiles for September 18, 2008. The peak value of each profile is shown in the upper right corner of each trace. The profiles are inverted from O ₄ absorption spectra collected at viewing angles 2.5°, 5°, 7°, 10°, and 15°.	150
Figure 7.5: Aerosol extinction coefficient profiles for September 19, 2008. The peak value of each profile is shown in the upper right corner of each trace. The profiles are inverted from O ₄ absorption spectra collected at viewing angles 2.5°, 5°, 7°, 10°, and 15°.	151
Figure 7.6: Averaging kernels for the first seven altitudes used in inversion of aerosol extinction coefficients for September 17, 2008, at 1:14 PM.	152

Figure 7.7: Measured and modeled O₄ differential optical depth spectra. The modeled data is a result of a forward model (F(x)) run using the retrieved profile of aerosol extinction at 350 nm for September 17, 2008 at 1:14 PM. 154

Figure 7.8: Average aerosol extinction coefficient profile for the entire September 2008 collection period. Error bars represent the standard deviation of the data set. The aerosol profile shown here was used for all subsequent radiative transfer applications in this research 155

Figure 7.9: Aerosol extinction coefficient (km⁻¹) plotted with relative humidity values. 157

Figure 7.10: Example of the analysis of SO₂ from the WinDOAS analysis software from the July 16, 2008 collection period. 160

Figure 7.11: NO₂ and SO₂ profiles generated from the EPA Gaussian Plume model AERMOD and compiled from the highest 3-hour averages for the month of July, 2008. 163

Figure 7.12: Cross-sectional view of the NO₂ plume as specified in the three-dimensional grid of the MCARaTS radiative transfer model as a perturbation to the horizontally homogeneous atmosphere. 164

Figure 7.13: Peak mixing ratios of NO₂ determined from measured slant column densities. Error bars indicate the Root Mean Squared Error of the regression. 167

Figure 7.14: Peak mixing ratios of SO₂ determined from measured slant column densities. Error bars indicate the Root Mean Squared error of the regression. 168

List of Tables

Table 5.1: Wavelength windows of common analytes used in past differential optical absorption studies.....	54
--	----

CHAPTER 1: INTRODUCTION

Multi-Axis Differential Optical Absorption Spectroscopy, or MAX-DOAS, is an extension of the well-known zenith (upward looking) collection of scattered solar radiation remote sensing method¹. In a Multi-Axis collection configuration, scattered solar radiation is collected not only pointing to the zenith, but also at off-axis angles relative to the horizon. As the majority of atmospheric scattering occurs in the lowest few kilometers of the troposphere, MAX-DOAS methods are especially sensitive to boundary layer species. This enhanced sensitivity to tropospheric species was first noted in 1993 during twilight measurements of OCIO in Antarctica². MAX-DOAS measurements can be accomplished with relatively simple instruments, consisting of a light collection device, angular pointing mechanism, and a UV-visible spectrometer of moderate (~1 nm) resolution. The information which can be collected with MAX-DOAS instruments represents an intermediate-scale measurement, between that of point monitoring methods and those measurements taken by satellites, with spatial resolutions of tens of kilometers. While it is difficult to define the horizontal resolution of MAX-DOAS measurements, rough estimates based on aerosol-limited visibility calculated using the aerosol model OPAC place this resolution between 10 and 25 km, although consideration for different wavelengths and measurement geometries must also be given.

MAX-DOAS measurements collected at different elevation angles contain information on the vertical distribution of atmospheric gases and aerosols¹. These measurements can be coupled to a model of atmospheric radiative transfer and, using statistical methods of inversion, be used to retrieve the vertical profiles of trace gas and aerosol species^{3,4}. Additionally, using assumed or realistic profiles of the species of interest, MAX-DOAS data can be efficiently converted to atmospheric vertical columns, and, in some cases, concentration. The ability to retrieve the vertical distribution of trace gases and aerosols is a significant aspect of the method, as spatially resolved information is typically unobtainable using conventional, point monitoring techniques. These point monitoring techniques, often collected at ground level, are important in understanding the impacts of emissions and pollution on human health, but provide little to no information on processes and emissions above ground level. Additionally, there are relatively few techniques that can provide vertically resolved information from a ground-based platform. Other methodologies, such as airplane or balloon soundings using conventional instrumentation modified for above-ground sampling, have been used to obtain similar profile information, but entail significant expense compared to the relatively inexpensive instrumentation necessary for MAX-DOAS methodologies. The high degree of expertise and maintenance required for balloon or airplane based soundings and the limitations of the vehicles themselves serve to limit the temporal resolution of these methodologies, compared to MAX-DOAS methods, which can obtain a full series of angular measurements necessary to retrieve a single profile in 15 to 30 minutes time. If only a single observation angle is necessary, temporal resolution could theoretically be on the

order of a minute or less, limited by the absorption signal strength of the species of interest and the capabilities of the spectrometer itself.

An under-represented application of the MAX-DOAS methodology is the ability to monitor isolated plumes, for example, those emitted from natural sources, such as volcanoes, and anthropogenic sources, such as industrial stacks. The technique has been implemented on a limited basis to the study of volcanic plumes, but as of this writing, only a single example can be found in the literature concerning the monitoring of an emissions plume from an industrial source^{5,6}. As both SO₂ and NO₂, major atmospheric pollutants emitted in large amounts by coal-fired power plants, can be resolved with MAX-DOAS, a major goal of this research is the extension of the method for this purpose. In addition, the vertical distribution of aerosol extinction can be extracted from the absorption signature of O₄^{1,7}. From these data, a relatively comprehensive picture of regional atmospheric conditions can be determined with only a single instrument. The ability to monitor in plume concentrations of pollutant species is a significant improvement to traditional ground based monitoring methods, as conducted by environmental regulatory agencies, as these methods provide only the ground level concentration of a particular species. While important in regards to human health, such methods cannot predict the impacts of emissions downwind of the emission point, whereas in-plume measurements can.

Two of the target species in this research, SO₂ and NO₂, have important implications to not only regional atmospheric chemistries, but also impact significantly areas well outside of their emission point due to long range transport. For example, some estimates of acid deposition (primarily SO₄²⁻) in the Mid-Atlantic region, by back

trajectory analysis, attribute 37% to emission sources in the Ohio River Valley⁸. Long range transport of NO_x species, considered precursors to ozone, from the same region, have been shown to impact the concentration of ozone significantly in the Mid-Atlantic region, and have been estimated to contribute 49% of ozone transport to this region⁹. MAX-DOAS measurements, combined with wind speed data and models of atmospheric dispersion, can provide estimates of emissions from single sources with a high level of temporal resolution. Such information has the potential to be invaluable in correlating large-scale modeling of pollutant transport with downwind observations.

Equally important as the measurement of emitted trace gas species within a plume is the ability to derive information on the vertical distribution of aerosols from the absorption signature of the O₄ species. Aerosols, which vary drastically their composition and optical properties both regionally and temporally, represent the largest source of uncertainty in climate change models¹⁰. Regional measurements of aerosols by MAX-DOAS methods could provide a significant improvement to these uncertainties. The relatively simple nature of the instrument itself would lend itself to large-scale networks of aerosol monitoring instruments. Extraction of aerosol distributions from scattered sunlight spectra, however, is not a simple matter, requiring sophisticated statistical inversions methods and well-characterized estimates of the aerosol distribution and optical properties beforehand. To this end, the use of dispersion models and prior measurements of aerosol composition and concentration for this purpose were examined in this research.

In this research, a MAX-DOAS spectrometer was constructed, characterized, and deployed in the Upper Ohio River Valley, a region well known for industrial activity and

atmospheric air pollution, for nine days in the summer of 2008, spanning the months of July, August, and September. From the data collected during this time period, vertical profiles of aerosols were retrieved using optimal Bayesian estimation methods, and the mixing ratios of SO₂ and NO₂ within a power plant plume were determined.

It is hypothesized in this research that application of newly proposed theoretical methods of radiative transfer in horizontally inhomogeneous atmospheres, specifically volcanic plumes¹¹, can be applied to the monitoring of an anthropogenic plume emitted from a coal-fired power plant. Also hypothesized is that interpretation of MAX-DOAS data collected near to an emissions source can be interpreted and correlated with the output of a sophisticated Gaussian plume model. It is anticipated that the marriage of these techniques will aid significantly in the development of MAX-DOAS as a regulatory tool, providing information on above-ground plumes which cannot be gathered easily using conventional point monitoring techniques. Such measures are significant in their ability to provide information on the long-range transport and downwind impacts of such industrial plumes. In this dissertation, the scientific phenomenon relevant to MAX-DOAS measurements and their interpretation are presented. Additionally, instrumentation and analysis procedures performed in the collection and analysis of spectral data collected in the Upper Ohio River Valley are described. Chapter 2 details important tropospheric chemistries, focusing in large part on chemical cycles involving SO₂ and NO₂, the primary target species of this work. Chapter 3 presents the structure and physics of the atmosphere, which is important in the modeling of atmospheric radiative transfer, a necessary process for the proper interpretation of measured scattered solar radiation. The MAX-DOAS instrument used in this research is described in

Chapter 4, including details on the characterization of the instruments resolution and noise. Spectral analysis of scattered solar radiation is presented in Chapter 5, examining the conditioning of both measured spectral data and regression analysis. Interpretation of data generated by the spectral analysis procedures of Chapter 5, including the role of atmospheric radiative transfer models in the processing of MAX-DOAS data and the retrieval of vertical profiles, are given in Chapter 6. Results of the field study in the Upper Ohio River Valley are presented in Chapter 7.

CHAPTER 2: IMPORTANT TROPOSPHERIC CHEMISTRIES

2.1 Introduction to Relevant Tropospheric Chemistry

This chapter will focus on the most important and well-known atmospheric chemical processes relevant to this research, as the targeted species undergo chemical transformations, which determine their ultimate fate in the atmosphere. In addition to being the most important atmospheric chemical cycles for this research, those reviewed in this chapter involve chemical species with sufficient concentrations and structure in their UV-visible absorption cross-sections to be detected by scattered sunlight DOAS instruments. The temperature inversion of the stratosphere serves to constrain vertical mixing and exchange of gaseous molecules between the troposphere and stratosphere. A vast array of geochemical and anthropogenic emissions from the surface of the Earth is vertically mixed within the troposphere. The troposphere, although well shielded from the most energetic wavelengths of incoming solar radiation, receives sufficient solar radiation energies to enable photochemistry to occur. As such, the chemical cycles of the troposphere are unique and many. In large part, the chemistry of the troposphere is oxidation involving fast radical reactions.

2.2 The HO_x, NO_x, and O₃ Cycles

The primary oxidant of the troposphere is the hydroxyl radical, OH. This species reacts rapidly with most reduced non-radical species and is able to react quickly with

hydrocarbons by abstraction of H atoms to produce H₂O. Production of OH radical proceeds by the following reactions¹²:



Photolytic production of $O(^1D)$ occurs within the narrow wavelength region 300 to 320 nm, and was, prior to the 1970's, thought to occur with such low frequency due to the high degree of absorption by the stratospheric ozone layer that oxidation by the OH radical was thought to be negligible. Although still a subject of some debate, the global mean concentration of hydroxyl radical is thought to be $\sim 1.0 \times 10^6$ molecules cm^{-3} . The hydroxyl radical, although measurable only by high intensity, high resolution long-path instruments¹³, is considered the most important oxidant in the troposphere, and is of primary importance to many of the chemical cycles reviewed here¹⁴.

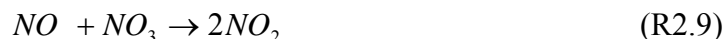
It is not surprising that oxides of nitrogen, the most abundant gaseous species in the atmosphere, play an important role in tropospheric (and stratospheric) chemistry. Oxides of nitrogen occur in both polluted regions as a by-product of combustion, and in remote atmospheres due to the action of lightning, volcanic activity, and naturally occurring fires. Nitrogen-oxides are frequently grouped under the terms NO_x and NO_y . NO_x is defined as both NO and NO_2 , and NO_y is defined as NO_x and its reservoir species, including N_2O_5 and HNO_3 . Of primary importance in the troposphere is the photolysis of NO_2 and the production of ozone. The cycle begins with the photolysis of NO_2 at wavelengths below 424 nm¹⁵:



where M is any third body that absorbs excess vibration energy and stabilizes the newly formed O₃ molecule. O₃ can go on to react with NO to regenerate NO₂ and O₂ by the reaction¹⁵:



In addition to these three primary reactions, several other reactions occur in the NO_x cycle, including the reservoir species HNO₃ and NO₂. These reactions are as follows¹⁵:



All of the above reactions occur in both remote and polluted regions, but additional reactions must be included to explain deviations from the photo-stationary state.

Consider a polluted atmosphere, where fossil fuel combustion enhances not only NO_x concentrations but also the concentrations of hydrocarbons, RH, through incomplete fuel combustion. In this case, not only must the NO_x/ozone cycle be considered, but also the oxidation of RH species by the hydroxyl radical. RH oxidation produces RO₂ and HO₂, which in turn can produce NO₂ without destroying O₃. Thus, the presence of RH in

sufficient concentrations allows for the concentration of O₃ to increase beyond typical background concentration of 30 ppb. In polluted, particularly urban, regions, the photochemical reactions presented here are frequently referred to as the “photochemical smog cycle”, a phenomenon that, in some areas, maintains the concentration of O₃ at or above 80 ppb for extended periods of time. As such, this is considered a serious health and environmental problem, O₃ being toxic to both plant and animal life.

The enhanced O₃ production described above is initiated by the photolysis of ozone and the production of hydroxyl radical, by Reactions 2.1 – 2.3. Under conditions of elevated hydrocarbon concentration, the abstraction of an H atom by the hydroxyl radical yields water and RO₂ radical by¹²:



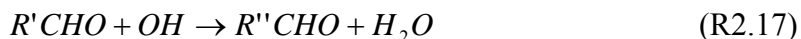
The resultant RO₂, or peroxy radical, can react with NO to produce NO₂ by the following¹²:



NO₂ produced by this reaction can go on to produce O₃ by Reactions 2.4 and 2.5. The RO radical produced can undergo several reactions, but the usual case is the formation of carbonyl species and the HO₂ radical, by the following reactions¹²:



The resultant R'CHO can undergo several reactions, including reaction with hydroxyl radical or photolysis¹²:





HO₂ radical produced by Reactions 2.15 and 2.18 can react with NO as per Reaction 2.16 to produce further hydroxyl radical. In remote regions, where NO_x concentrations are relatively low, HO₂ radical typically self reacts to produce H₂O₂ and O₂, terminating the HO_x cycle¹⁴. In polluted regions, where NO_x concentrations are high, the HO_x cycle is terminated typically by the reaction of NO₂ with hydroxyl radical¹²:



The reactions detailed here are of primary importance to this research, and comprise a great proportion of typical tropospheric chemistries. The reactions involving the generic hydrocarbon RH are extended in Section 2.3 to the species formaldehyde, HCHO.

2.3 Tropospheric Formaldehyde

The treatment of organic molecules in the production of tropospheric ozone detailed above will be extended for the trace gas formaldehyde, as this species has several strong absorption bands in the UV-visible region, and is quite easily monitored by typical MAX-DOAS instruments, and is the most common atmospheric aldehyde, ranging in concentration from 100 ppt in remote regions to 45 ppb in polluted cities¹⁶. The reactions of formaldehyde are also critical in understanding and tracking of polluted air masses using CO as a tracer, as HCHO is a source of atmospheric CO. As such, the formaldehyde molecule is an important species in understanding global carbon cycles. Formaldehyde is both emitted from anthropogenic sources such as incomplete combustion, and is also a product of the oxidation of atmospheric hydrocarbons. The

formaldehyde molecule undergoes both photolysis and reaction with the hydroxyl radical by the following¹⁵:



The HO_x cycle is extended by the reaction of H radical with O₂ to form HO₂ radical, as does the HCO radical. CO produced by the photolysis of HCHO can undergo further reaction with the hydroxyl radical to produce CO₂ via¹⁵:



and is therefore a critical reaction in understanding global climate change.

2.4 Sulfur Dioxide Chemistry

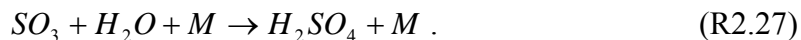
Sulfur dioxide (SO₂) is a by-product of coal and diesel combustion. It has a strong absorption spectrum below ~300 nm, and can, in some circumstances, be monitored by remote sensing techniques. In this research, the weaker absorption bands above 305 nm are probed. The oxidation of SO₂ is an important cycle leading to the formation of sulfate aerosols and contributing to the lowering of the pH of rainwater, commonly known as acid rain. The primary route of gas phase SO₂ oxidation is reaction with the hydroxyl radical via the reaction¹⁴:



followed by further oxidation to sulfite via¹⁴:

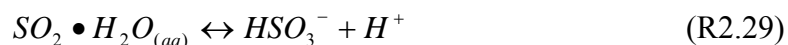


Sulfite can then rapidly react to form sulfuric acid by¹⁴:



The average lifetime of SO₂ is approximately one week based on the reaction with the hydroxyl radical, but this lifetime is further decreased by deposition mechanisms. In addition to these gas phase reactions, oxides of sulfur participate in a variety of heterogeneous chemistries involved in aerosol formation and growth¹⁴.

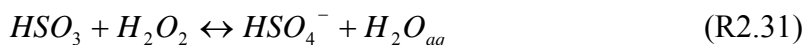
Gas-phase SO₂ is readily dissolved in liquid water, a phenomenon that leads to a rich variety of oxidation reactions with other atmospheric species in the aerosol/aqueous phase. This high solubility leads to the greater importance of heterogeneous SO₂ oxidation relative to oxidation in the gas phase. Dissolved SO₂ forms different chemical species through several aqueous phase equilibrium reactions. For simplicity of notation, these species are typically indicated simply by S(IV), for sulfur species in the 4+ oxidation state. Sulfur species with the 4+ oxidation state include SO₂*H₂O, HSO₃⁻¹, and SO₃⁻². Giving rise to these species are the following aqueous equilibrium reactions¹⁴:



Once incorporated into the aqueous phase of a droplet or aerosol, S(IV) can undergo oxidation reactions with co-dissolved atmospheric species. This includes metal-catalyzed oxidation with O₂, reaction with nitrogen oxides or ozone, and oxidation by reaction with H₂O₂ or organic peroxides. It is not the aim of this thesis to present a full treatment of these various oxidation processes, especially when the relative importance of the chemistry of several of these processes in the real atmosphere is considered. Over the

acidic pH range found in typical atmospheric aerosols, the oxidation of S(IV) by H₂O₂ is the dominant reaction, the rate of which is fairly constant over this pH range¹⁴. Therefore, only the oxidation by peroxides will be detailed here.

Aqueous aerosol phase oxidation of S(IV) by peroxides is an important phenomenon in tropospheric aerosol chemistry, as the rate of reaction is relatively fast compared to oxidation by, for example, dissolved ozone. Although concentrations of H₂O₂ are low in troposphere, the high solubility (Henry's Law constant = 1x10⁵ M atm⁻¹) of H₂O₂ leads to enhanced concentrations in the aqueous aerosol phase. This enhancement drives rates higher relative to other species less prone to dissolution. In addition, peroxides can form from organic reactions within the aerosol or droplet, independent of the gas phase peroxide concentration. As stated above, the peroxide oxidation rates of S(IV) are relatively independent of pH, over the normal range of typically acidic particulates or droplets. The mechanism for this oxidation processes proceeds as follows, assuming S(IV) has previously been solvated into the aerosol phase^{12,14}:



Similar mechanisms to those above are applicable to organic hydro-peroxides, although these reactions are of limited importance due to low concentrations of organic hydro-peroxides in "typical" tropospheric aerosols or droplets. H₂O₂, being ubiquitous to both remote and polluted regions, is therefore considered the most important oxidant of

aqueous phase S(IV), and indeed is considered the dominant oxidation pathway of SO₂ in general¹².

The reaction presented in this chapter detail the most important reactions involving the species monitored during the MAX-DOAS field study, presented in Chapter 7. This includes NO₂, HCHO, SO₂, and indirectly, aerosols via the derivation of vertical profiles of aerosol extinction coefficients. It should be noted that the discussion was largely limited to tropospheric reactions outside of the marine environment. In those environments, halogen chemistries play a much larger role, whereas in the atmospheres examined in this research, halogens are of minor importance. While important on a global scale, these reactions are not germane to this research.

CHAPTER 3: STRUCTURE AND PHYSICS OF THE ATMOSPHERE

3.1 Introduction to Atmospheric Structure and Physics

Interpretation of MAX-DOAS data, or measured scattered solar radiation in general, requires knowledge of the structure and physics of the atmosphere, in particular those aspects that control the scattering and absorption of photons. The complex relationship between absorption signatures measured by a ground-based observer and the true atmospheric state can only be determined through accurate radiative transfer calculations. Presented here are the important physics and phenomena that control the structure of the atmosphere and the propagation of photons in the atmosphere.

3.2 Delineation of Atmospheric Regions

In the study of atmospheric sciences, it is commonplace to separate the atmosphere into distinct domains or layers. The primary factor in the delineation of the atmosphere is the vertical profile of temperature. Unlike pressure, which decreases exponentially with altitude (see Figure 3.1) due to the action of gravity on the atmosphere, the vertical distribution of temperature has a complex structure determined by external sources and sinks of heat energy. Atmospheric temperature and pressure profiles, taken from the U.S. Standard Atmosphere, 1976, are shown in Figure 3.1¹⁷. Here, the delineation of the atmosphere into distinct layers is presented, following Jacob, 1999¹². Examination of the enthalpy, H of an air mass:

$$H = E + PV \quad 3.1$$

where P is pressure, V is volume, and E is the internal energy of the air mass and the change in enthalpy:

$$dH = dE + d(PV) = dW + dQ + d(PV). \quad 3.2$$

where dW represents the work performed on the system, equivalent to $-PdV$, and dQ represents heat added to the system. Expansion of $d(PV)$ to PdV and VdP gives:

$$dH = dQ + VdP. \quad 3.3$$

If this air mass is to be subjected to a thermodynamic cycle of: A. an adiabatic rise from altitude z to altitude $z + dz$ followed by, B. an isothermal compression from $z + dz$ to z , and finally C. an isobaric heating at altitude z , the air mass is returned to its original thermodynamic state. The change in enthalpy for the individual cycles A, B, and C can be expressed as:

$$dH_A = VdP, \quad dH_B = 0, \quad \text{and} \quad dH_C = dQ = -mC_p dT. \quad 3.4$$

Under the assumption of no net thermodynamic change, the process can be summarized as:

$$dH_A + dH_B + dH_C = 0. \quad 3.5$$

Substituting VdP for dH_A and $mC_p dT$ for dH_C , where m is the mass of the air parcel and C_p the specific heat of air, we obtain:

$$VdP = mC_p dT. \quad 3.6$$

The quantity dP can be replaced by $-\rho_{air}g$, the density of the air mass $-\rho_{air}$ multiplied by the acceleration due to gravity. The mass of air parcel, m , can be replaced by the quantity $-\rho_{air}V$. Doing so yields the equation for the adiabatic lapse rate¹²:

$$\Gamma = \frac{g}{C_p} = 9.8 \text{ K km}^{-1}. \quad 3.7$$

If this adiabatic lapse rate was maintained in the real atmosphere, a state of equilibrium would exist, giving a temperature profile that decreases from the surface by the lapse rate. We know, however, that in the real atmosphere heat exchanges do occur, thus the familiar atmospheric structure (Figure 3.1) is obtained¹².

Variations in heating force the stratification of the atmosphere into five distinct layers. The troposphere extends from the surface of the Earth to approximately 10 to 15 km altitude. Within the troposphere, temperature typically decreases with altitude. Vertical mixing, driven by solar heating of air masses and the surface of the Earth, occurs rapidly within the troposphere. Between the troposphere and the stratosphere is a transition region, referred to as the tropopause, where the temperature gradient is relatively small. From the tropopause to approximate 45 to 55 km is the stratosphere. The stratosphere contains the protective ozone layer, which shields the surface of the Earth from harmful shortwave radiation. Exothermic photolysis of ozone releases heat, thus the temperature within the stratosphere increases with altitude. The temperature inversion within the stratosphere inhibits vertical mixing both within the stratosphere itself and between the troposphere and stratosphere. Distinct chemistries within the troposphere and stratosphere are largely a result of the limited interchange between the two layers. Above the stratosphere are the mesosphere, from 50 to 80 km altitude, the thermosphere, and lastly the exosphere, where gas molecules are capable of escaping the gravitational force of the Earth. These three layers are referred to collectively as the

upper atmosphere, and are beyond the scope of this research, which focuses primarily on the troposphere.

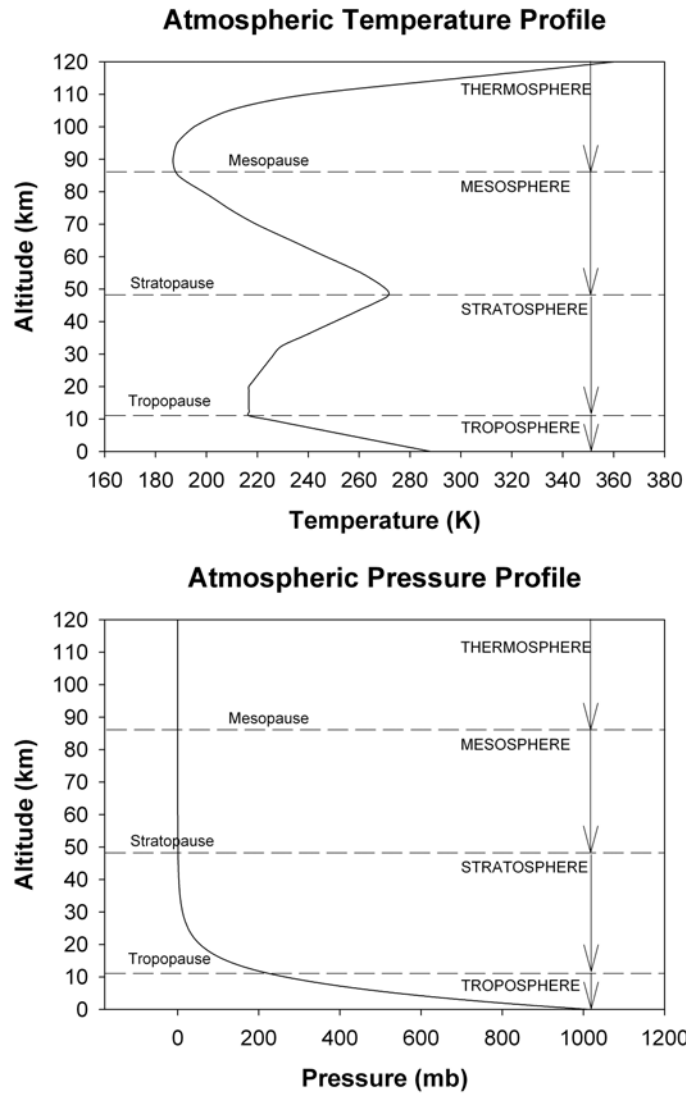


Figure 3.1: Vertical profiles of atmospheric temperature and pressure, shown with atmospheric layers as delineated by temperature. Data from the U.S. Standard Atmosphere, 1976.

3.3 Solar Radiation and Radiative Transfer

Solar radiation is the primary driver of the stratification of the atmosphere, the general circulation of air masses, and many, if not most, atmospheric chemistries. Solar energy received at the top of the atmosphere is well approximated by a blackbody at 5770 K¹⁴. The mean total amount of light energy received per unit area, known as the solar constant, is 1368 W m⁻². The spectral distribution of this blackbody radiation is strongly attenuated by absorption due to atmospheric several main atmospheric species, primarily O₃, O₂, CO₂, and H₂O¹⁴. Absorption by these species is critical to the maintenance of life, shielding living matter from harmful ultra-violet radiation and supporting the natural greenhouse effect. In addition to the primary absorbers listed above, many atmospheric species, present at much lower concentrations, also absorb solar radiation. These minor absorbers are the primary focus of this thesis.

Propagation of solar radiation through the atmosphere, including absorption, scattering, and emission processes can be described by the well-developed science and mathematics collective known as atmospheric radiative transfer. Interpretation of remote sensing data often requires replicating the experimental conditions with mathematical models of solar radiative transfer, and this is especially true when scattered solar radiation is the primary data quantity. A brief presentation of the major mathematical principles and equations related to the propagation of solar radiation, as applied to ground-based remote sensing applications, is given here.

The complexity of radiative transfer necessitates several assumptions, most importantly that the atmosphere can be divided into horizontally homogenous vertical layers. Such an assumption is commonplace in the available discussions of radiative

transfer, and is frequently referred to as the plane-parallel approximation. This convention is maintained throughout this chapter. Secondly, it is assumed that the atmosphere is bound on two sides by optical thickness $\tau = 0$ and $\tau = \tau_d$, where τ_d is the optical thickness of the entire scattering atmosphere. Both the position of the sun in the sky relative to an observer on the ground, and the direction of propagation of solar radiation can be defined by two angles, θ , the solar zenith angle, and ϕ , the azimuth angle. Angles defining radiation propagating in the Sun to Earth direction are denoted θ_0 and ϕ_0 . This notation is further extended to the functions $\mu_0 = \cos(\theta_0)$ and $\mu = \cos(\theta)$. These functions are further expanded by assigning propagation in the Sun to Earth direction as negative (-) and in the Earth to Sun direction as positive (+). With these conventions, the radiance transmitted through the atmosphere from the Sun to the surface of the Earth can be defined as $L_\lambda(\tau_d; -\mu, \phi)$.

Using these conventions and definitions, a formal expression for atmospheric radiative transfer can be expressed, following the form of Chandrasekhar¹⁸, as:

$$\mu \frac{\partial L_\lambda(\tau; \mu, \phi)}{\partial \tau} = L_\lambda(\tau; \mu, \phi) - J_\lambda(\tau; \mu, \phi). \quad 3.8$$

In the above expression, the radiative transfer equation (RTE), function J_λ is known as the source function, and contains all equations for scattering, absorption, and emission necessary for replication the measurement conditions. $L_\lambda(\tau_d; -\mu, \phi)$ again represents the Sun to surface radiance. The formal solution to equation 3.8 is given by:

$$L_\lambda(\tau_d; -\mu, \phi) = L_\lambda(0; -\mu, \phi) \exp\left(-\frac{\tau_d}{\mu}\right) + \int_0^{\tau_d} \exp\left[-\frac{(\tau_d - \tau')}{\mu}\right] J_\lambda(\tau'; -\mu, \phi) \frac{d\tau'}{\mu} \quad 3.9$$

No formal solution to equation 3.9 exists, but various approximation methods have been applied to render the problem solvable. A full treatment of these methods are not within the scope of this thesis, but will be expanded upon in the description of the various radiative transfer models used for this research.

3.4 Mathematical Description of Atmospheric Scattering

To accurately model the propagation of radiation within the atmosphere, consideration must be given to scattering due to gas molecules and particulate matter (aerosols). From the perspective of radiative transfer modeling, a common way of mathematically expressing the nature of atmospheric scattering is the phase function, which is applicable to both Rayleigh and Mie scattering. When the scattering particle is of much smaller diameter than the wavelength of light impinging upon it, the scattering treatment is said to be in the Rayleigh regime. Defining the scattering angle Θ as the angle between the incident and scattered beam, the phase function for Rayleigh scattering can be written as¹⁵:

$$P(\Theta) = \frac{\lambda^2}{8\pi^2} \left(\frac{\pi D_p}{\lambda} \right)^6 \left| \frac{m^2 - 1}{m^2 + 2} \right|^2 (1 + \cos^2 \Theta) F_0. \quad 3.10$$

Here, D_p is the diameter of the particle, m the refractive index of the particle normalized by the refractive index of air ($1.0003 + 0i$ at 589 nm)¹⁵, and F_0 is the intensity of the incident radiation. Assuming that the term $\frac{m^2 - 1}{m^2 + 2}$ is independent on wavelength, the familiar expression for the proportionality of the irradiance of Rayleigh scattered light, $1/\lambda^4$, can be applied. From this equation, it is apparent that the intensity of scattering decreases with longer wavelengths.

A phase function for scattering by larger particles, where the size of the particle is approximately the same as the impinging wavelength, or Mie scattering, can be defined, similar to that defined for Rayleigh scattering. An elegant solution to this problem was proposed in 1941 by Henyey and Greenstein, and the approximation is known as the Henyey-Greenstein approximation or simply the HG phase function approximation. In their solution, a single parameter g , or asymmetry factor, is introduced into the phase function equation. The Mie scattering phase function under this approximation can be expressed as¹⁹:

$$P(\Theta) = \frac{1}{4\pi} \frac{1 - g^2}{[1 + g^2 - 2g \cos(\Theta)]^{3/2}}. \quad 3.11$$

The asymmetry factor is defined as the intensity weighted average of the cosine of the scattering angle, and is expressed as¹⁵:

$$g = \frac{1}{2} \frac{\int_0^\pi \cos(\Theta) F(\Theta) \sin(\Theta) d\Theta}{\int_0^\pi F(\Theta) \sin(\Theta) d\Theta}. \quad 3.12$$

In contrast to the symmetric Rayleigh scattering phase function, the Mie scattering phase function allows for asymmetries in the distribution of scattering angles. Thus, for $g = 1$, scattering is entirely in the forward direction, for $g = 0$, scattering is isotropic, and for $g = -1$, scattering is entirely in the backwards direction. Non-integer values within these ranges therefore describe the distribution of scattering angles about a particle.

To simplify notation, Mie scattering phase function equation can be re-expressed in terms of the cosine of the scattering angle as¹⁸:

$$P(\mu) = \frac{1}{2} \frac{1 - g^2}{[1 + g^2 - 2g\mu]^{3/2}} \quad (3.13)$$

where $\mu = \cos(\Theta)$. As the phase function is a probability density function, it is subject to the normalization condition:

$$\int_{-1}^1 P(\mu) d\mu = 1. \quad (3.14)$$

The phase function can be easily expanded by Legendre polynomials L_n using the form:

$$P(\Theta) = \sum_{n=1}^{\infty} (2n+1)g^n L_n(\mu). \quad (3.15)$$

Here, n is the order of the polynomial. In this form, the phase function can be rapidly calculated with minimal computational effort.

3.5 Absorption by Atmospheric Gases

In addition to molecular (Rayleigh) and particulate (Mie) scattering, a third process contributes to the extinction of solar radiation passing through the Earth's atmosphere, the absorption of radiation by gaseous species. If we consider an absorbing layer of thickness dz and a beam of light of intensity F , then the loss of light due to absorption can be expressed following the form of Seinfeld¹⁵, as:

$$dF = -b_a F dz. \quad (3.16)$$

Here, the absorption coefficient is b_a , in units of m^{-1} , and the entire path length including the absorbing media runs from z_1 to z_2 . The absorption coefficient b_a results from the multiplication of an individual molecule's absorption cross-section (expressed as $\text{m}^2 \text{molecule}^{-1}$) and the number density of that species in the layer, in units of molecules m^{-3} . Integration of equation 3.16 yields¹⁵:

$$F(z_2) = F(z_1) \exp(-\delta_a) \quad (3.17)$$

where δ_a is the dimensionless absorption optical thickness. If the medium is homogeneous, then equation 3.17 can be rewritten as¹⁵:

$$F(z_2) = F(z_1) \exp(-b_a(z_2 - z_1)). \quad (3.18)$$

In this form, the extinction of light due to atmospheric absorption is known as the Beer-Lambert Law of Extinction. Overall absorbance within the layer can be expressed by¹⁵:

$$a = \frac{F(z_1) - F(z_2)}{F(z_1)}. \quad (3.19)$$

The description of atmospheric absorption presented here through the Beer-Lambert Law is expanded in Chapter 5 of this thesis, in a form more practical to the application of differential optical absorption spectroscopy principles.

3.6 Radiative Transfer Modeling

Interpretation of MAX-DOAS data often requires radiative transfer modeling to simulate the radiative transfer condition at the time of measurement. For this research, two distinct radiative transfer models, MCARaTS, the Monte Carlo Atmospheric Radiative Transfer Simulator²⁰ developed at the Japan Agency for Marine-Earth Science and Technology, and SCIATRAN, developed at the University of Bremen²¹⁻²³ were implemented. In this research, the MCARaTS model was used in situations requiring radiative transfer calculations in the presence of horizontal inhomogeneities in the atmosphere, such as an isolated plume, and SCIATRAN was used for all calculations in which the atmosphere could be treated as horizontally homogeneous.

3.6a MCARaTS

The radiative transfer model MCARaTS is a forward propagating Monte Carlo algorithm capable of radiative transfer calculations of both incoming and outgoing solar radiation. MCARaTS v. 0.10 was implemented in this research to simulate the radiative transfer in a horizontally inhomogeneous atmosphere, such as the power plant plume examined here. The physical dimensions of the modeling domain are specified in a three-dimensional Cartesian grid, within which the user can specify the location of the observing instrument and the location of any horizontal in-homogeneities of atmospheric gases, aerosols, as well as pressure and temperature. Instrumental characteristics, such as observation angle, and the solar geometries are also simulated within the model.

The fundamental equations of the MCARaTS model are detailed here, following the form and description of Iwabuchi, 2006²⁰. As a first step, the simulated photons are initialized across the model domain. In the case of solar radiation, photons are distributed uniformly at the top of the atmosphere. Radiative power of each photon in the simulation is given as:

$$E = \frac{\int \int F_{SRC}(x, y) dx dy}{N_{TOT}} . \quad (3.20)$$

Here, N_{TOT} is the number of simulated photons and F_{SRC} is the source irradiance. Collision points (scattering and absorption) are determined from a uniform random number between 0 and 1. At each collision of order n , a weight is applied to each photon based on the average single scattering albedo at the collision point, single scattering being the ratio of the scattering coefficient within a layer to the extinction coefficient of that layer. The ray tracing of any photon is continued or terminated randomly based on a

random number Russian roulette method. If the tracing is continued, the type of scattering or collision event is determined randomly based on the distribution of scattering coefficients. If the event was a scattering event, the scattering angle is determined from the phase function distribution, as described in Section 3.4. The process repeats for each photon until termination criteria are achieved. The advantage of Monte Carlo radiative transfer is that an analytical solution to the radiative transfer equation is unnecessary and the method closely simulates the physical processes of radiation propagation in the atmosphere. At the expense of simplicity is the need to simulate large numbers of photons (1×10^6 or greater) to achieve reasonable accuracy. This translates into often lengthy simulation times, and is exacerbated by the need to simulate the narrow field of view of most MAX-DOAS instruments.

3.6b SCIATRAN

The radiative transfer model SCIATRAN is a successor version of the well known GOMETRAN model²³. SCIATRAN solves numerically the radiative transfer equation (equation 3.9) using several approximation methods, including the Combined Differential Integral technique in a fully spherical atmosphere, including the effects of atmospheric refraction²⁴. Within SCIATRAN, the geographic coordinates of the observer define the modeling domain. The distribution of all gases, aerosols, and atmospheric parameters are treated as horizontally homogeneous profiles specified by external data files. The primary advantages of the SCIATRAN model is the ability to calculate radiative transfer quantities across multiple wavelengths, relatively short solution times, and the ability to calculate quasi-analytically, rather than by numerical perturbation, the Jacobian matrices necessary for inversion of atmospheric profiles from scattered light observations.

Application of SCIATRAN v. 2.2.2 in this research is limited to those species that are to be distributed homogeneously in the horizontal direction, and is thus unsuitable to species considered to be part of a distinct plume in the atmosphere.

CHAPTER 4: INSTRUMENTATION

4.1 Introduction

The MAX-DOAS spectrometer used in this research was designed around emerging miniature UV-visible spectrometer technology. This allows the instrument to be light-weight and portable, and accurate in angular control and spectral quality. High-quality data and analyses are ensured by careful characterization of the resolution and noise characteristics of the spectrometer. These instrumental characteristics are important to the spectral analysis procedures described in Chapter 5. In this chapter, details on both the design and characterization of the instrument used in this research are presented.

4.2 Instrument Components

The differential absorption spectrometer used in this work consists of three basic components. These are the spectrometer, light collection hardware, and the instrument mount. Aside from the instrument mounting/support hardware, all components are enclosed within a Pelican model 1500 air-tight case, which has been modified to accept computer and power cables. The case itself is packed with silica-gel desiccant to prevent condensation on sensitive spectrometer components due to the thermoelectric cooling of the CCD (Charge Coupled Device) detector. The air-tight case is necessary to isolate the spectrometer as much as possible from ambient conditions. The spectrometer used in this

study is a B&W-TEK miniature UV-visible CCD spectrometer, model BTU142E. The 2048 element CCD array is thermo-electrically cooled to a temperature of 15° Celsius. The spectrometer optics are optimized for low stray-light below 350 nm. This optimization is necessary as light in the ultra-violet region is more easily scattered by imperfections in the optical system, which can lead to erroneous signals recorded by the detector and the loss of intensity due to scattering. Measured spectral resolution, as determined by the full-width at half-maximum of the emission lines of a mercury vapor pen lamp, is 0.282 ± 0.005 nm. Light collection optics in the DOAS spectrometer used in this study are quite simple, consisting of a 25.4 mm planar-convex lens, with a focal length of 100 mm, mounted inside of optically black tubing. The lens itself is protected from dust and moisture by a 25.4 mm fused silica window mounted in the front of the optical tubing approximately 3 cm away from the focusing lens. A Teflon o-ring clamped to both sides of the window further isolate the focusing optic from the surrounding atmosphere. Incoming scattered solar radiation is focused onto a solarization-resistant Ocean Optics 600 μ m quartz fiber multi-mode optic cable mounted on an adjustable X-Y-Z mount, which enables fine-tuning of the alignment to the focal point of the lens. The fiber optic couples directly to the USB spectrometer. The case housing the spectrometer and optical collection hardware is mounted inside of a cast aluminum frame, which allows for the adjustment of the elevation angle by moving the entire case assembly. Control of the elevation angle is manual, and is done by moving the assembly to one of fourteen machined preset positions, including the zenith. The aluminum frame is itself mounted to a cast aluminum tripod with height-adjustable legs.

Azimuthal (typically measured from North) angle can be adjusted with a thumbscrew on the neck of the tripod.

This setup, although requiring manual adjustment of the elevation angle and particular attention and effort in ensuring that the instrument and mount are level, allows for very stable angle control, yet is relatively lightweight and portable. Figure 4.1 shows a picture of the MAX-DOAS instrument used in this research.



Figure 4.1: Multi-Axis Differential Optical Absorption Spectrometer used in this research.

In addition to the portability and ease of operation by a single operator, the use of manual angular control as opposed to electronic angular control enables the instrument to be powered by a 12-volt battery for several hours.

4.3 Instrument Function

The slit, resolution, or instrument function, of a spectrophotometer describes the attenuation of light by diffraction and optical elements that occurs during the collection

and dispersion of electromagnetic radiation. These phenomena affect the resolution of the instrument, that is, the smallest separation between spectral peaks, which can be distinguished. Accurate knowledge of the spectrometers instrument function is crucial when reference absorption cross-sections from outside sources are used in the DOAS analysis procedure, as these spectra must be conditioned with the instrument function of the DOAS spectrometer, as described in Chapter 5. To determine the instrument function of the DOAS spectrometer, a 25 mm Oriel mercury vapor pen-lamp was mounted to an optical post secured to a breadboard. The front of the DOAS telescope was positioned 150 mm from the pen-lamp. Seven individual spectra were collected, each the result of a 400 ms integration time collection, averaging 150 spectra. The emission line at ~ 334 nm was then fitted by linear regression by a Lorentzian function of the form:

$$f(x; x_0, \gamma, I) = I \left[\frac{\gamma^2}{(x - x_0)^2 + \gamma^2} \right] \quad (4.1)$$

where x_0 is the center position of the peak, I the peak height, and γ the half-width at half-maximum. Twice fit parameter γ (2γ) is the full-width at half-maximum for the peak in question. An example of this regression using a Lorentzian function is shown in Figure 4.2.

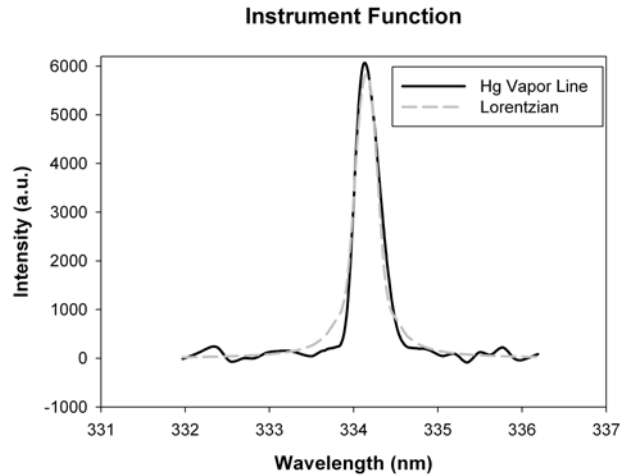


Figure 4.2: Emission line of a mercury vapor penlamp at 334 nm, measured with a differential optical absorption spectrometer, shown with a Lorentzian lineshape. FWHM is 0.282 nm.

4.4 Electronic Offset

To avoid complications in the analog to digital conversion of recorded spectra, a typical CCD detector will add an amount of signal to each pixel electronically. This is known as electronic offset. The implication of electronic offset is that even when no light strikes a pixel, a non-zero value is recorded during sampling. Electronic offset is added to each scan during the collection period, and is therefore proportional to the number of scans averaged during a collection period. Note that electronic offset is independent of integration time. Under normal laboratory conditions, when the same number of scans is used for both the reference and sample intensities in an absorption experiment, electronic offset is effectively cancelled out. However, in DOAS applications, in particular those using a single reference intensity for an entire measurement period with varying numbers of scans, the effects of electronic offset must be accounted for. This situation would arise, for example, when a zenith sky reference, collected at solar noon when the

pathlength, and thus absorptions, are at a minimum, is used as the reference intensity for all other spectra collected during a full day of measurements. A correction for electronic offset can be measured by collecting a large number of spectra using a short integration (exposure) time. For the spectrometer used in this research, an offset correction spectrum was generated by blocking all light sources from reaching the detector optics, and collecting 10,000 scans at 6 ms integration time, the minimum achievable integration time of the spectrometer. The electronic offset of the B&W-TEK spectrometer used for this research is shown in Figure 4.3. Average electronic offset for 10,000 scans at each pixel is 1039 ± 0.7 counts.

Electronic Offset

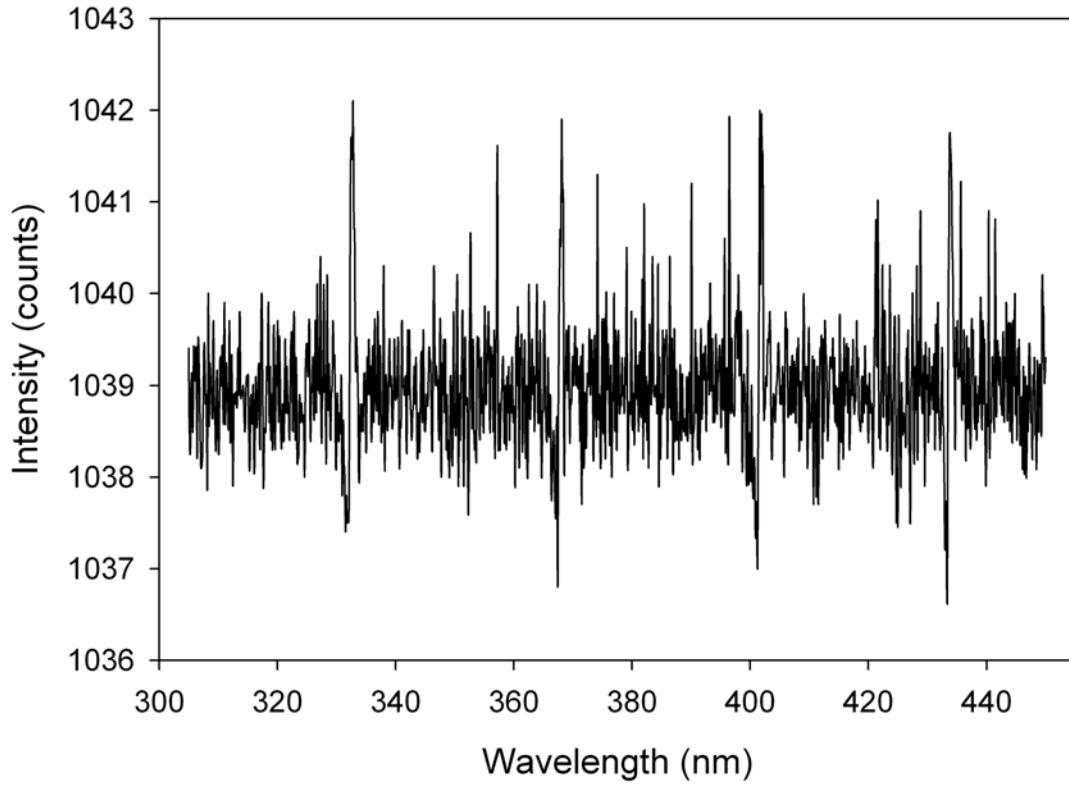


Figure 4.3: Electronic offset for the BWTEK spectrometer used in this research. Offset was recorded from 10,000 spectra using a 6 ms integration time, with no light reaching the detector.

As the electronic offset is dependent on the number of acquired scans comprising a spectrum, the offset must be scaled prior to removal. A spectrum can be corrected for offset by the following equation:

$$I_{OffsetCorrected}(\lambda) = I(\lambda) - \frac{MS}{OS} Offset(\lambda). \quad (4.2)$$

Here, MS is the number of scans in the measured spectrum, OS the number of scans in the *Offset* spectrum, and $I(\lambda)$ the original measured spectra.

4.5 Dark Current

Dark current is a noise component of spectra collected with a CCD detector which arises from thermally excited electrons which reach the conduction band of the CCD, and are thus recorded as signal. Cooling of the CCD chip reduces the magnitude of the dark current by impeding thermal excitation, although some dark current is invariably present in all measurements. At a constant temperature, the magnitude of the dark current is proportional to the integration time. For longer integration times, more thermally excited electrons reach the conduction band of the CCD chip and recorded as part of the signal. As with electronic offset, a dark current correction can be recorded, although most modern spectrometer control packages, such as the one used in this research, dark current is automatically compensated for. To record a dark current correction spectrum, long integration times are used, collecting a single scan only. Here, an integration time of 60 seconds was used to collect the dark current spectrum, with no light reaching the detector. The dark current correction for the B&W-TEK spectrometer is shown in Figure 4.4.

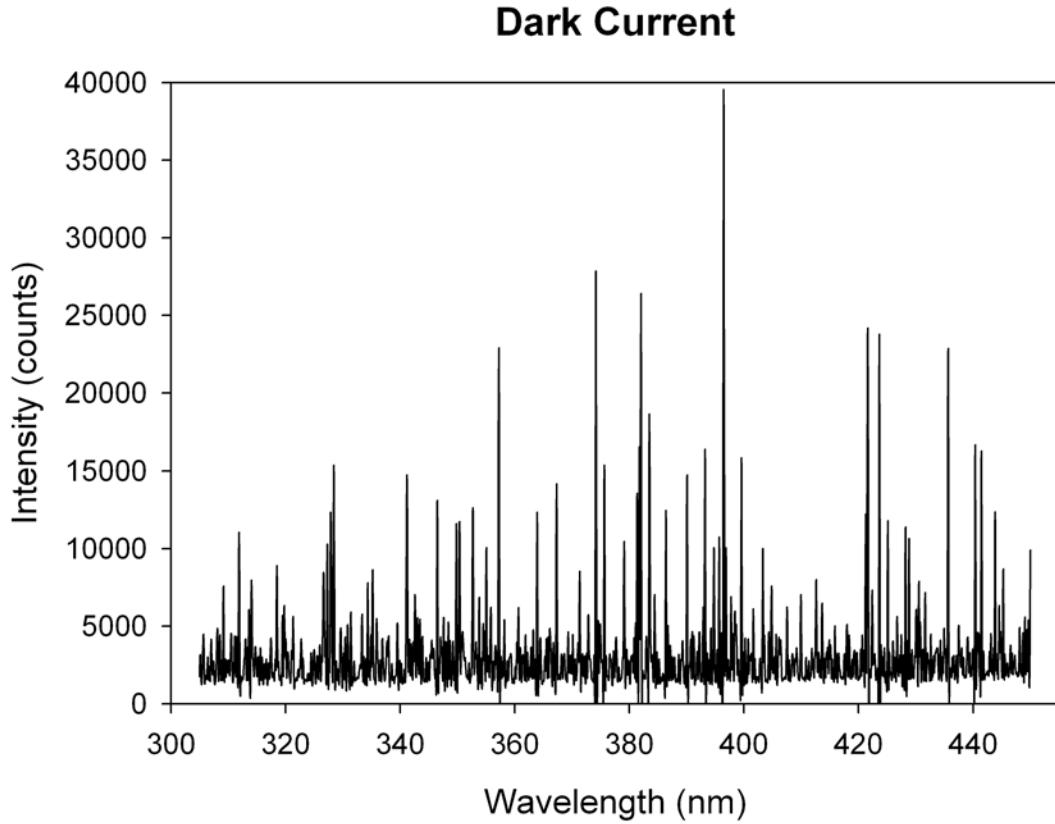


Figure 4.4: Dark current correction for the BWTEK spectrometer recorded with no light reaching the detector, using a 60 second integration time.

Due to the dependency of the magnitude of the dark current signal with integration time, the dark current must be scaled prior to subtraction when correcting collected spectra.

This is done by the following equation:

$$I_{\text{DarkCurrentCorrected}}(\lambda) = I(\lambda) - \frac{tM}{tDC} \text{DarkCurrent}(\lambda). \quad (4.3)$$

Here, tM is the integration time of the measured spectrum to be corrected and tDC is the integration time of the dark current spectrum.

4.6 Noise Considerations

All spectrophotometric measurements are subjected to varying degrees of noise, which arise from both the instrument itself and the statistics of photon collection. A series of spectra collected in rapid succession under the same conditions will demonstrate noise, which fluctuates about a mean value. Treating this as a normally distributed function, the total noise in a measurement can be defined as:

$$s_{Total} = \sqrt{s_{Ins}^2 + s_{Phot}^2} \quad (4.4)$$

where s_{Ins} is the noise associated with the instrument itself and s_{Phot} the noise associated with the detection of photons. The fluctuation in recorded photons is described by Poisson statistics, and spectrometers are designed so that, under adequate signal intensity, photon noise is dominant. Both forms of noise can be estimated from measured spectral data using replicate measurements of both offset, as described in Section 4.4, and that of a light source.

Instrument noise, s_{Ins} , can be estimated from replicate offset spectra. In this case, the standard deviation of the difference between two offset spectra yields an estimate of the noise due to the instrument itself. Total noise can be estimated from replicate measurements of a stable light source, using equation 4.5, below²⁵.

$$s_{Total} = rms \ noise = \sqrt{\frac{\sum (s_{avg} - s_i)^2}{n}} \quad (4.5)$$

Here, s_{Total} is defined as the root mean squared error, determined from thirty replicate measurements of the spectrum of a deuterium-tungsten UV-visible light source, Ocean Optics Mini-D2T, collected within a short time period of one another. s_{avg} is the average of the thirty spectra, s_i are the individual spectra, and n is the number of spectra averaged.

All spectra have been corrected for dark current, and were collected at 100 ms integration time. From these measurements and equation 4.5, the total noise was determined to be 178 counts at 75% saturation. Figure 4.5 shows the root mean square error spectra of the B&W-TEK spectrometer used in this research.

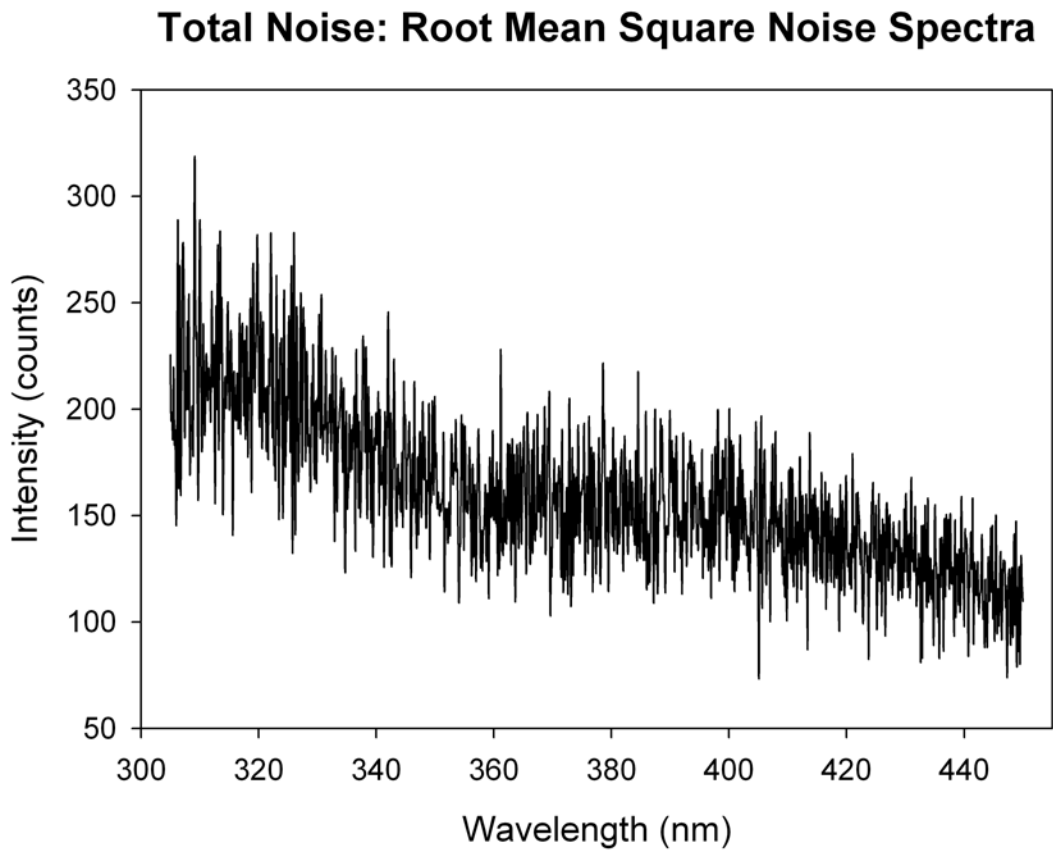


Figure 4.5: Root mean squared error of the B&W-TEK spectrometer used in this research. The total noise was calculated as the root mean squared error of thirty spectra of an Ocean Optics deuterium-tungsten light source, Mini-D2T.

For the B&W-TEK spectrometer used in this research, s_{Total} was calculated as 178 counts. The total noise value calculated here is only valid if sufficient photons are collected, thus ensuring that photon noise is the dominant source of noise. To ensure this criterion is met, recorded intensities are typically maintained at ~75% of the saturation value of the pixels (~65,000 counts for B&W-TEK BTU142), although this cannot always be achieved across the entire wavelength region of a spectrometer.

CHAPTER 5: SPECTRAL ANALYSIS

5.1 Introduction: Principles of Differential Optical Absorption Spectroscopy

Differential Optical Absorption Spectroscopy, or DOAS, is a spectroscopic technique used to determine the concentration of atmospheric constituents by application of the Beer-Lambert Law:

$$I(\lambda) = I_0(\lambda)e^{-\sigma(\lambda)cl} \quad (5.1)$$

where $I(\lambda)$ is the transmitted intensity of light at wavelength λ with initial intensity $I_0(\lambda)$, after transmission along pathlength l in centimeters, containing concentration c in units of molecules per cm^3 of a constituent with absorption cross-section σ with units cm^2 per molecule²⁶. From equation 5.1, the optical density, $OD(\lambda)$, can be defined as:

$$OD(\lambda) = \ln(I_0(\lambda)/I(\lambda)) = -\sigma(\lambda)cl \quad (5.2)$$

and the concentration of the constituent can be determined using the relationship:

$$c = OD(\lambda)/(-\sigma(\lambda)l). \quad (5.3)$$

equations 5.1-5.3 are applicable in most laboratory settings, but in the open atmosphere using light path-lengths of several kilometers, the Beer-Lambert Law must be modified to include extinction from elastic Rayleigh and Mie scattering processes²⁷. Here, extinction refers to the loss of light from a direct beam, and can be thought of as both scattering and absorption. Rayleigh scattering, the elastic scattering of light by air molecules, is treated as an additional extinction process with extinction cross-section $\sigma_R(\lambda)$.

The overall extinction due to Rayleigh scattering, $\varepsilon_R(\lambda)$, can be defined as a function of wavelength and the concentration of scattering species $c_{scatter}$ using the expression^{28,29}:

$$\varepsilon_R(\lambda) = \sigma_R(\lambda)c_{scatter}. \quad (5.4)$$

In like manner, elastic scattering by aerosols (Mie) is also treated as an extinction process with wavelength dependent extinction cross-section $\sigma_M(\lambda)$, and overall extinction²⁷:

$$\varepsilon_M(\lambda) = \sigma_M \lambda^{-n} \quad (5.5)$$

where n is an integer between 1 and 4²⁶. Thus, equation 5.1 can be re-written to include the extinction due to Rayleigh and Mie scattering. Additional absorbing species are also included by summing over all species j :

$$I(\lambda) = I_0(\lambda)e \left[-l \sum_j \sigma_j(\lambda)c_j + \varepsilon_R(\lambda) + \varepsilon_M(\lambda) \right]. \quad (5.6)$$

The processes outlined above describe absolute extinction using the Beer-Lambert Law, in which the features of a spectrum are described as the attenuation of source intensity I_0 . Spectroscopic analysis in the atmosphere, however, often requires the use of differential as opposed to absolute extinction. As most atmospheric absorbers and scatterers are present or assumed to be present in the air mass probed, it is difficult to obtain reference intensity $I_0(\lambda)$ containing no spectral signature of the j^{th} absorbing species or extinction due to Rayleigh and Mie scattering. Differential optical absorption spectroscopy overcomes this limitation by modification of the reference intensity, and isolating those spectral features which differ from that estimation. To illustrate this, consider the spectrum of Figure 5.1.

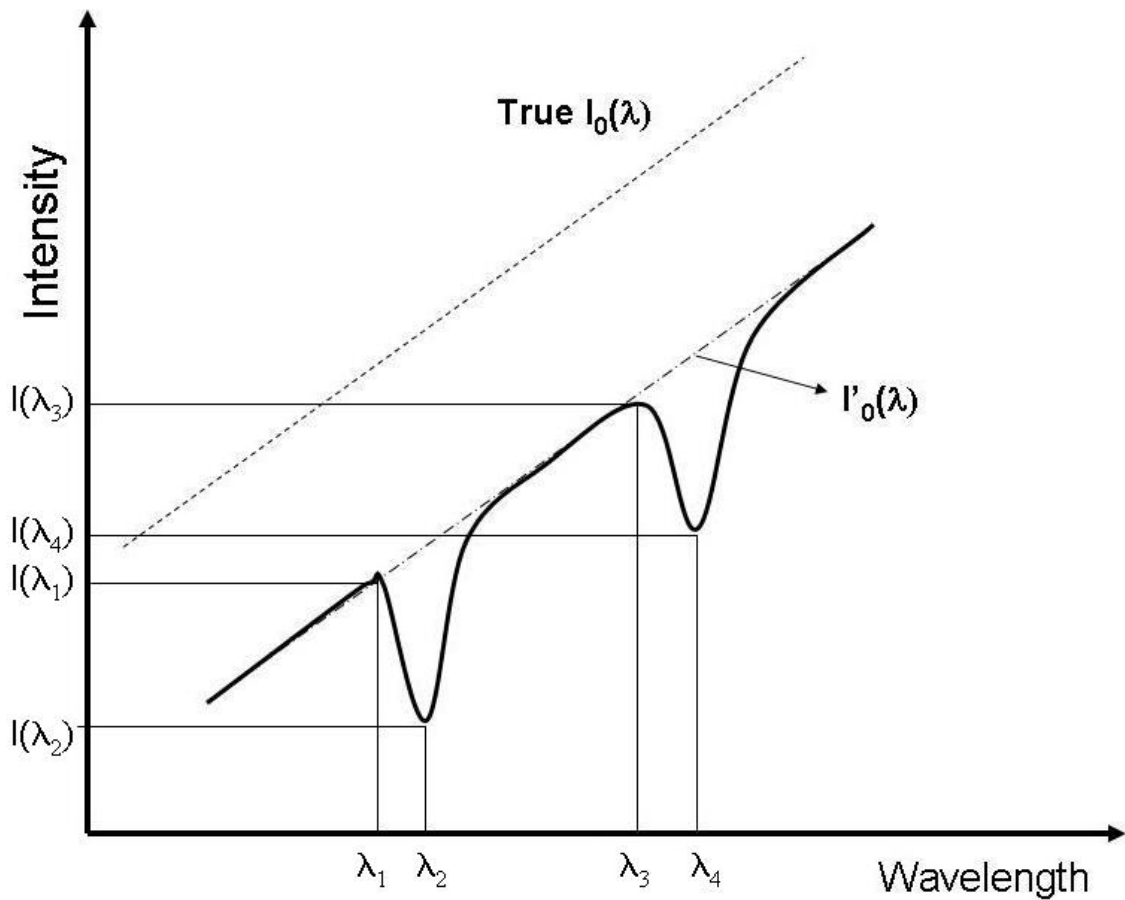


Figure 5.1: An absorption band shown as a departure from the true $I_0(\lambda)$ as in laboratory spectroscopy and as a departure from $I'_0(\lambda)$, as in differential spectroscopy.

Here, two absorption bands are defined as the difference in intensity between points where the spectrum is relatively smooth (λ_1 and λ_3), and points where the spectrum has changed rapidly in intensity (λ_2 and λ_4), as opposed to departures from true intensity I_0 , as is the case for laboratory extinction measurements. If those points on the smooth

function absent of narrow-band features, given in Figure 5.1 as $I'_0(\lambda)$. This implies that a separation is possible, isolating the broad-band, smooth features of the spectrum from narrow-band features. If the extrapolated smooth portion is subtracted from the overall spectrum, the narrow-band, or differential features can be isolated. As the extinctions due to Rayleigh and Mie scattering, given by equations 5.4 and 5.5, are broad-band features with respect to wavelength, the differential, narrow-band structure of the measured spectrum is considered to represent only absorption features. However, such a separation also removes those absorptions or broad-bandwidth absorption features. If the DOAS technique is to be quantitative, a means of isolating the narrow-band, differential features from the absorption cross-sections σ of those species present at the time of collection must also be used^{26,27,30-33}.

By analogy to the extrapolation and removal of the broad-band component of a measured spectrum shown in Figure 5.1, the absorption cross-section of the j^{th} species can also be separated into narrow-band and broad-band components. Thus, each cross-section is expressed as the sum:

$$\sigma_j(\lambda) = \sigma_j(\lambda)_{broad\ band} + \sigma_j(\lambda)_{narrow\ band} \quad (5.7)$$

Using the broad-band component of equation 5.7, the reference intensity $I'_0(\lambda)$, in the absence of differential absorption, previously defined as the extrapolation of the smooth points of the measured intensity spectrum, can be mathematically defined as:

$$I'(\lambda)_0 = I_0(\lambda) \exp \left[-l \sum_j \sigma_j(\lambda)_{narrow\ band} c_j \right] + \varepsilon_R(\lambda) + \varepsilon_M(\lambda) \quad (5.8)$$

Accordingly, the intensity $I(\lambda)$ can be described using the narrow-band component of the absorption cross-section of the j^{th} species. Lastly, following the Beer-Lambert Law, the differential optical depth, $DOD(\lambda)$, can be defined as:

$$DOD(\lambda) = \ln(I'_0(\lambda)/I(\lambda)) = -l \sum_j \sigma_j(\lambda)_{\text{narrowband}} c_j \quad (5.9)$$

In practice, the extrapolation of the broad-band components, and separation of the narrow-band components of both atmospheric intensity and absorption cross-section spectra is accomplished by robust mathematical techniques, the details of which are given in sections 5.6 and 5.7 of this chapter.

To determine the concentration of the j^{th} species, the differential absorption cross-section $\sigma_i(\lambda)_{\text{rapid}}$ is fitted by least squares regression to the measured differential optical depth, as described in section 5.8 of this chapter. The resultant fit coefficient is the concentration of the j^{th} species, or in the case of an unknown pathlength, the differential slant column density of the j^{th} species^{1,27}. The least squares fitting procedure often includes a correction for wavelength calibration differences between the measured differential optical depth spectrum and the reference differential absorption cross-sections, as well as corrections for stray light in the measurement spectrometer. Additional corrections for instrumental spectral broadening and noise are also made prior to the least squares fit. Each step of the differential spectral analysis presented above and the fundamental scientific basis for each process is detailed in this chapter. The rudimentary steps of this analysis, and the relevant sections of this chapter in which each processes is described, are shown in Figure 5.2.

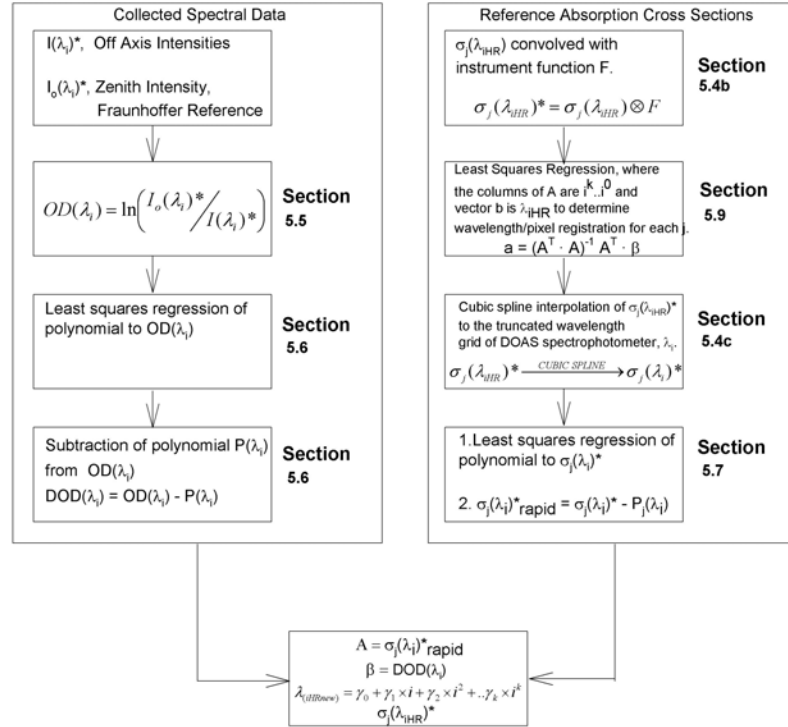


Figure 5.2: Pre-processing of both collected atmospheric intensities (left) and reference absorption cross-sections (right), shown with references to relevant sections of this document. The necessary output for subsequent analysis procedures are the design matrix A , data matrix B , the wavelength pixel mapping function for the j species to be analyzed, as well as the convolved reference absorption cross-sections with their original wavelength grids.

Note that no distinction has been made at this point between continuous and measured, discrete spectra. The concept of discrete spectra is introduced later, and was purposely omitted from the above description of differential absorption, which is a description of the physical nature of light absorption. In points of discussion where this distinction is made, discrete data points will be indicated by the subscript i and the subscript iHR , indicating the wavelength grid of the DOAS spectrophotometer and the higher resolution wavelength grids of reference absorption cross-sections, respectively.

5.2 Species Measurable by Differential Techniques

DOAS techniques for the UV-visible region are concerned with molecules that absorb light in the 310 to 770 nm wavelength region. Electromagnetic radiation below 310 nm is strongly attenuated by the Hartley band of ozone, and wavelengths below 180 nm are almost completely absorbed by atmospheric oxygen^{34,35}. Differential spectroscopy is also possible for longer wavelengths, but is limited by the strong absorptions of H₂O and CO₂ in the infrared. In practice, the nature of the excitation light source also limits wavelength coverage, and therefore the number of species capable of being analyzed.

The Max-Planck Institute maintains a database of atmospheric species which absorb light within the UV-visible wavelength region, and currently contains approximately 670 species³⁶. This is a significant reduction in the number of species to be considered in light of the vast number of gaseous species present in the atmosphere at any given time. Despite the large number of atmospheric species capable of absorbing UV-visible light, the majority of atmospheric species are unsuitable for differential spectroscopic applications. Even if the species is a strong absorber, or is present in high concentrations, that species cannot be detected using differential techniques if it lacks sufficient narrow-band absorption features, or structure, in its absorption cross-section spectrum, as described in section 5.1^{26,32,33}. For example, Figure 5.3 shows the absolute absorption cross-section of nitric acid. Despite a relatively large absolute absorption cross-section, nitric acid lacks the narrow, structured absorption features necessary for differential spectral analysis.

Nitric Acid: Absolute Absorption Cross Section

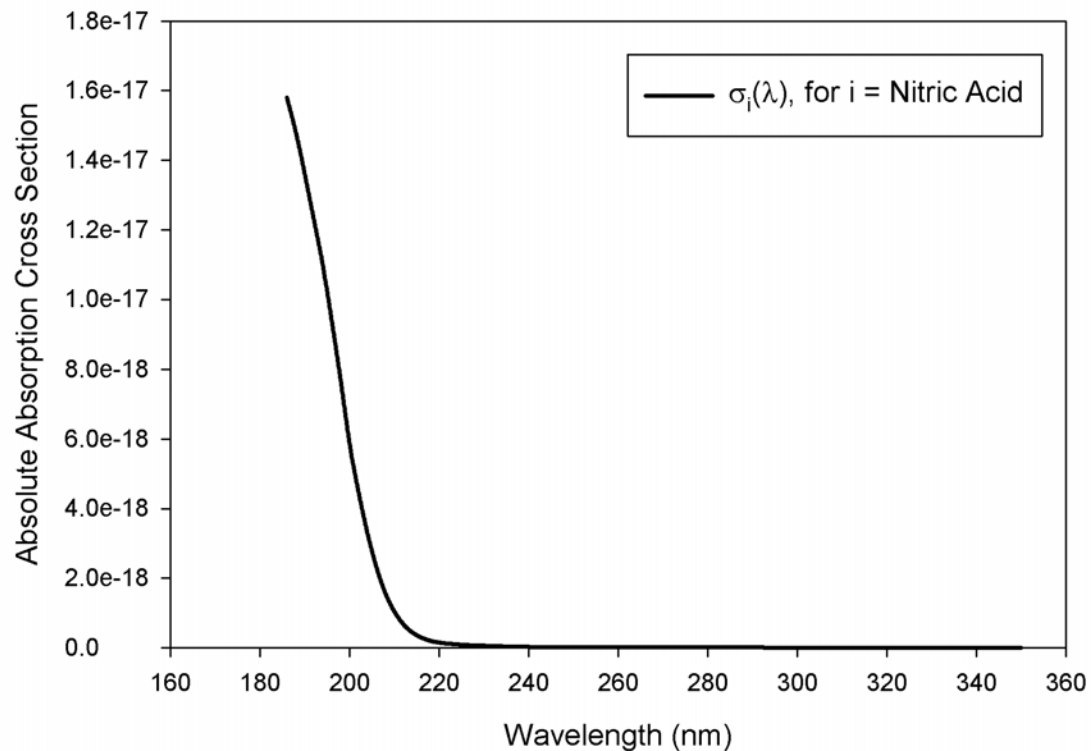


Figure 5.3: Absolute absorption cross-section of nitric acid. The lack of peaked structure necessary for differential analysis is clearly evident.

That is, if the extrapolation and differentiation of Figure 5.1 is applied to the cross-section of nitric acid, the resultant spectrum would be a monotonous function that would not impart distinct narrow-band features to an absorption spectrum. The vast majority of absorbers of ultra-violet or visible radiation present in the atmosphere demonstrate absorption spectra similar to that of nitric acid, having little or no narrow-band absorption features, which can alternatively be thought of as multiple peaks and valleys in the absorption cross-section. In contrast, Figure 5.4 shows the absolute and differential absorption cross-sections of NO_2 . Note the broad-band component of the absorption

cross-section, calculated here as a moving average smoothed version of the original spectrum.

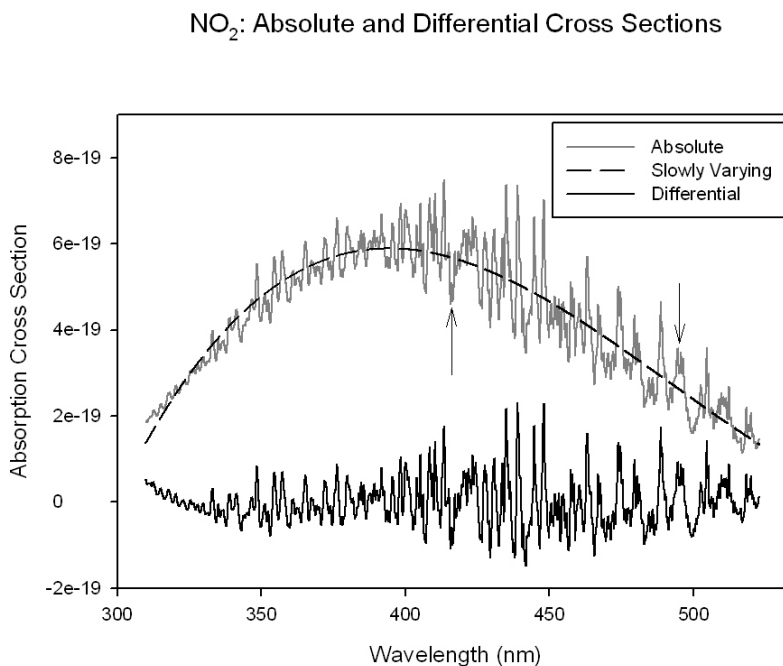


Figure 5.4: Absolute and differential absorption of NO₂. Two strong differential features are indicated by the arrows.

The broad-band component represents not only the overall trend in the absorption, but also the shape of the excitation light source and any broad-band instrument effects, for example, poor transmission of certain wavelengths in the optical components. Arrows indicate examples of the narrow-band structure necessary for differential spectral analysis.

Of the approximately 670 documented gaseous species that absorb UV-visible radiation in the atmosphere, only a small percentage of those species have absorption

spectra with the characteristic narrow-band structure necessary for differential spectral analysis. At the time of writing, approximately 20 gaseous species capable of being detected and analyzed by UV-visible differential absorption spectroscopy, using either natural or artificial light sources, have been identified²⁷. Figure 5.5 shows the absorption cross-sections of 10 atmospherically relevant species which have been detected and/or quantified using differential optical absorption spectroscopy. Note the narrow-band absorption features of each spectrum in contrast to the relatively smooth nature of nitric acid shown in Figure 5.3

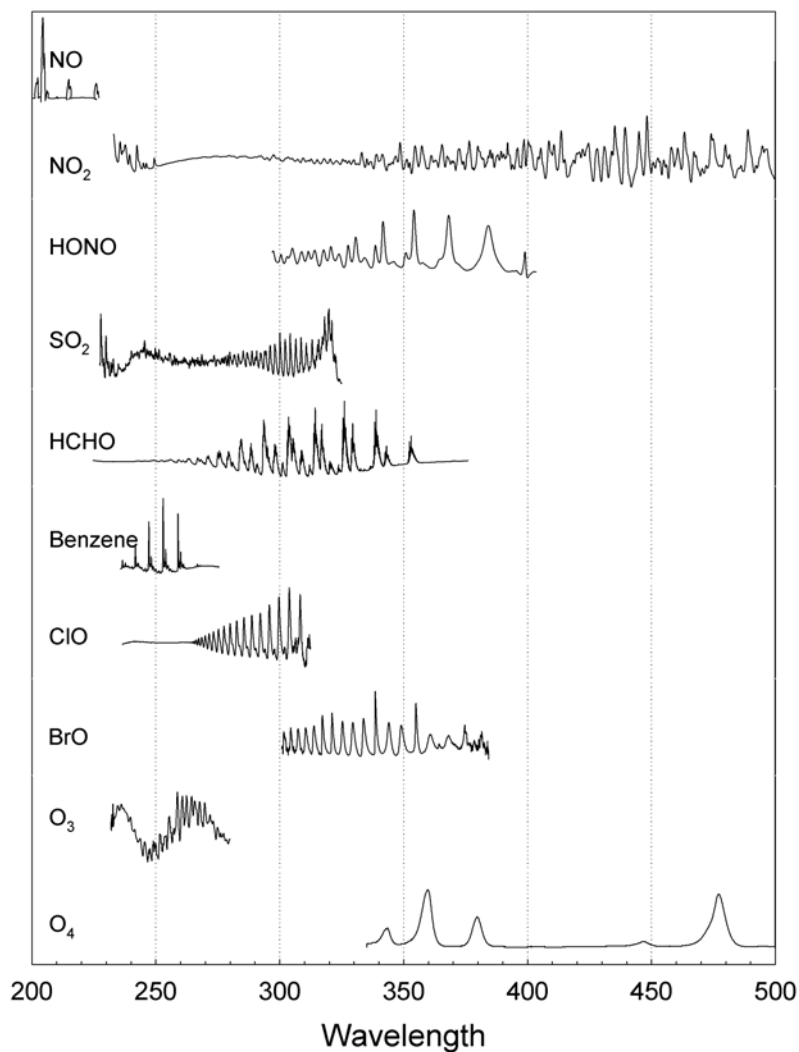


Figure 5.5: Differential absorption cross-sections of 10 species commonly found in DOAS analysis.
 The spectra were taken from: NO³⁷, NO₂³⁸, HONO³⁹, SO₂⁴⁰, HCHO⁴¹, Benzene⁴², ClO⁴³, BrO⁴⁴, O₃⁴⁵, and O₄⁴⁶

5.3 Analysis Window Selection

As important as the selection of species to be included in the differential analysis is the narrowing of available wavelengths to smaller wavelength regions, or, as commonly presented in the literature, the selection of analysis windows where species of interest absorb strongly. Equation 5.9, defining differential absorption, could

theoretically be applied across the entire UV-visible wavelength region, limited only by the spectral coverage of the DOAS instrument. In practice, however, only limited regions of the entire spectral region of the instrument are used for differential analysis^{30,31}. Although there is no single rule dictating the selection of the spectral windows for analysis, there are three important guidelines. First, the spectral window chosen must contain significant differential absorption structure of the species of interest. Illustrations such as Figure 5.5, which show the differential absorption features of a great many species detectable by differential methods, are a valuable tool in wavelength region selection. Secondly, wavelength regions should be selected where there is minimal interference from other species also demonstrating differential absorption. Ideally, a wavelength region where only the species of interest absorbs would be selected, although this situation is rarely encountered. As an example, consider the absorption of NO₂, which covers a large portion of the UV-visible wavelength region. Based on Figure 5.5, it would be prudent to analyze atmospheric spectra for NO₂ above approximately 400 nm, based on the lack of absorption structure of other species at these higher wavelengths, although consideration to the capabilities of the particular spectrometer used must be given. Above 400 nm, it is apparent that NO₂ has strong differential features, with only minor interference from the O₄ collisional complex. Although extinction due to absorption scales with both the magnitude of the absorption cross-section and concentration, analysis window selection is primarily based on the presence of absorption features. The most appropriate choice for an NO₂ fitting window would therefore be selected above 400 nm. It should also be noted that even if a species is not a target analyte but absorbs differentially in a selected wavelength interval, that species must be

included in the analysis by equation 5.9, even if that species is not anticipated to be present at concentrations above the detection limit of the instrument.

Lastly, the spectra of the excitation light source must be considered. In many cases, the emission spectrum of the light source will exhibit significant structure, which may interfere with differential analysis. If sun or moonlight is used as a source, much care must be taken to avoid regions where strong solar Fraunhofer (native emission lines in the solar spectrum) lines occur¹. Removal of these spectral features can be difficult even when a reference solar spectrum is subtracted from the measured data, due to the broadening of solar lines from molecular rotational Raman scattering, also known as the Ring effect^{47,48}.

The selection of wavelength windows for differential analysis is greatly simplified by the amount of research conducted using the differential technique over more than three decades. For the majority of species shown in Figure 5.5, as well as several others, standard wavelength windows, or intervals, for their analysis have been established in the literature, following the guidelines detailed above. Only for a newly discovered species exhibiting differential absorption features, an infrequent occurrence, would a rigorous analysis to determine the most appropriate analysis window be necessary, although some consideration to the individual instrument and atmospheric conditions during the time of collection must be given. Table 5.1 summarizes the analysis windows used for ten of the most common species quantifiable by differential optical absorption spectroscopy. From Table 5.1, it can be seen that the majority of the species shown can be quantified within several spectral windows. Note the difference in windows between techniques using artificial and solar light. These differences can be attributed to the avoidance of spectral

features associated with the Fraunhofer lines found in the solar spectrum. Note that artificial light sources are capable of projecting wavelengths of radiation which do not reach the surface of the Earth from natural sunlight.

SPECIES	LIGHT SOURCE / INTERVAL(nm)	REFERENCE
Benzene	Artificial, 250-290	49
BrO	Solar, 346-359	50
ClO	Artificial, 284-302	51
Formaldehyde (HCHO)	Artificial, 323-335 Solar, 335-357	30,52,53
HONO	Artificial, 350-375	33
NO ₂	Artificial, 323-335 Artificial, 345-380 Solar, 430-455 Artificial, 400-450 Solar, 430-441	1,30,32,54-56
NO ₃	Lunar, 656-668 Lunar, 646-682 Solar, 640-680	57-59
O ₃	Artificial, 325-350 Solar, 400-453 Solar, 315-330	31,32,60-62
O ₄	Solar, 347-388, 415-682 Solar, 335-367 Solar, 460-490	7,63,64
SO ₂	Solar, 303-313 Solar, 307-316 Solar, 316-325	5,65,66

Table 5.1: Wavelength windows of common analytes used in past differential optical absorption studies.

5.4 Processing of Absorption Cross-Section Spectra Prior to Differential Analysis

Analysis of measured differential optical absorption spectra to determine the concentration of gaseous species relies on the availability of high-quality absorption cross-section spectra ($\sigma(\lambda_{\text{IHR}})$, equation 5.1 for discrete case), which can be processed and subsequently fitted by least squares techniques to the measured optical depth spectra. To this end, absorption cross-sections can be measured in the laboratory using the DOAS instrument, a suitable light source, and a gas handling system to deliver species of interest into an optical cell³². The advantage of this method of acquiring reference absorption cross-sections is that the collected spectra will include all spectral artifacts introduced by the instrumentation, as well as a consistent wavelength calibration and resolution as collected atmospheric spectra. However, laboratory collection of high-quality absorption cross-section data requires a gas handling system, standardized trace gases, and temperature control capabilities. At the lower resolution of a typical DOAS spectrometer, these spectra will typically be of use only for that particular instrument.

As an alternative to laboratory measured trace gas absorption spectra, it is commonplace within the DOAS scientific community to use absorption spectra published from laboratories dedicated to the acquisition of temperature dependent, high-resolution gaseous absorption spectra. The earliest measurements of NO_3 and other trace species by differential methods relied on absorption cross-section data collected in such a manner, and that precedence continues in the most current DOAS literature^{58,64}. In addition to being of much higher quality than what is capable of a typical DOAS instrument (typical resolution of ~ 1 nm), such spectra are readily available and maintained in electronic databases, such as that of the Max-Planck Institute, Division of Atmospheric Chemistry.

In order to use absorption cross-sections collected from outside sources, a number of preprocessing steps are necessary²⁷. The disadvantages of using spectra from outside sources, aside from the additional mathematical processing necessary, is the need for intensive instrumental characterization to realize the effects of stray light and spectral artifacts on measured spectra versus those collected from outside sources. The mathematical techniques used in the preprocessing of absorption cross-section spectra are detailed in Sections 5.4b-5.4d of this thesis. However, it is necessary first to examine the scientific basis of these techniques, which are strongly rooted in principles of spectroscopy, optics, and digital signal processing, and are detailed in section 5.4a, below.

5.4a Recording of spectral data by spectrophotometers

Differential optical absorption spectroscopy is a spectrophotometric technique, and as such, there are several common elements to all DOAS instruments. All DOAS instruments require a suitable light source, such as the Sun, a high intensity UV-visible lamp, or UV-visible laser. Suitable optics, capable of collecting light emitted by the source and directing that light to the spectrophotometer, such as telescopes, focusing lenses, and fiber optics are also necessary. Details of the instrument used in this work are presented in Chapter 4. Once directed to the spectrophotometer, collected light is focused onto an entrance slit, then to a wavelength selection component. The wavelength selector, whether a prism, filter, or grating, separates the collected white light into its component wavelengths and disperses these wavelengths onto a detector. The detector registers the intensity of light at discrete wavelength intervals as an analog signal, which is subsequently converted to a digital signal suitable for computer storage or readout.

This process has several implications on the information content as well as appearance of the collected spectrum, and thus the mathematical treatment applied.

To illustrate the process of spectral collection and the attenuation of a given spectrum by the collection and discretization of the spectral signal, consider a spectrum of solar radiation prior to passing through the Earth's atmosphere. The sun itself is considered a spherical light source, located 1.5×10^8 kilometers from the Earth's surface, with a diameter of 1.4×10^6 kilometers. Un-attenuated by the Earth's atmosphere, the sun approximates a blackbody emitter with a temperature of approximately 5770 K, emitting a continuum of electromagnetic radiation from approximately 200 to 3000 nm¹⁴. This continuum passes through the Earth's atmosphere and, ignoring absorption processes for the purposes of demonstration, is assigned intensity $I(\lambda)$, as in Figure 5.6a, adapted from Stutz and Platt, 1996⁶⁷.

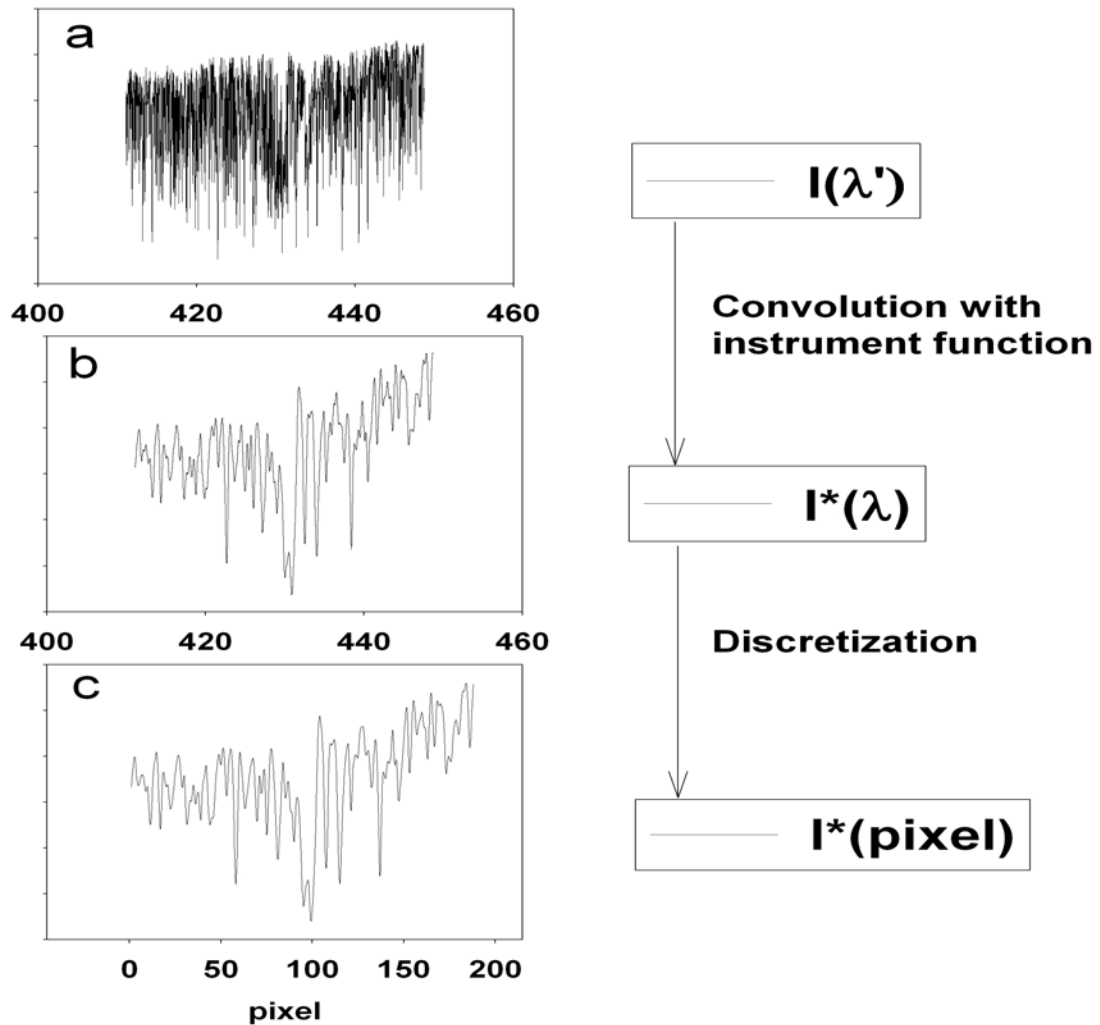


Figure 5.6: Attenuation of the solar spectrum during collection and pixelation by a spectrophotometer.

Intensity $I(\lambda)$ is gathered by the collection optics of the instrument and directed to the entrance slit of the spectrophotometer. Changes to the shape of the intensity spectrum are introduced by the collection optics and the limited resolution of the spectrometer itself, giving altered continuous intensity spectrum $I(\lambda)^*$, as in Figure 5.6b. How the instrument

alters the continuous spectrum can be described by function F , known as the response or instrument function, and intensity $I(\lambda)^*$ given by^{27,68}:

$$I(\lambda)^* = \int_{-\infty}^{+\infty} I(\lambda')F(\lambda - \lambda')d\lambda' \quad (5.10)$$

Recording of the continuous, convolved spectrum $I(\lambda)^*$ by the detector, which maps wavelength ranges to discrete pixels or bins, destroys the continuous nature of the spectrum and degrades information content, yielding intensity spectrum $I(pixel)^*$. $I(pixel)^*$ can alternatively be expressed in terms of discrete wavelengths as $I(\lambda_{(i)})^*$, if each pixel is assigned a wavelength by a calibration function, as detailed in section 5.9.

As $I(\lambda_{(i)})^*$ represents an actual intensity spectrum collected by a DOAS instrument, the model of attenuation in the atmosphere, previously defined for continuous spectra by equation 5.6 above, can be modified to better express the discrete, instrument function attenuated nature of the data as:

$$I(\lambda_i)^* = I_0(\lambda_i)^* e^{\left[-l \sum_j \sigma_j(\lambda_i)^* c_j + \varepsilon_R(\lambda_i) + \varepsilon_M(\lambda_i) \right]} \quad (5.11)$$

where $\sigma_j(\lambda_i)^*$ is the absorption cross-section of the j^{th} species, which has been subjected to instrument function convolution (*) and discretization to the wavelength grid of the DOAS spectrophotometer (λ_i). Following the differential absorption methods detailed in section 5.1, optical depth, previously defined by equation 5.2, can be expressed for the discrete, convolved case for j trace gas species as:

$$OD(\lambda_i) = \ln(I_0(\lambda_i)^*/I(\lambda_i)^*) = -l \sum_j \sigma_j(\lambda_i)^* c_j . \quad (5.12)$$

In like manner, the differential optical depth, previously defined for the continuous case by equation 5.9, can be expressed for actual data as:

$$DOD(\lambda_i) = \ln(I'_0(\lambda_i) / I(\lambda_i)) = -l \sum_j \sigma_j(\lambda_i) c_j \quad (5.13)$$

Equation 5.13 serves as the regression model for the spectral analysis employed in this research, as it deals with discrete, instrument attenuated spectra as encountered in actual analysis.

Manipulation and processing of absorption cross-section spectra attempts to replicate, as closely as possible, the attenuation of spectra as they are collected and recorded by a spectrophotometer. In a DOAS framework, the goal is to apply the above principles to absorption cross-sections collected with a spectrophotometer different than that of the DOAS instrument, so that the resultant spectra are as if they were collected with the DOAS spectrophotometer itself. The mathematical routines used to replicate the effects of the instrument function as well as discretization to the pixels of the DOAS spectrophotometer are detailed in sections 5.4b and 5.4c, respectively.

5.4b Convolution with the instrument function

The instrument function of a spectrophotometer describes the attenuation of light by diffraction and optical elements that occurs during the collection and dispersion of electromagnetic radiation. These effects can be both broad-band, introduced, for example, by poor transmission of certain wavelengths in the optical setup, or narrow-band, such as the effects introduced by diffraction, and stray light impinging on certain regions of the detector⁶⁹. As the DOAS technique is primarily concerned with narrow-band phenomena over limited wavelength ranges, broad-band instrumental effects are

largely removed as the slowly varying component of measured and reference spectra, as described in Section 5.1. However, the narrow-band effects of spectral sampling must be accounted for if using absorption cross-sections collected with spectrophotometers other than that of the DOAS instrument. Narrow-band effects can be attributed to both the diffraction efficiency of the wavelength separation device and the optical setup of the spectrometer which determines the resolution of the instrument, as well as to artifacts introduced to measured spectra, from, for example, faulty detector pixels. Spectral artifacts can be detected and removed through instrument characterization, and are not typically considered to be part of the instrument function. Henceforth, the term instrument function will refer to those processes that control the resolution of the instrument, unless explicitly stated otherwise. In general, the instrument function can be determined by measuring the spectrum of several emission lines with known line widths. For the case of the spectrophotometer used in this research, the instrument function is a Gaussian function with full width at half maximum of 0.282 nm, as described in Chapter 4. In Figure 5.6 above, the alteration of the spectrum from trace a to b shows these narrow-band effects, and can be thought of as a “smearing out” of the fine structure present in the continuum spectrum.

Equation 5.10, describing the attenuation of the continuum intensity with the instrument function F :

$$I(\lambda)^* = \int_{-\infty}^{+\infty} I(\lambda')F(\lambda - \lambda')d\lambda' \quad (5.10)$$

is not practical for DOAS applications, however, as continuum signals are not dealt with. A more practical presentation of convolution is the generalized, discrete form, which can

be applied to any two signals. In this form, the equation is referred to as the convolution sum, expressed as ⁷⁰:

$$y(i) = \sum_{j=0}^{M-1} h(j)F(i - j) \quad (5.14)$$

where h is any signal of length M running from 0 to $M-1$, such as an absorption cross-section, and F is any signal of length N running from 0 to $N-1$, such as the instrument function of the DOAS instrument. M and N are indices representing, for example, a spectrum running from λ_1 to λ_2 . The resultant signal y , the convolution of the two signals, is an $N + M - 1$ point signal running from 0 to $N + M - 2$. By the above equation, each point of y at index i can be calculated individually⁷⁰. For instrument or filter functions F larger than 64 data points, convolution using equation 5.13 becomes relatively slow. By the convolution theorem, convolution in the time domain, as in equation 5.14, is equivalent to multiplication in the frequency domain. Thus, equation 5.14 can be expressed for the frequency domain as:

$$y(i) = \mathfrak{F}^{-1}[\mathfrak{F}(h(j)) * \mathfrak{F}(F(i - j))] \quad (5.15)$$

where \mathfrak{F} is the Fourier transform to the frequency domain and \mathfrak{F}^{-1} the inverse Fourier transform to the time (wavelength) domain ⁶⁸. By equation 5.15, absorption cross-section spectra of trace gases can be convolved with the instrument function of the DOAS instrument, smoothing the high resolution spectra as if it were collected with the DOAS instrument itself. This convolution transforms $\sigma(\lambda_{iHR})$ to $\sigma(\lambda_{iHR})^*$, more representative of a spectrum collected with the DOAS instrument. Again, instrument function in this context refers only to those processes contributing to the resolution of the instrument.

Two important properties of the convolution theorem must be accounted for to ensure a proper convolution. First, both the spectra and instrument function must have the same number of elements prior to transformation to the frequency domain. Secondly, the convolution theorem treats signals as if they were periodic, which can produce wraparound issues if not dealt with properly. The first issue is easily dealt with by padding the signals with zeroes to achieve the same number of elements. The second issue is also dealt with by padding both signals with zeroes to length $M + N - 1$, where M and N are the original signal lengths for the spectrum and instrument function.

An example of this convolution is shown in Figure 5.7, using the NO_2 absorption cross-section of Figure 5.4.

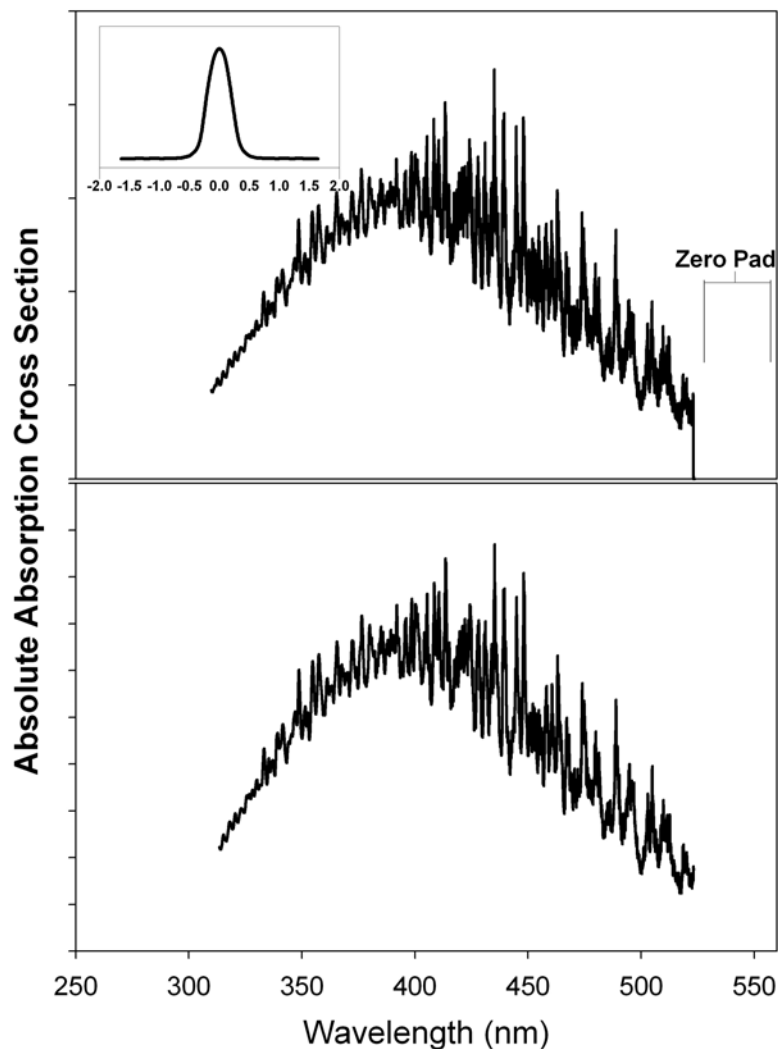


Figure 5.7: Convolution of the absorption cross-section of NO₂ by the instrument function of a DOAS spectrophotometer. In this case, the convolution was implemented by multiplication in the frequency domain.

The graphs shown in Figure 5.7 were obtained following the convolution routine as detailed by Press and adapted for implementation in Mathcad⁷¹. For practical purposes, however, the time consuming process of convolution as described above has been incorporated into most software written for the purpose of DOAS spectral analysis, for example the WinDOAS and SCIATRAN software implemented in this research^{72,73}.

Note that although spectra collected from outside sources contain the instrument function of the original instrumentation, the resolution of those instruments are typically much finer than that of a DOAS spectrophotometer, and as such can be ignored²⁷. This is demonstrated in Figure 5.8, showing the broadening of a spectral line by a high and low resolution spectrophotometer, as well as the broadening of a spectral line collected by a high resolution instrument (0.2 nm) and subsequent convolution by the instrument function of an Ocean Optics spectrometer (PC2000) used for parts of this research (0.8 nm).

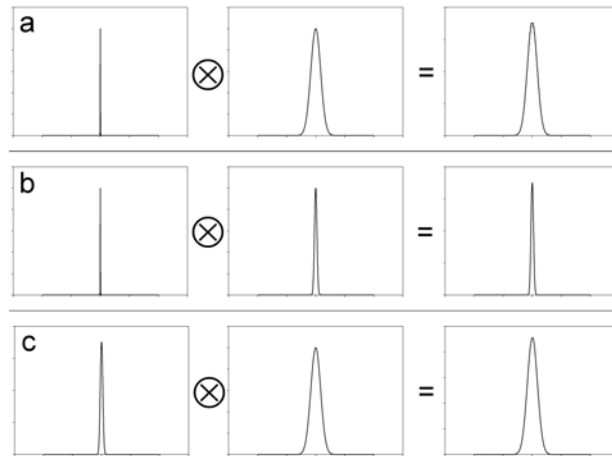


Figure 5.8: Convolution of a spectral line with low and high resolution Gaussian instrument functions. In trace *a*, a spectral line is convolved with the instrument function of the DOAS instrument, with full-width at half maximum 0.8 nm. *b* shows the convolution of the same spectral line with a theoretical instrument function of full-width at half maximum 0.2 nm. *c* demonstrates the convolution of the product in *b* with the lower resolution instrument function of *a*. It can be seen that the product of *c* is identical to the product of *a*. Thus, the instrument function of the high resolution spectrum does not need to be removed prior to convolution.

Again, this method is useful for degrading the resolution of narrow-band spectral features, but does not correct for any slowly varying, broad-band instrumental features (non-resolution component). Removal of those features is accomplished by high pass filtering of the absorption cross-sections, Section 5.7.

5.4c Spline to grid of spectrometer

The final step in the recording of a spectrum by a DOAS spectrophotometer as detailed in Section 5.4a above is the discretization of the continuous spectrum to the individual pixels of the detector. In the case of high resolution cross-section spectra obtained from outside sources, which have previously been pixilated to the detector of the spectrophotometer with which they were collected, this can be thought of as re-mapping the spectrum to the pixels of the DOAS detector. As the high resolution absorption cross-sections have much finer wavelength spacing and different wavelength-pixel mapping functions than that of a typical DOAS instrument, it is often not possible to find matching wavelength points. Therefore, it is desirable to use a mathematical routine to interpolate the high resolution spectra to the wavelength grid of the DOAS instrument, imitating the discretization of the spectrum as described in section 5.4a. The most common approach to the interpolation problem in DOAS analysis is to implement the cubic spline. This method provides a relatively fast means of estimating the value of a point using values surrounding it, and is relatively robust against nonlinearities in the detector's wavelength pixel mapping⁶⁷. A rigorous investigation of interpolation errors in the framework of differential spectroscopy was conducted in 1996 by Roscoe, Fish and Jones, which determined that the cubic spline was superior over both linear and quadratic interpolation

methods over a large range of theoretical spectrophotometer resolutions and wavelength pixel mapping nonlinearities⁷⁴.

Interpolating reference absorption cross-sections to the wavelength grid of a DOAS spectrophotometer, as mentioned previously, is a necessary step in the spectral analysis process if the references are to be fitted by least squares methods to differential optical depth spectra⁷⁴. By this process, the discretization of a continuous or in the case of high-resolution spectra, relatively continuous, spectra can be accomplished. Using the instrument function convolved cross-section of NO₂ from Figure 5.7, the process of interpolation by cubic splines can be demonstrated.

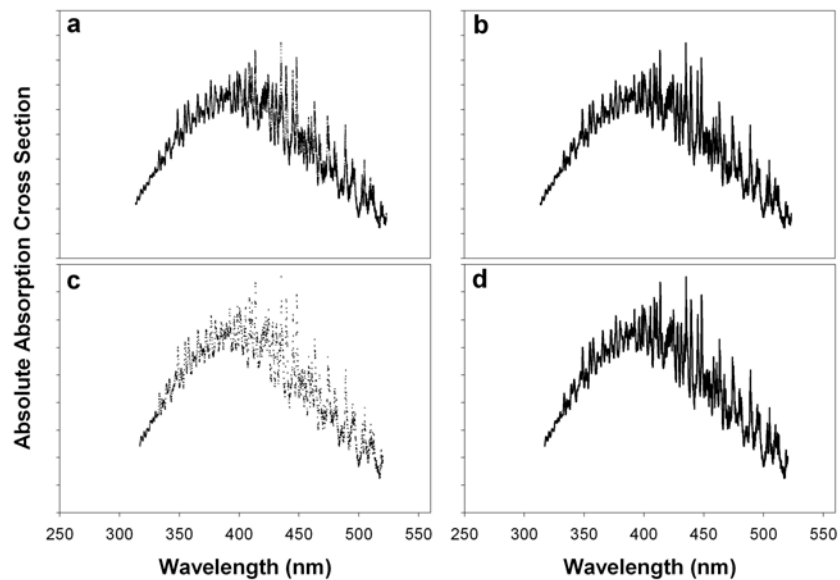


Figure 5.9: Results of a cubic spline interpolation of the high resolution NO₂ absorption cross-section to the wavelength grid of a lower resolution DOAS spectrometer. Traces *a* and *b* show the original spectrum plotted as discrete data points and as a continuous spectrum, respectively. Traces *c* and *d* show the spectrum after a cubic spline interpolation to the relatively rough grid of the DOAS instrument, as discrete data points and as a continuous spectrum, respectively. The reduction in information content between traces *a* and *c* is clearly visible.

Figure 5.9 demonstrates the application of cubic spline interpolation from the fine grid of the original spectrum to the relatively “rough” grid of a DOAS spectrophotometer. Over an arbitrary wavelength region of 415.00 to 416.00 nm, the convolved, high resolution reference spectrum of Voigt³⁸ has $N = 101$ data points, evenly spaced at 0.01 nm intervals. Over the same wavelength region, the detector of an Ocean Optics USB2000 spectrometer used in this research has $N = 12$ data points, evenly spaced at 0.1 nm intervals from 414.93 to 416.03 nm. In this case, an operator could theoretically select manually those data points from the high-resolution spectrum of NO_2 . However, this is not done for the purposes of demonstrating the cubic spline interpolation. Cubic spline interpolation techniques are more representative of the actual process of sampling discrete points from a continuous spectrum that occurs when a spectrophotometer records data. Based on Figure 5.9, it can be shown that despite the ~ 6 fold reduction in information content, the interpolated spectrum strongly resembles the original. The mathematical details of the cubic spline interpolation used to produce the above spectra are given below.

Given a function, or in this case a spectrum, $f(x)$ at known points x_1, x_2, \dots, x_N without an analytical expression of $f(x)$ that allows the calculation of values at arbitrary points, it is still possible to estimate the value at an arbitrary point by means of an interpolation scheme. A very simple scheme, for example, would be to draw a smooth curve through the known points of $f(x)$ and estimate arbitrary values from that curve. In the framework of spectral analysis, however, a more exacting, mathematical means of estimating data points, in this case the points are the wavelength bins of the DOAS detector, is desired. For this, as mentioned above, the cubic spline interpolation scheme

is used. Using the arbitrary function $y_i = y(x_i)$, for $i = 1 \dots N$, and focusing on the interval x_j to x_{j+1} , linear interpolation in that interval can be given as:

$$y = Ay_j + By_{j+1} \quad (5.16)$$

where

$$A = \frac{x_{j+1} - x}{x_{j+1} - x_j} \quad B = 1 - A = \frac{x - x_j}{x_{j+1} - x_j} \quad (5.17)$$

Equation 5.16 is a linear equation with zero second derivative within each interval and an infinite second derivative at each abscissa x_j . The cubic spline is based on finding an interpolation formula that has a smooth first derivative and continuous second derivative both within a given interval and at its boundaries⁷¹. To fulfill both conditions, a cubic polynomial can be added to the right hand side of each interval within equation 5.16, whose second derivative varies linearly from y_j'' to y_{j+1}'' and has zero values at x_j and x_{j+1} .

To accomplish this, equation 5.16 can be re-written as:

$$y = Ay_j + By_{j+1} + Cy_j'' + Dy_{j+1}'' \quad (5.18)$$

where

$$C = \frac{1}{6}(A^3 - A)(x_{j+1} - x_j)^2 \quad D = \frac{1}{6}(B^3 - B)(x_{j+1} - x_j)^2 \quad (5.19)$$

An additional caveat of the cubic spline is that the first derivative of y must be continuous across the boundary between two intervals. Requiring this continuity and using it to derive equations for the first and second derivatives of y is the main aspect of the cubic spline. The first derivative of equation 5.18 can be written as:

$$\frac{dy}{dx} = \frac{y_{j+1} - y_j}{x_{j+1} - x_j} - \frac{3A^2 - 1}{6}(x_{j+1} - x_j)y_j'' + \frac{3B^2 - 1}{6}(x_{j+1} - x_j)y_{j+1}'' \quad (5.20)$$

In order to impart continuity to the first derivative across interval boundaries, equation 5.20 is evaluated for $x = x_j$ across interval x_{j-1} to x_j and set to be equal to the same equation evaluated for the interval x_j to x_{j+1} . This new equation can be written for the interval $j = (2, \dots, N-1)$, with rearrangement, as:

$$\frac{x_j - x_{j-1}}{6} y_{j-1}'' + \frac{x_{j+1} - x_{j-1}}{3} y_j'' + \frac{x_{j+1} - x_j}{6} y_{j+1}'' = \frac{y_{j+1} - y_j}{x_{j+1} - x_j} - \frac{y_j - y_{j-1}}{x_j - x_{j-1}} \quad (5.21)$$

Equation 5.21 represents $N-2$ linear equations with N unknowns y'' . To obtain a unique solution, two further boundary conditions must be specified, and are typically applied at x_1 and x_N . The most common way of applying boundary conditions is to set one or both of y''_1 and y''_N equal to zero, and is frequently referred to as the “natural” cubic spline⁷¹. Additional boundary conditions can be applied in the interpolation process, and in most high quality calculation software packages several options are available to the user. For practical purposes, however, the “natural” cubic spline yields satisfactory results with minimal computational effort.

5.4d Absorption cross-section processing in practice

To this point, the processing of absorption cross-section spectra to make them suitable for inclusion in the differential optical depth least squares fitting procedure has been detailed from the standpoint of replicating the physical processes that occur during the collection of a spectrum by a DOAS spectrophotometer. These processes include convolution with the resolution component of the instrument function to replicate the limited resolution of the DOAS spectrophotometer and cubic spline interpolation to replicate the discretization that occurs when the detector bins a spectrum that is continuous in wavelength to the pixels of the detector. At this point, it is beneficial to

compare an absorption cross-section collected with the DOAS spectrophotometer to that of a high-resolution spectrum from a secondary source that has been processed by the mathematical routines described in Sections 5.4b and 5.4c. An additional step, the least squares regression and removal of a 4th order polynomial, representative of the broad-band instrument function, has been performed for both the measured and processed spectra. This additional step is detailed further in Section 5.7. For the sake of completeness, the example NO₂ spectrum used in previous examples will be used, and compared to an absorption cross-section of NO₂ collected with the Ocean Optics USB2000 spectrophotometer used for parts of this research.

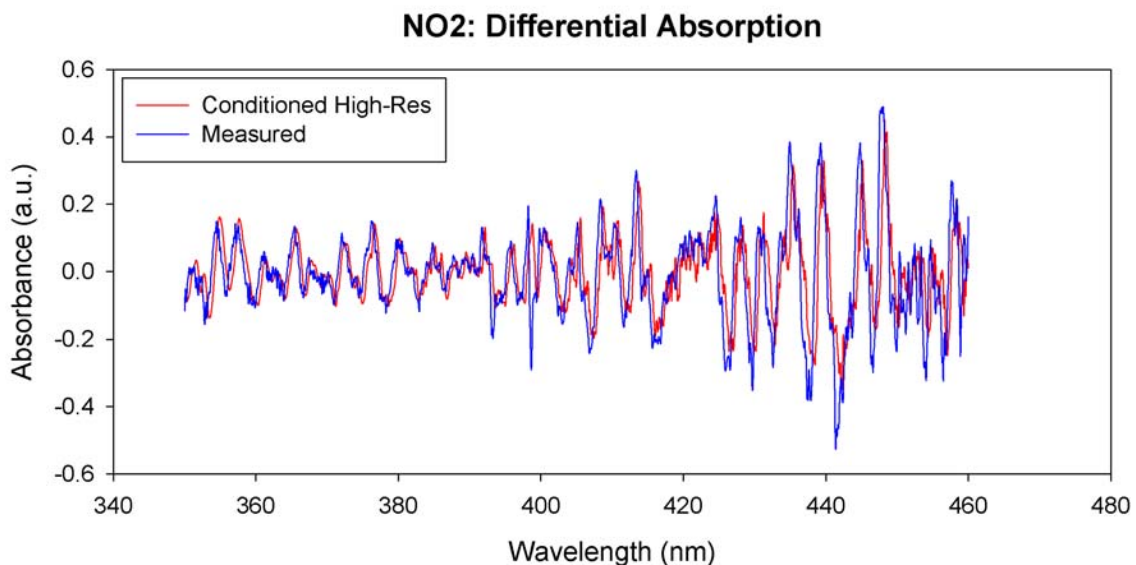


Figure 5.10: Differential absorption cross-section of NO_2 collected by a low-resolution DOAS spectrometer (blue trace) and a spectrum processed from a high resolution spectrum after convolution and cubic spline interpolation (red trace). For comparison, a 4th order polynomial, representing the broad-band instrument function of each instrument, has been removed from both spectra. The slight differences can be attributed to variations in calibration between the two instruments, and can be corrected in the fitting process.

The data shown in Figure 5.10 are quite remarkable, as it demonstrates several important aspects of the processing of spectral data prior to least squares analysis to derive concentration. Firstly, the effectiveness of the instrument function convolution is apparent by comparison of the peak widths between the two spectra. Although not represented for the purposes of visualization, the red trace was interpolated to the wavelength grid of the DOAS spectrophotometer, a reduction in data from 11,000 values to 1080. The above also demonstrates the effectiveness of the regression and removal of slowly varying functions, in this case a 4th order polynomial, as representative of the slowly varying component of the absorption cross-section (equation 5.7) as well as any

broad-band features introduced through instrumentation. The removal of broad-band features from spectral data is discussed in further detail in Sections 5.6 and 5.7 of this chapter. Additionally, Figure 5.10 highlights an important source of error in differential analysis, that is, the slight wavelength misalignment between the reference absorption cross-sections and the DOAS instrument. To correct this misalignment, an adjustment of the wavelength calibration of each reference spectrum is included in the least squares analysis procedure^{67,75,76}. This correction is detailed in Section 5.9.

5.5 Determination of Optical Depth

The primary data that is analyzed in differential optical absorption spectroscopy are collected intensity spectra. As the technique is based on the absorption of light by trace gas species, the analysis is based on the Beer-Lambert Law, equation 5.1. For each intensity spectrum to be analyzed, a Fraunhofer reference spectrum must be selected, which is used to remove spectral lines associated with solar radiation. Reference intensities are chosen such that a minimum amount of absorption features are present. Following equation 5.12, the natural logarithm of the ratio of the reference intensity and spectrum of interest is calculated. The resultant spectrum is known as the optical depth. This division is usually sufficient to remove those spectral features associated with the light source and isolate those features associated with extinction processes, such as scattering and absorption. In a laboratory setting, where scattering is assumed to be negligible, the resultant spectrum would contain only those features associated with absorption. Figure 5.11 shows an optical depth spectrum calculated from scattered solar radiation spectra collected on August 14, 2007 using equation 5.12.

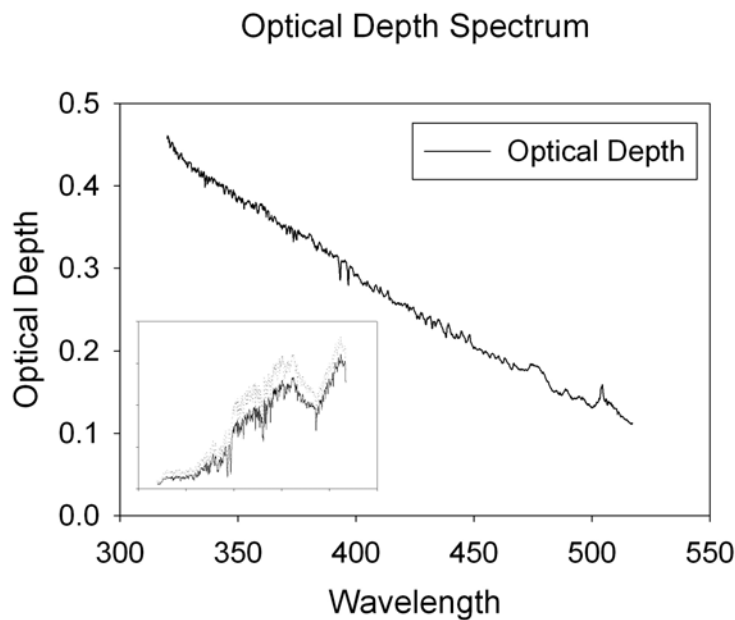


Figure 5.11: Optical depth spectrum, collected on August 14, 2007. The spectrum shown here represents the natural log of I_0 and I , a Fraunhofer reference spectrum and off axis spectrum, respectively, shown in the inset, according to the Beer-Lambert Law. The strong overall slant of the optical depth spectrum is the result of Rayleigh and Mie scattering, as well as the slowly varying components of atmospheric absorbers. It is this slowly varying trend that must be separated prior to least squares analysis to determine concentrations or slant column densities.

For spectra collected in the open atmosphere, the optical depth spectrum contains not only narrow-band absorption features but those features associated with scattering and broad-band extinctions, as in equation 5.11, above. These features are clearly visible in Figure 5.11 as the overall slant or trend in the optical depth. The removal of these broad-band features is a critical aspect of the DOAS technique, and is discussed in Section 5.6, below.

5.6 Determination of Differential Optical Depth

In most DOAS applications, the broad-band features associated with Rayleigh and Mie scattering, as well as absorption, are removed prior to least squares fitting, or included in the fit routine as is the case for this research. In either case, these features are treated as smooth functions^{26,27,30,31,77}. On the surface, the assignment of scattering features to an all-encompassing function seems arbitrary, but is strongly rooted in the physics of light scattering. By equations 5.4 and 5.5, describing the extinction of light by air molecules and particulate matter, respectively, simple representations of scattering can be calculated. It is fortunate that extinction by air molecules and aerosols can be well-approximated by simple power functions, as a full treatment of scattering in the atmosphere would be computationally costly²⁷. A more advanced treatment of atmospheric scattering, necessary for the modeling of solar radiation in the atmosphere, is given elsewhere in this thesis (Chapter 2), as it is not fully relevant to the discussion of differential spectral analysis excepting the slowly varying behavior with wavelength. It was previously demonstrated in sections 5.1 and 5.2 of this chapter that atmospheric intensity spectra and the absorption cross-section spectra of trace gases have a broad-band and narrow-band component, which can be separated using equation 5.7. As the broad-band component of the cross-section is un-quantifiable in the presence of Rayleigh and Mie scattering, the DOAS application is concerned only with the narrow-band component, as in Figure 5.1. Therefore, the spectral analysis task is to isolate these features and remove the un-quantifiable content, that is, scattering and broad-band absorption. As in section 5.1, this can be thought of as the extrapolation and subtraction of those points of a spectrum which do not change rapidly with wavelength. To

accomplish this, a slowly varying broad-band function must be removed from the measured optical depth spectrum as well as the reference absorption cross-sections to be included in the least squares fit to determine slant column densities or concentrations, depending on the experimental setup. It should be noted that while the removal of the broad-band trend in both the optical depth and absorption cross-section spectra prior to concentration determination is mathematically sound by equations 5.7, 5.8, and 5.9, the usual practice is to include the slowly varying component as an additional fit parameter, as is the case in this research ⁷³. This method can be thought of as the superposition of the narrow-band components of the absorption cross-sections onto a broad-band trend. The former method, however, makes for a more effective demonstration of differential absorption.

Figure 5.12 illustrates the use of several broad-band functions to determine the differential optical depth for the spectrum of Figure 5.11, above.

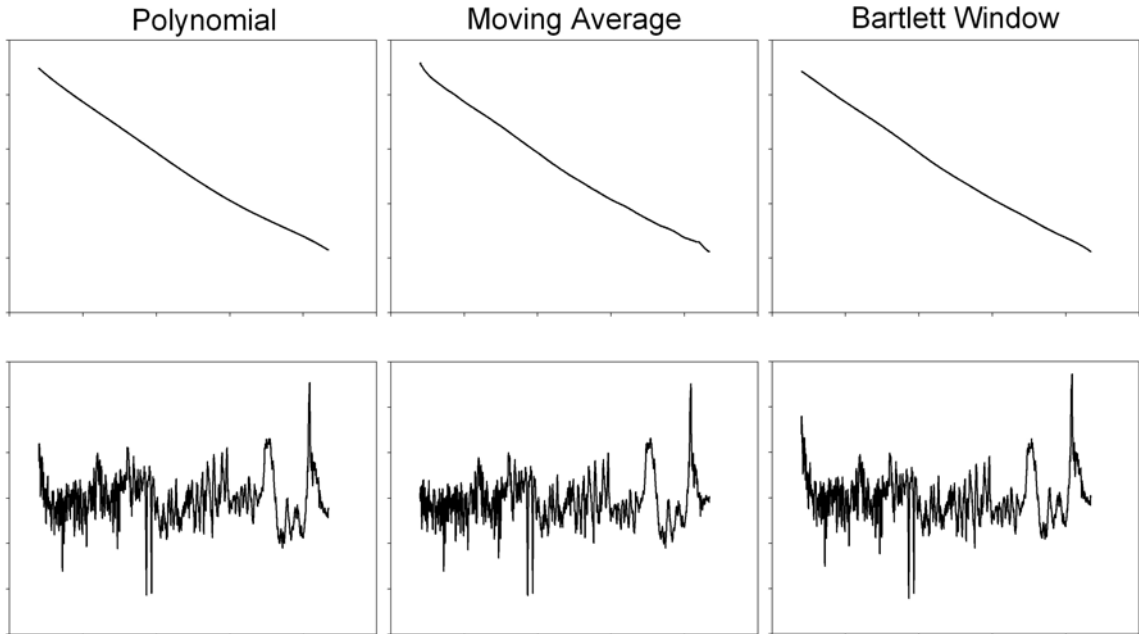


Figure 5.12: Broad-band component of an optical depth spectrum, determined by three methods. The top row of traces show the slowly varying component of the optical depth spectrum, determined by least squares regression of a 4th order polynomial, a moving average smoothed optical depth spectrum, and a Bartlett (triangular) windowing smooth. Below each function is the differential optical depth, calculated as the difference between the optical depth and the respective slowly varying function. Although minor differences are present in each of the three differential absorption spectra, these are largely confined to the end regions.

The regression of these broad-band functions serves as the extrapolation of the smooth component of a spectrum, as demonstrated in Figure 5.1. From Figure 5.12, the choice of function for the determination of differential optical depth, representing the extinction due to Rayleigh and Mie scattering in the atmosphere, has only a relatively minor impact on the final spectrum. It should also be noted that the DOAS technique is concerned only with absorptions that are differential to a consistent function that is slowly varying with respect to the absorption features present. Thus, the broad-band function could also be represented as, for example, a sine or square wave, as long as the same function is

applied over the same wavelength region for each spectrum included in the model and the spacing between the peaks is greater than that of the absorption cross-sections in the model, although such a method would invariably introduce structure, and thus error, into the regression, in addition to being a non-physical representation of broad-band features. In the available software routines for DOAS analysis, the polynomial regression method is typically used, and as such is commonplace in the literature⁷³. Experience has also shown that the polynomial method is more easily implemented and performs faster than other methods of high pass filtering within various differential absorption fit routines, and is the method implemented in this research.

5.7 Determination of Differential Absorption Cross-sections

Analogous to the determination of differential optical depth from measured atmospheric intensity spectrum, the absolute absorption cross-sections to be used in the determination of concentration or slant column density must be processed to remove those features that are slowly varying with respect to wavelength, to conform to the restrictions of equation 5.13. Broad-band features in absolute absorption cross-sections, collected under laboratory conditions in which Rayleigh and Mie scattering are minimal, are attributed to the general shape of the excitation source, the broad-band component of the instrument function, and the natural shape of the absorption spectrum itself²⁷. Figure 5.4 shows the determination of the differential absorption cross-section of NO₂, as determined by a moving average smooth of the original spectrum. In practice, however, absolute absorption cross-sections are truncated in wavelength to match that of the DOAS spectrophotometer, and possibly further truncated to isolate wavelength regions where interference from the light source and other absorbing species is minimal, as discussed in

section 5.3.^{26,27,32}. Figure 5.13 below shows the differential absorption cross-section calculation for NO₂, that is, wavelength truncation, followed by the fit and removal of a 4th order polynomial. The wavelength interval chosen here, 350 to 460 nm, encompasses several fitting windows used in previous DOAS research, as shown in Table 5.1.

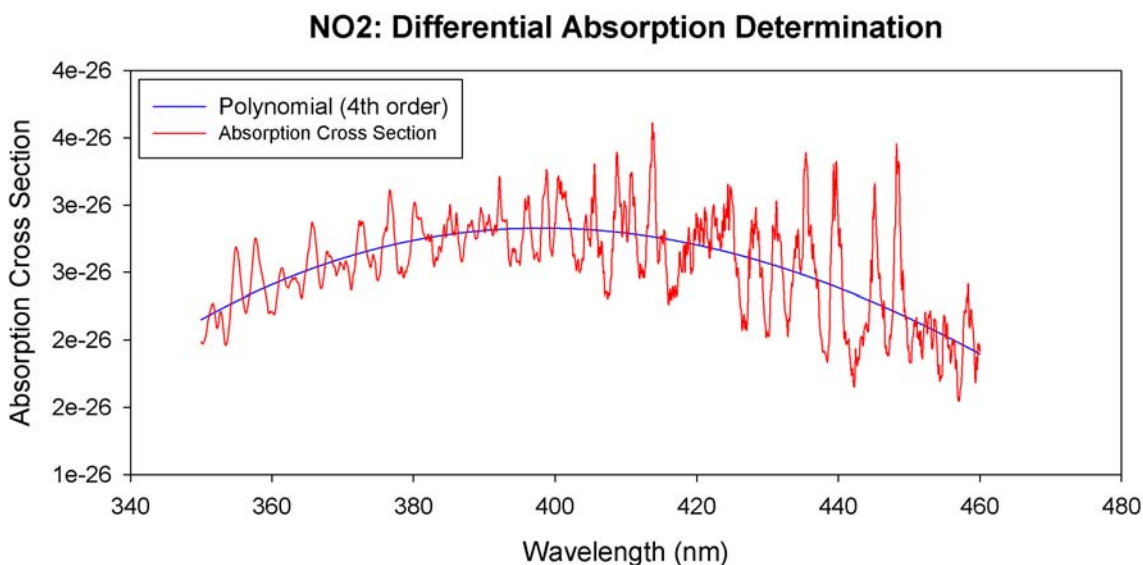


Figure 5.13: The differential absorption cross-section of NO₂. A polynomial of 4th order (blue trace) was fit by linear least squares regression to the absolute absorption cross-section of NO₂ (red trace). Subtraction of this polynomial, representative of the broad-band absorption features as well as the instrumental effects, yields the desired differential absorption cross-section.

Previously, several methods for calculating the broad-band component of spectra were demonstrated, including the regression of a polynomial and the calculation of a moving average smoothed version of the original spectrum. Although the choice of method has little impact on the final appearance of the differential spectra, as shown in Figure 5.12, experience has shown that the moving average smooth method is more

effective over very large wavelength regions, of, for example, 500 nm or more, where a polynomial regression often fails to accurately capture the overall trend in such large wavelength intervals. However, the latter method, in which the spectra are truncated to isolate the wavelength region of interest first, followed by least squares regression of a polynomial, is computationally faster, as there are fewer mathematical processes involved, an important factor in writing and assessing DOAS retrieval algorithms. In either case, the determination of the differential absorption cross-sections should be consistent with the method used to derive the differential optical depth from measured data²⁷. As such, the polynomial regression is implemented in this research.

5.8 Least-squares Regression to Derive Concentration or Slant Column Density

The earliest DOAS measurements were primarily concerned with the detection of various trace atmospheric species, such as NO₃, NO₂, and HCHO. The concept of simultaneous fitting by least squares techniques the differential absorption cross-sections of gas species to measured optical depth spectra was introduced in 1983 and expanded to the analysis of spectra using the sun as a light source in 1987^{31,61}. These early techniques for the least squares analysis of spectra were purely linear algorithms to solve equation 5.13 for unknown quantity c , the concentration of the j^{th} trace gas species. This process can be thought of as the modeling of measured differential optical depth spectra through the linear combination of differential absorption cross-sections⁶¹. The basic linear procedure for spectral analysis is shown in Figure 5.2, shown again below for completeness. Also shown in this figure are the relevant sections of this chapter in which each step is fully detailed.

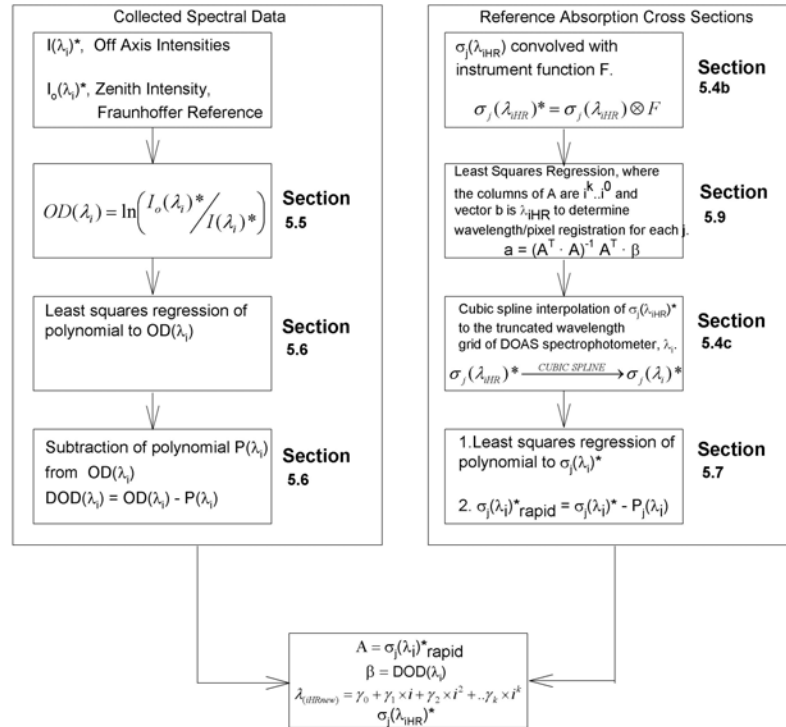


Figure 5.2: Pre-processing of both collected atmospheric intensities (left) and reference absorption cross-sections (right), shown with references to relevant sections of this document. The necessary output for subsequent analysis procedures are the design matrix A , data matrix B , the wavelength pixel mapping function for the j species to be analyzed, as well as the convolved reference absorption cross-sections with their original wavelength grids.

Although more sophisticated algorithms have been developed for the task of DOAS spectral analysis accounting for any calibration variations between the measured and reference data (section 5.9), those portions of the analysis based on the Beer-Lambert Law of absorption are solved by linear ordinary least squares methods^{67,76}. This Additional least squares fitting, for example, the determination of the polynomial representing the broad-band component of a spectrum, is also conducted by procedures detailed below.

Models of the type presented in equation 5.13, above, can be generalized as:

$$y(x) = \sum_{k=1}^M a_k X_k(x) \quad (5.22)$$

where $X_1(x), \dots, X_M(x)$ are fixed functions of x , and y the data to be modeled. These arbitrary functions are known as basis functions, and represent in the DOAS model the differential absorption cross-sections of trace gas species. While the basis functions can be completely non-linear with respect to x , the term linear describes dependence of the model on parameters a_k ⁷¹. A merit, or cost function for the model can be defined as:

$$\chi^2 = \sum_{i=1}^N \left[\frac{y_i - \sum_{k=1}^M a_k X_k(x_i)}{\sigma_i} \right]^2 \quad (5.23)$$

where σ is the measurement error of the i^{th} data point. In the special case of unknown measurement error, σ may be set to the constant value of 1^{71,78}. Selection of model parameters a_k is done to minimize the merit or cost function. The least squares procedure detailed in this Section is presented in matrix form, according to literature precedence^{67,71,78}.

Following the matrix representation of least squares procedures, matrix A , the design matrix, is constructed from the M basis functions at N points x_i as:

$$A_{ij} = \frac{X_j(x_i)}{\sigma_i} \quad (5.24)$$

In the context of differential optical absorption, design matrix A would contain the differential absorption cross-sections of trace gas species, which have been convolved by the instrument function of the DOAS instrument and interpolated to the wavelength grid of the DOAS detector. A vector b of length M can be defined as:

$$b_i = \frac{y_i}{\sigma_i} \quad (5.25)$$

containing measured data y . A third vector containing the parameters to be fitted, a , is also defined. It is necessary here to examine the merit function, whose minimum occurs where the derivative of χ^2 with respect to parameters a_k is equal to zero. The derivative of χ^2 is given by:

$$0 = \sum_{i=1}^N \frac{1}{\sigma_i^2} \left[y_i - \sum_{j=1}^M a_j X_j(x_i) \right] X_k(x_i) \quad (5.26)$$

With rearrangement and substitution, equation 5.26 can be written as:

$$\sum_{j=1}^M \alpha_{kj} a_j = \beta_k \quad (5.27)$$

where α is defined as:

$$\alpha_{kj} = \sum_{i=1}^N \frac{X_j(x_i) X_k(x_i)}{\sigma_i^2} \quad (5.28)$$

and β as:

$$\beta_k = \sum_{i=1}^N \frac{y_i X_k(x_i)}{\sigma_i^2} \quad (5.29)$$

Equations 5.28 and 5.29 can be expressed as matrix operations, with α expressed as:

$$[\alpha] = A^T \cdot A \quad (5.30)$$

and β expressed as:

$$[\beta] = A^T \cdot b. \quad (5.31)$$

In like manner, equations 5.30 and 5.31 can be substituted into equation 5.27, and with re-arrangement to solve for parameters a , given as:

$$a = (A^T A)^{-1} A^T \beta \quad (5.32)$$

the usual presentation of the least squares equations^{71,78}. With these equations, an example least squares analysis of a differential optical depth spectrum is demonstrated below, emphasizing the construction of the design matrix following the recommendations of Sections 5.2 and 5.3 of this chapter.

The optical depth spectra shown in Figure 5.11, collected on August 14, 2007 will be used for the purposes of demonstration here. Again, the task is to fit, by least squares regression, the differential absorption cross-sections of absorbers to the measured differential optical depth. For this example, the wavelength interval 430-455 was chosen, as the analyte of interest is NO₂. Based on Figure 5.5 above, it is initially anticipated that only NO₂ and O₄ will differentially absorb light within this wavelength interval. It is also anticipated that there is a difference in the width of spectral lines present in the solar reference intensity versus that of intensity spectrum of interest. Therefore, an additional synthetic Ring correction spectrum will be fitted to remove any residual solar features. Following the procedures detailed in sections 5.5 and 5.6 of this chapter, the natural logarithm of the reference intensity divided by the intensity spectrum of interest is calculated according to the discrete Beer-Lambert Law of absorption, equation 5.12 above. This optical depth spectrum is then truncated to the chosen wavelength interval, 430-455 nm, and a 4th order polynomial is fitted by least squares regression to the result. This polynomial is subtracted from the resultant spectrum, representing broad-band absorption and scattering features, as in the first trace of Figure 5.12 above. This process of calculating the differential optical depth from measured atmospheric intensity spectra is summarized in Figure 5.14.

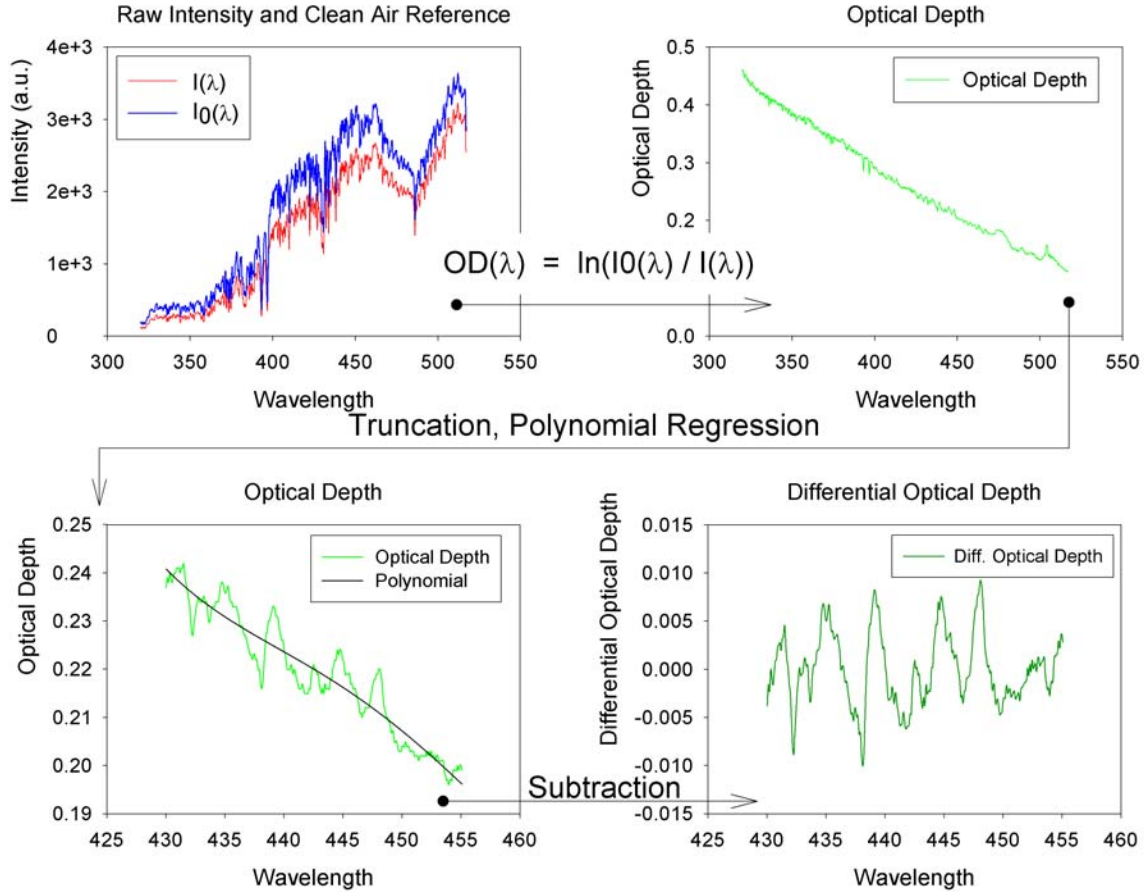


Figure 5.14: The derivation of differential optical depth from measured intensity spectra.

The resultant differential optical depth spectrum is the measured data, y as in equation 5.22. Differential absorption cross-sections of NO_2 , O_4 , and the Ring spectrum are the basis functions of the model, and are gathered in design matrix A , as detailed above. Note that the basis functions have been convolved by the instrument function of the DOAS spectrophotometer, interpolated by cubic spline to the wavelength grid, and truncated to match the chosen wavelength interval.

The construction of the design matrix A is shown in Figure 5.15. Following construction of the design matrix, the coefficients a , representing the contribution of each basis function, are calculated according to $a = (A^T \cdot A)^{-1} A^T \cdot \beta$, as in equation 5.32.

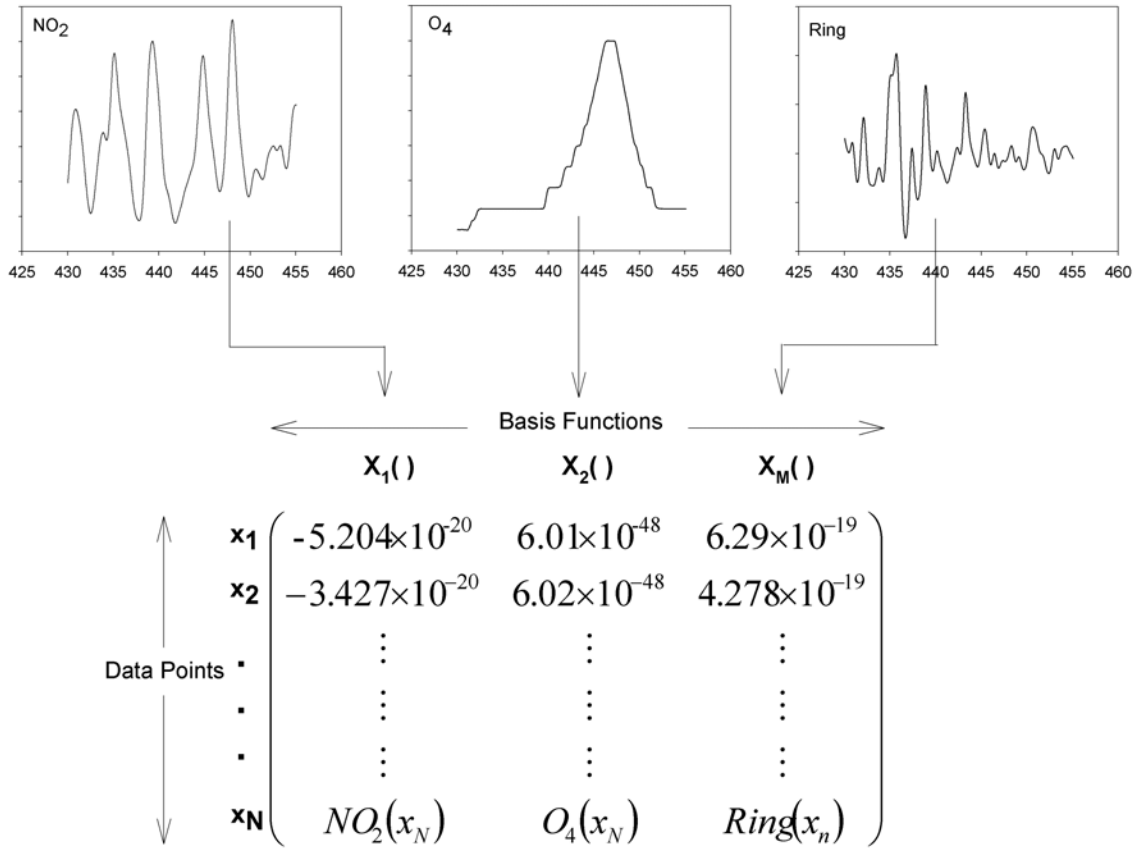


Figure 5.15: Construction of design matrix A, for least squares analysis. The matrix is composed of the convolved, interpolated differential absorption cross-sections of NO_2 , O_4 , and a synthetic Ring spectrum.

In the context of DOAS analysis, the coefficients represent the concentration or slant column density of each species of interest. The modeled spectrum is calculated as the sum of each basis function, multiplied by their respective parameter a . Error analysis, discussed elsewhere, is performed during the least squares analysis, although at this point, visual inspection of the modeled and measured spectra is beneficial. This enables the initial quality of the fit to be assessed, including if the correct differential cross-sections were included in the fit. Examination of the residuals, the difference between

the measured and modeled data, can serve as a means to identify additional absorbers that may be present. The ability to detect unknown atmospheric absorbers is a powerful advantage of the DOAS technique over more traditional means of atmospheric characterization.

Following the example least squares regression of Figures 5.14 and 5.15, the measured and modeled spectra, as well as the fit residual, are shown in Figure 5.16. Based on the example regression of Figure 5.16, it appears that the chosen model approximates the measured data well. However, the magnitude of the residuals is quite large relative to the original data.

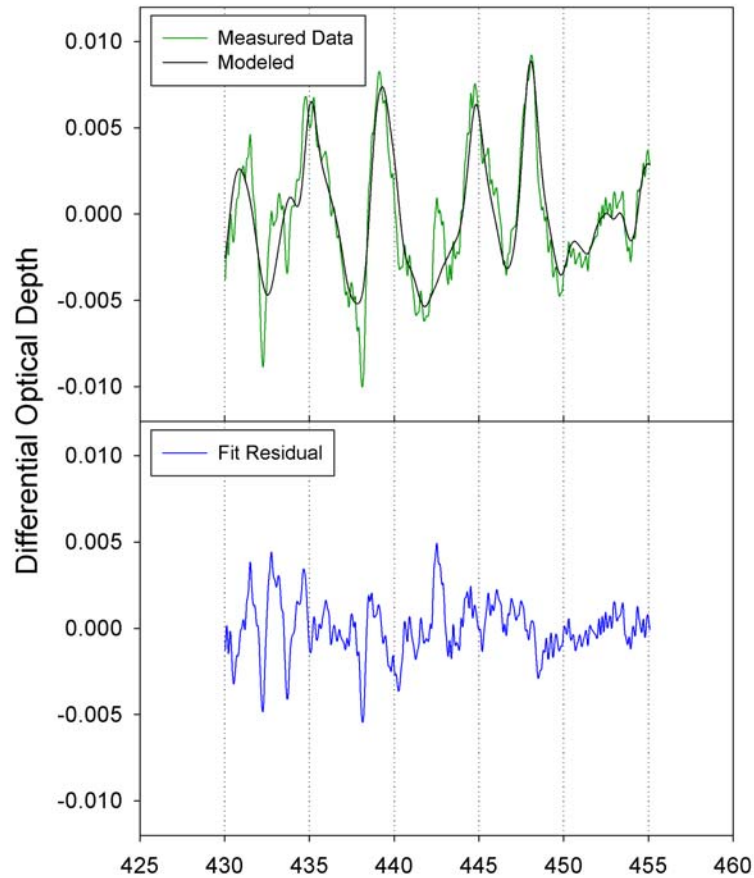


Figure 5.16: Measured and modeled differential optical depth spectra. The modeled spectrum was obtained through a linear least squares regression of NO_2 , O_4 , and a synthetic Ring spectrum to a measured differential optical depth spectra. Residuals (lower trace) were calculated as the difference between the measured and modeled spectra. For this wavelength interval, where NO_2 is the primary absorber of solar radiation as discussed in Section 5.3, the residuals are unlikely to be the result of the exclusion of an absorbing species from the design matrix²⁷. The cause of these relatively large residuals is likely due to slight misalignments between the measured data and the reference differential absorption cross-sections and the incomplete removal of solar features, a common problem in the analysis of solar spectroscopic data.

To correct such errors, most differential analysis algorithms include a calibration correction for the reference data, as discussed in the following section of this chapter.

5.9 Least-squares Regression with Calibration Correction

The linear least squares method presented in section 5.8 is applicable if the reference absorption cross-sections as well as the differential optical depth spectra have, after cubic spline interpolation, the same calibration function, or more commonly in the DOAS literature, wavelength-pixel mapping function. That is, the functions describing which wavelengths are registered by each pixel of the detector are identical. For reference absorption cross-sections collected from outside sources using different instrumentation, this situation is unlikely. Further discrepancies in the wavelength-pixel mappings can be introduced by different measurement conditions, such as temperature and pressure, changes in which can alter the dispersion and thus wavelength registration of the DOAS spectrophotometer⁶⁷. These discrepancies were clearly illustrated previously in Figure 5.10, above, showing the NO₂ absorption cross-section as recorded by the DOAS spectrophotometer and as calculated from a high resolution cross-section. Misalignment between the reference absorption cross-sections and the measured data can lead to concentration or slant column density estimations of poor quality. Several solutions have been proposed to deal with the effects of wavelength misalignment, all based upon the process of iteratively modifying the calibration function of the reference spectra while at the same time maintaining the linearity of the absorption phenomenon as described by the Beer-Lambert Law^{67,75,76}. As with all of the algorithms implemented in the analysis of differential absorption spectra, these methods attempt to replicate, as closely as possible, the physical phenomena involved in the collection of spectroscopic data. In this case, the process can be viewed as the recalibration of the reference absorption cross-sections to more closely match the calibration of the DOAS instrument,

followed by the linear least squares analysis as presented in Section 5.8, replicating the linear relationship between absorption and the concentration of the j^{th} species. The details of this method along with a sample application are given below.

During the collection and recording process of a spectrophotometer, light is dispersed by the wavelength separation device onto the pixel array of the detector. Each individual pixel records the intensities of a range of wavelengths, which is subsequently recorded as a single intensity at a central wavelength. The signal intensity $I(i)$ at the i^{th} pixel can be expressed by the integral:

$$I(i) = \int_{\lambda(i)}^{\lambda(i+1)} I(\lambda) d\lambda \quad (5.33)$$

and is applicable to each pixel i of the detector, in the absence of instrumental faults⁶⁷. Note that the convention of using an asterisk to denote spectra which have been collected or convolved by the instrument function has been dropped, as it is assumed that all spectra subjected to this alignment procedure have previously been conditioned for the linear regression. The smaller this range of wavelengths is about the central wavelength of each pixel, the finer the resolution of the instrument. Equation 5.33 is inherent to each instrument, and represents one factor in the overall resolution of that instrument. The central wavelength assigned to each pixel across the detector array, however, must be defined by the operator. Assignment of central wavelengths for each pixel is the process of wavelength calibration for a spectrophotometer, and the usual procedure is to measure the spectra of several species or light sources with features appearing at well-known wavelengths, followed by the assignment of central wavelengths by mathematical means to each pixel⁷⁹. The usual mathematical method is to define a function, usually a

polynomial, which describes the relationship between pixel number and central wavelength⁸⁰. For a typical array detector, the calibration function, also known as the wavelength-pixel mapping function, can be expressed as:

$$\lambda(i) = \sum_{k=0}^q \gamma_k \times i^k . \quad (5.34)$$

The vector of parameters γ_k determines the mapping assignment of wavelengths to the pixels of the detector. Changes to γ_0 introduce an overall shift in the assignment of wavelengths, thus a shift in wavelength of recorded spectra. Changes to γ_1 introduce linear distortions to the wavelength mapping, and can be thought of as a stretching or squeezing of recorded spectra. Theoretically, the calibration function can be extended to $k = \infty$, although for a typical spectrometer, calibration functions beyond $k = 0.2$ (second-order polynomials) are usually unnecessary to fully define the wavelength to pixel mapping^{67,79}. Thus, equation 5.34 can be written for $k = 0..2$ as:

$$\Gamma_1 : \quad \lambda(i) = \gamma_0 + \gamma_1 \times i + \gamma_2 \times i^2 . \quad (5.35)$$

The notation Γ_1 , chosen for consistency with the literature, will be used henceforth to indicate the wavelength-pixel mapping or calibration function of the instrument⁶⁷. Calculation of the coefficients γ_k is a straightforward procedure, following the least squares equations introduced in section 5.8. For $k = 0..2$, as in equation 5.35, the design matrix A is constructed such that its columns contain i^2 , i^1 , and i^0 . Matrix β is constructed from wavelengths $\lambda(i)$. By equation 5.32, the coefficients a resulting from the matrix calculation are the values γ_k . For larger k , the design matrix is simply extended to include all i^k . Iteratively changing the wavelength-pixel mapping of the reference differential absorption cross-sections prior to cubic spline interpolation (Section

5.4c) to the fixed grid of the DOAS spectrometer is the basic process included in DOAS analysis routines to correct for wavelength misalignment prior to least squares analysis.

As an example, consider the conditioned NO₂ absorption cross-section of Figure 5.10, which has been convolved by the instrument function of the DOAS instrument, and interpolated to the rougher grid of the DOAS detector. Prior to interpolation, the spectrum had a wavelength spacing of 0.01 nm, from 311.00 to 523.20 nm, binned to 21,221 individual pixels, arbitrarily numbered 0 to 21,220. By least squares regression, a polynomial Γ_1 , following the form of equation 5.33, can be found to describe the relationship between pixel number and associated wavelength. For the regression, matrix β is constructed from the wavelengths 311.00 to 523.20, and the design matrix A contains columns i^2 , i^1 , and i^0 , where $i = 0..21,220$. For the NO₂ spectrum here, the resultant polynomial is:

$$\Gamma_1 : \lambda(i) = 311.00 + 0.01 \times i + 0 \times i^2 \quad (5.36)$$

In this case, with equal wavelength spacing, the second order term is not required to fully express the wavelength-pixel mapping of the NO₂ spectrum, although the term is included for the purposes of demonstration. Alteration of the first term, equivalent to γ_0 , will introduce an overall shift in the NO₂ spectrum, alteration of the second term will “stretch” or “squeeze” the spectrum linearly, and alteration of the third term introduces higher order changes to the spectrum that are mostly unnecessary in differential analysis of atmospheric spectra⁶⁷. Examples of this effect are demonstrated in Figure 5.17, using the differential spectrum of Figure 5.10, above.

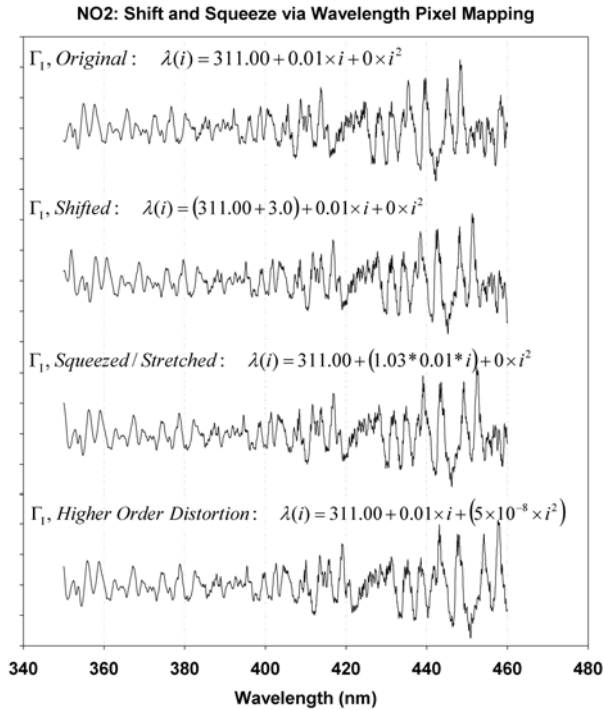


Figure 5.17: NO₂ differential cross-section with altered wavelength pixel mapping functions. Altering the wavelength pixel mapping functions can shift, stretch, and squeeze a spectrum, analogous to changing the wavelength calibration of an instrument. The spectra shown were calculated by first altering the wavelength pixel mapping function as shown, then interpolated by cubic spline to the wavelength grid of the DOAS spectrophotometer.

Note that the spectrum has been truncated in wavelength after adjustment to Γ_1 , for the purposes of comparison.

The example spectra in Figure 5.17 were calculated by arbitrary adjustment of the wavelength pixel mapping function. In the context of differential analysis, the goal of correcting wavelength misalignment is to improve the overall quality of the concentration retrieval, based on the Beer-Lambert Law. Thus, the correction of wavelength misalignments must be performed from a rigorous statistical standpoint. Typically, a multi-step algorithm is applied, combining the linear least squares regression detailed

previously to determine the concentration of each species included in the model with a non-linear Levenberg-Marquardt analysis to derive the wavelength pixel mapping coefficients γ_k from equation 5.35. Non-linear analysis is necessary here, as the relationship between the magnitudes of the fit coefficients a (concentration), and the calibration functions for each differential absorber cannot be expressed linearly. The details of the Levenberg-Marquardt method are presented elsewhere, as a full description of the method is not relevant to the spectral analysis presented in this chapter. The overall process is illustrated in Figure 5.18, adapted from Stutz and Platt 1996⁶⁷.

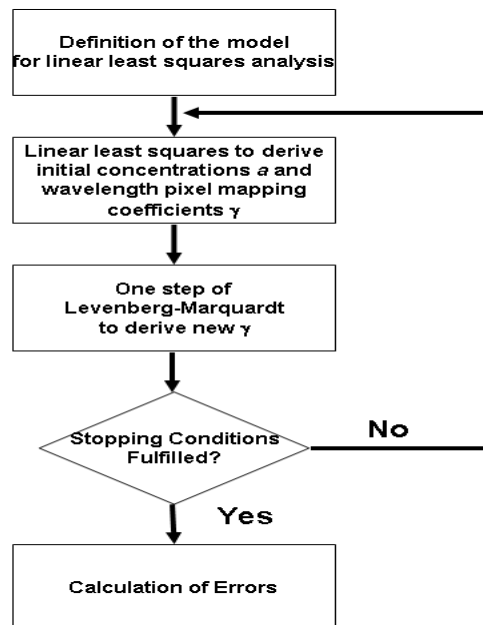


Figure 5.18: Logic flow for a typical DOAS analysis including correction for wavelength misalignment. The process of determining wavelength pixel mapping coefficients is performed as a separate step from the linear least squares analysis to determine concentrations, in accordance with the Beer-Lambert Law of absorption.

By this method, the wavelength pixel mapping functions of the differential absorbers included in the least squares model are iteratively changed until a stopping condition, usually a specific value of the Chi-squared error or a maximum number of iterations, is achieved.

To illustrate the effects of including wavelength alignment in the differential analysis of atmospheric spectra, consider the example regression of Figure 5.16. Previously, this spectrum was analyzed by purely linear means, considering only three absorption features, without wavelength corrections. Prior to the original least squares analysis, the absorption cross-sections were processed according to the methods detailed above, including truncation, removal of the underlying broad-band component of the absorption cross-section, convolution by a 0.8 nm FWHM instrument function of the Ocean Optics DOAS spectrophotometer, and interpolation to a common wavelength grid. Thus, the wavelength pixel mapping function of each of the three spectra is given as:

$$\Gamma_1 : \lambda(i) = 428.944 + 0.0982 \times i + 9.011 \times 10^{-6} \times i^2 \quad (5.37)$$

Following the procedure outlined in Figure 5.18 and adapted for implementation in Mathcad, the regression procedure with wavelength alignment correction yields new wavelength pixel mapping functions of:

$$\Gamma_{NO_2} : \lambda(i) = 428.944 + 0.024 + 0.0982 \times 0.996 \times i + 9.011 \times 10^{-6} \times 0.997 \times i^2 \quad (5.38)$$

$$\Gamma_{Ring} : \lambda(i) = 428.944 + 0.732 + 0.0982 \times 1.077 \times i + 9.011 \times 10^{-6} \times 5.540 \times i^2 \quad (5.39)$$

$$\Gamma_{O_4} : \lambda(i) = 428.944 + 0.491 + 0.0982 \times 1.233 \times i + 9.011 \times 10^{-6} \times 19.514 \times i^2 \quad (5.40)$$

From equations 5.38-5.40, it can be shown that for this example, the initial wavelength pixel mapping functions for each species included in the regression model needed little

modification to reach the Chi-squared minimum. For DOAS analysis, this is a typical result⁷⁶. Comparison to the original purely linear regression shows that in this case, modification of the wavelength alignment had only a minimal effect on the overall quality of the regression, as determined by the magnitude of the residuals. This comparison is illustrated in Figure 5.19.

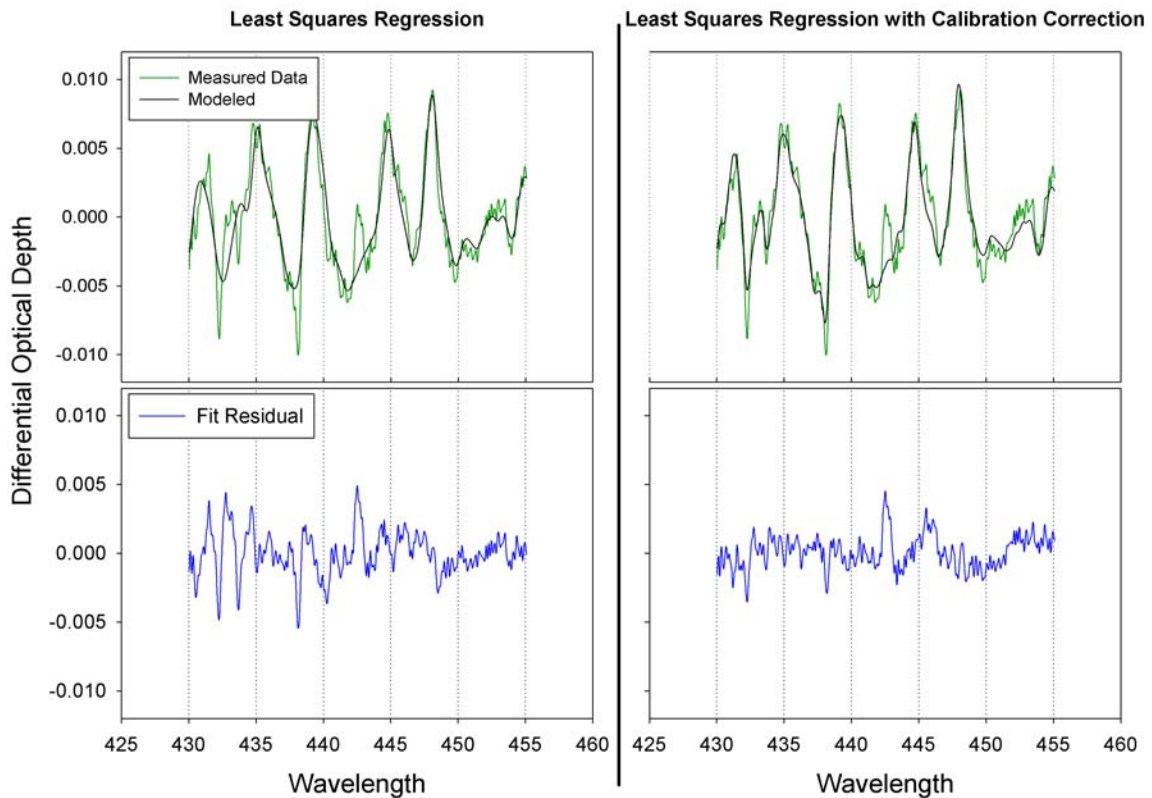


Figure 5.19: Analysis of a differential optical depth spectrum with and without correction for wavelength misalignment. The improvement in the magnitude of the residuals is clearly visible, although the improvement is modest.

The entire DOAS analysis process, including the wavelength calibration process implemented in the data analysis, is summarized in Section 5.12.

The only modest improvement in the magnitude of the residuals for this example is not necessarily indicative of a poorly designed regression model. Differential analysis using natural light sources suffers from the problematic removal of solar spectral lines, despite the subtraction of a solar reference intensity and inclusion of the Ring effect in the regression model¹. A further technique, known as the I_0 effect correction, can be implemented to reduce the presence of solar lines in the residuals, although this is typically only necessary in the presence of very weak absorbers. As such, the method is currently not implemented in this research. The basis of the technique is the modification of the absorption cross-sections to appear as if each was collected using the sun as a light source and not a relatively smooth artificial light source. This is very similar to the instrument function convolution necessary to replicate the limited resolution of the DOAS spectrophotometer, and is detailed in Section 5.2 of this chapter.

Although no strict guidelines exist for the amount of shift and stretch/squeeze that is to be permitted in the wavelength alignment algorithm, indeed, the Levenberg-Marquardt method allows an infinite amounts, it is often prudent to apply limitations to the re-calibration. It should be remembered that absorption of electro-magnetic radiation is a physical process that can be well described using the principles of quantum mechanics. Thus, absorptions recorded by a properly calibrated DOAS spectrophotometer and reference absorption cross-sections collected on properly calibrated instruments should initially be very closely aligned. Experience has shown that significant differences are strong indicators of instrumental problems, poorly

designed regression models, and algorithm errors. Shifts modifying γ_0 by more than a nanometer or two, and shifts/squeezes modifying γ_1 by several tenths of a decimal, should be viewed with skepticism, calling into question the quality of the regression model⁷⁶.

5.10 The Ring Effect

The Ring effect is thought to be the result of in-elastic scattering in the atmosphere, and is often attributed to Rotational Raman scattering⁸¹. The effect of this in-elastic scattering is to broaden the Fraunhofer lines in measured solar spectra. Thus, for spectra collected at different elevation angles, and by extension varying degrees of Rotational Raman scattering, complete removal of these solar features becomes problematic. This introduces interferences with the weak absorptions of atmospheric trace species. To correct for the Ring effect, a correction spectrum is often included in regression analysis, and is treated exactly like any other differential absorption cross-section⁶¹. In this research, a synthetic Ring correction spectrum, calculated by convolution of a high resolution solar spectrum with the rotational Raman spectra of N₂ and O₂ is used for the correction^{48,82}.

5.11 Concluding Remarks on DOAS Data Analysis

The mathematical techniques detailed here are applicable to all differential spectroscopy applications, including satellite, ground based solar, and ground based artificial light source platforms. Despite recent efforts to unify the presentation of DOAS data, the sheer number of individual processes that are performed prior to and during differential analysis necessitate the reporting of several pieces of information, for the purposes of replication by others⁸³. Thus, it is typical to report the species included in the regression model, the wavelength interval over which the data was analyzed, choice

of representative slowly varying function, and the full width at half maximum of the instrument function. Constraints placed on the degree of shift and squeeze allowed by the non-linear analysis of wavelength calibration are also reported. The reporting of errors for the retrieved concentrations or slant column densities is a poorly developed aspect of the method^{67,84}. Typically, the least squares regression error is reported for each species, and often a graph showing an exemplary analysis, is included in publications. The exemplary analysis will show the residuals of the analysis, which, as stated above, provides a good first approximation of the quality of the regression model chosen. However, the residuals present a statistical challenge, as they do not scatter randomly about the model function, nor is the content of a particular channel of the residuals independent of adjacent channels⁸⁴. Despite three decades of testing and refinement, statistical analysis in differential spectroscopy is an underdeveloped aspect of the science. The least squares error is therefore an underestimate of the true error, reported between 2 and 5 times less^{67,85}. Other methods have been applied to estimate the true spectral evaluation error, although these methods are often conservative overestimates. For example, the root-mean-square of the residual scatter and peak to peak magnitudes of the residual have been used as estimates of the evaluation error^{86,87}. Therefore, a rigorous statistical method is needed to bridge the gap between the underestimates of error by least squares and the overestimates calculated by alternative means. Although several methods have been proposed, including Monte Carlo methods and the use of synthetic residuals, these techniques are often time consuming, not completely representative of the residuals encountered in actual DOAS analysis, or are difficult to implement in the linear/nonlinear algorithms necessary to compensate for

wavelength misalignments^{67,84}. Development of statistical analysis methods to characterize the evaluation error more fully, which are statistically and physically sound as well as rapidly implemented, is a promising field of differential spectroscopic research.

5.12 Summary of Methodology: Spectral Analysis

The scientific basis and reasoning for the individual mathematical operations necessary for a complete DOAS analysis of collected atmospheric intensities, using reference absorption cross-sections collected from secondary sources, were presented in this chapter. For completeness, a summary of those operations, presented in the order in which they are performed, is given in this section.

Common to all DOAS algorithms are several mathematical operations. The purpose of these operations is to prepare the data and references to make them suitable for analysis, as per the requirements of equation 5.13, replicated here for completeness:

$$DOD(\lambda_i) = \ln(I'_0(\lambda_i) / I(\lambda_i)) = -l \sum_j \sigma_j(\lambda_i) c_j \quad (5.13)$$

These operations can be collectively referred to as pre-processing, as they occurring prior to any quantitative determinations, such as least squares regression, and are common to all DOAS analysis routines. The basic steps are shown in Figure 5.2, repeated here for completeness.

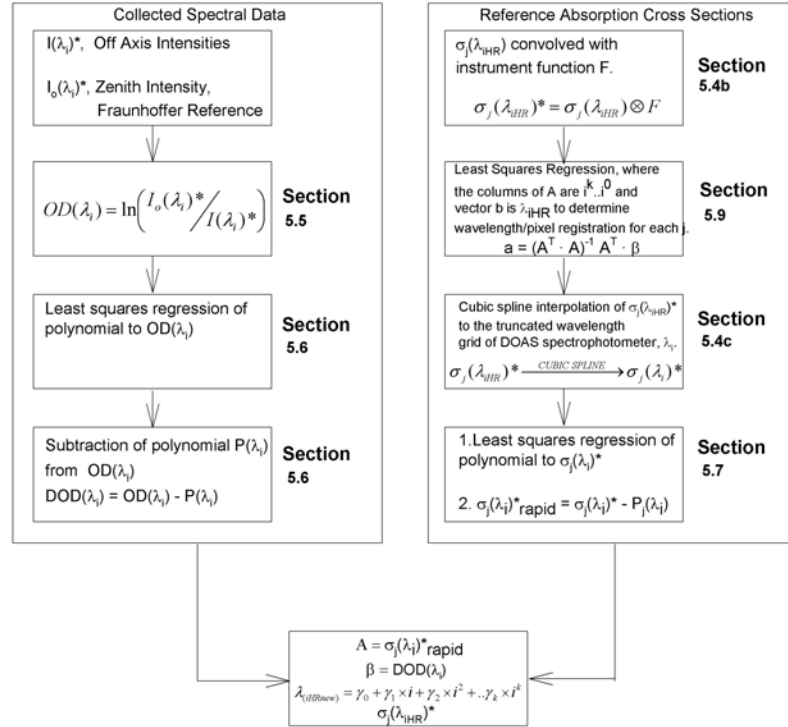


Figure 5.2: Pre-processing of both collected atmospheric intensities (left) and reference absorption cross-sections (right), shown with references to relevant sections of this document. The necessary output for subsequent analysis procedures are the design matrix A , data matrix B , the wavelength pixel mapping function for the j species to be analyzed, as well as the convolved reference absorption cross-sections with their original wavelength grids.

Pre-processing of the collected atmospheric spectra is straightforward, as shown in the left most box of Figure 5.2. Not shown in Figure 5.2 is the selection of the spectral region to analyze and the selection of species to include in the regression model, which of course should be done prior to any subsequent analysis. Also, the truncation of the spectra to the analysis region needs only to be performed for the collected spectra prior to analysis, as the cubic spline interpolation performs this task when implemented. All spectra to be analyzed are divided by a solar Fraunhofer reference spectrum, which is typically collected from a zenith viewing angle near the same time as the off axis spectra

to be analyzed. The negative natural logarithm of the result is then calculated, yielding the optical depth. As detailed above, the optical depth represents an attenuation or departure of the spectral features from the Fraunhofer reference, as per the Beer-Lambert Law of absorption. However, it is known that broad-band departures or differences cannot be quantified by the DOAS observation technique, and therefore are removed. This is done by the regression of a polynomial of third or fourth order to the optical depth and subsequent subtraction of that polynomial. The resultant differential optical depth now still represent absorptions, only now the spectral features represent departures from a function rather than departures from a known reference, as would be the case for a standard Beer-Lambert analysis. The differential optical depth spectrum to be analyzed is collected in a vector β and stored for subsequent analysis. Once differential optical depth has been calculated, no further mathematical processing of the data is necessary.

The pre-processing stage of DOAS analysis must also prepare the reference absorption cross-sections collected from secondary sources for initial analysis. Unlike the differential optical depth calculation, many of the processes presented in Figure 5.2 must be repeated several times if an iterative type of regression scheme is implemented. Regardless of the chosen method, the cross-section processing shown in Figure 5.2 is common to all DOAS analysis algorithms. Firstly, the chosen absorption cross-sections are convolved with the instrument function of the DOAS instrument using a frequency domain multiplication method, as detailed in section 5.4b. The relationship between the pixel number and wavelength for each reference spectrum is established by a polynomial regression. The resultant function is known as the wavelength registration or wavelength pixel mapping function, which is to be used if calibration differences are to be corrected

for in the regression analysis. Convolved cross-sections are then interpolated to the wavelength grid of the DOAS spectrometer, and as with the raw data, are subjected to polynomial regression and subsequent subtraction. The resultant differential absorption cross-sections are assembled into design matrix A for the initial regression analysis. Necessary outputs from the pre-processing stage are 1. The data vector β , containing the differential optical depth spectra to be analyzed and, 2. Design matrix A , containing the convolved, interpolated differential absorption cross-sections. Additional outputs, necessary for more advanced regression analysis methods, are 3. The wavelength pixel mapping functions for each of the j reference absorption cross-sections, which relate the original pixel number to the original wavelength grid of each spectra, as obtained from its primary source and, 4. The wavelength pixel mapping function of the DOAS spectrometer. Note that the reference absorption cross-sections with their original wavelength grids, which have been subjected only to convolution and no other mathematical processing, are also required.

Following the initial pre-processing stage, the differential optical depth spectra are subjected to quantitative analysis. The most basic form of analysis is a linear least squares regression, as shown in Figure 5.20.

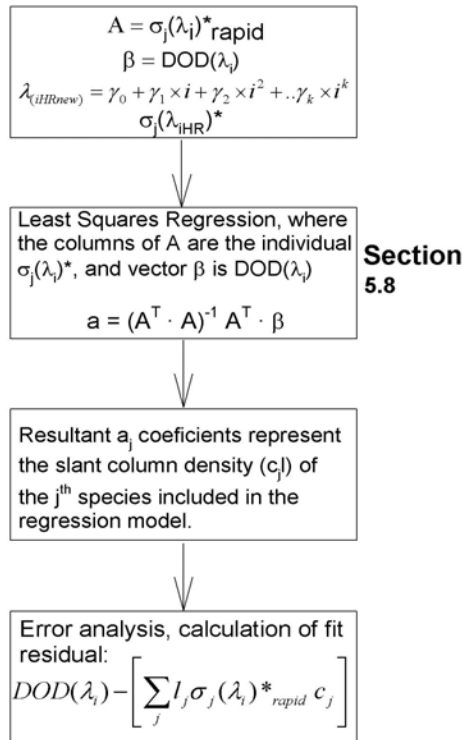


Figure 5.20: Least squares regression analysis of collected differential optical depth spectrum to derive individual slant column densities for the j^{th} species included in the regression model.

Design matrix A , constructed from the convolved, interpolated reference absorption cross-sections and data matrix β are manipulated algebraically to derive the slant column densities of the j^{th} species included in the regression model. The resultant coefficient vector a contains these slant column densities, and the best fit can be constructed by summation of each of the j^{th} absorption cross-sections multiplied by its respective a_j coefficient. Subtraction of the best fit from the collected differential optical depth spectrum yields the fit residual spectrum, a useful quantity in assessing the quality of the regression. The most common expression of error in DOAS spectral analysis is the root mean square of the residuals. Treating the residuals as the difference between the

measured data and the estimator (results of the regression analysis), the root mean square of the residuals can be defined as:

$$RMS = \sqrt{\sum_i (DOD_i - DOD_{i, Modeled})^2} \quad (5.41)$$

In the equation above, DOD_i is the measured differential optical depth, $DOD_{i, Modeled}$ is the estimated differential optical depth from the linear least squares analysis, and i denotes individual wavelengths or pixels.

The linear least squares regression presented in Figure 5.2 is often sufficient for DOAS applications. The accuracy can be improved, however, if the slight misalignments between the reference absorption cross-sections and the DOAS instrument are corrected, as discussed in section 5.9. In procedures of this type, the regression model of Figure 5.2 is combined with a means of adjusting the wavelength pixel mapping functions of each of the j species included in the model prior to interpolation and regression analysis. In this manner, the shape and position of the differential structure can be altered slightly to minimize regression errors, and can be thought of as a real-time re-calibration of the original reference spectra. The entire iterative process is summarized in Figure 5.21, starting with the four outputs from the pre-processing steps.

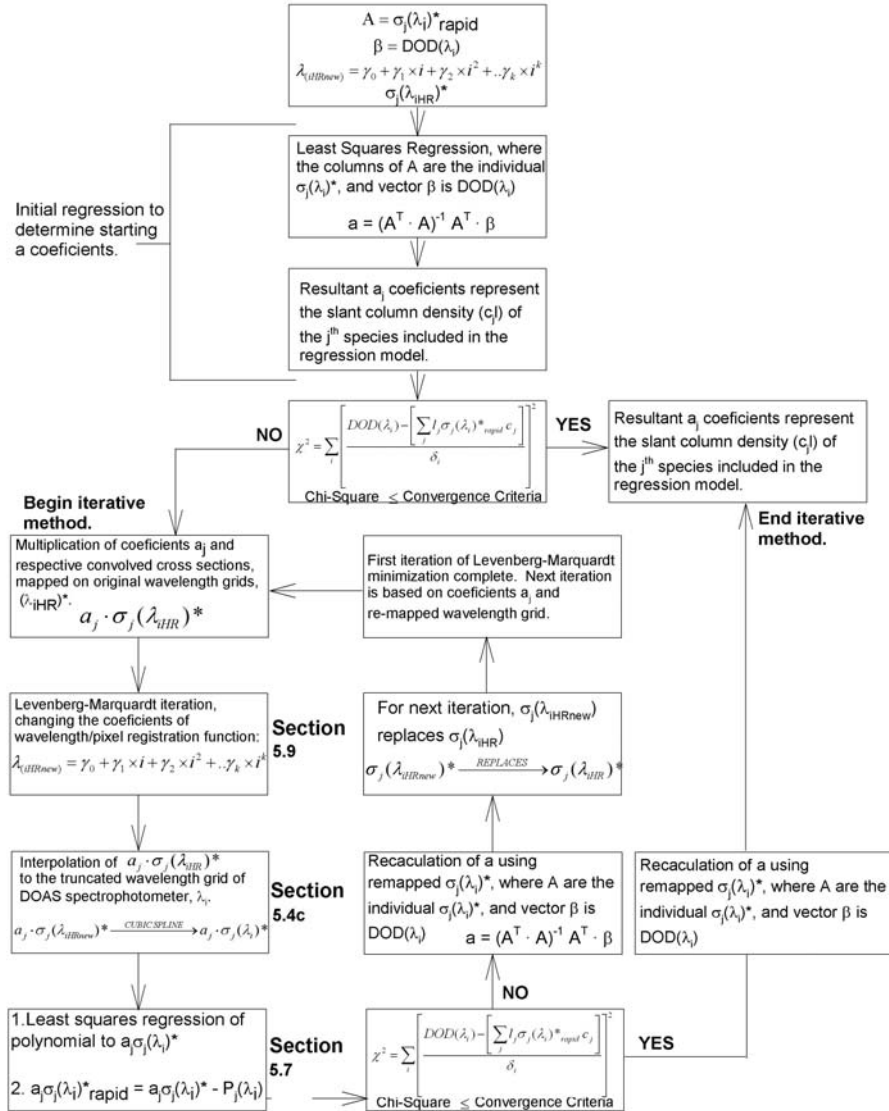


Figure 5.21: Regression analysis, including iterative calibration procedure.

To begin the analysis with calibration correction, an initial regression, as in Figure 5.20, is performed. This calculation provides an initial set of coefficients a , representing the slant column density for the respective species, and an initial Chi-squares value. Should the Chi-squares value be equal to or below a user-defined threshold, typically 10^{-5}

to 10^{-6} , the algorithm terminates without wavelength calibration. If the Chi-squares value exceeds this threshold, the iterative process is started. The original, convolved cross-sections, generated previously in the pre-processing stage, are multiplied by their respective coefficients, a_j . Using the Levenberg-Marquardt iterative method, the wavelength pixel mapping function of each cross-section is modified, thus shifting and stretching the cross-section spectra in wavelength space, as described in section 5.9. These modified cross-sections are then interpolated to the wavelength grid of the spectrometer, subjected to a polynomial regression and subsequent subtraction of that polynomial, as in the pre-processing steps. At this point in the iteration, the Chi-squares value is calculated, and compared to the user-defined threshold. If the value is less than or equal to the threshold, the least squares procedure to calculate slant column density is implemented, and the results of this regression represent the final slant column densities. Should the Chi-squares value be greater than the threshold, a least squares regression is implemented to calculate new slant column densities with the re-mapped absorption cross-sections, which are subsequently passed to the next iteration, along with the shifted/stretched absorption cross-sections and modified wavelength grids. The entire loop continues until the Chi-squares value is less than or equal to the user defined threshold value.

The procedures outlined here represent the basic algorithms implemented in the various DOAS retrieval software packages. Although some variation does exist between specific algorithms, the overall goal is the re-calibration of the reference absorption cross-sections, which produce slant column densities with a minimal amount of error.

The critical and underdeveloped aspect of the science, however, is the quantification and analysis of the residual errors, a key aspect of profiling the vertical distribution of trace gas absorbers.

CHAPTER 6: PROFILE AND CONCENTRATION RETRIEVAL OF ATMOSPHERIC SPECIES

6.1 Slant Column Density

In Chapter 5, the analysis of atmospheric spectra to determine the concentration or slant column density of the i^{th} species with differential absorption cross-section $\sigma_i(\lambda)_{\text{rapid}}$ was detailed for application to all DOAS platforms, independent of the light source. Equation 5.1 expressed the Beer-Lambert Law of Absorption as $I(\lambda) = I_0(\lambda) \exp(-\sigma(\lambda)cl)$, with c equal to concentration in molecules per cm^3 , l equal to path-length in the atmosphere in units cm , and $\sigma(\lambda)$ the wavelength dependent absorption cross-section of an atmospheric absorber in units cm^2 . With an artificial light source or direct-looking natural light source, the path-length l is known, and the regression yields c , the concentration of a particular species. For instruments collecting scattered radiation, the path-length is not readily defined⁶⁴. Therefore, the slant column density is defined as the concentration integrated over path-length l , or⁸⁸:

$$SCD = \int_0^l c(l)dl \quad (6.1)$$

For the unique case of scattered radiation, the differential Beer-Lambert Law is expressed as:

$$DOD(\lambda) = \ln(I'_0(\lambda)/I(\lambda)) = -(\sum_i \sigma_i(\lambda)_{\text{rapid}} SCD_i) \quad (6.2)$$

and the least squares regression procedure detailed in Chapter 5 yields SCDs for each species included in the regression model ¹.

The slant column density is defined along the slant path covered in the (real or simulated) measurement, while the vertical column density (VCD) is defined along a light path parallel to the surface normal. This vertical column extends from the surface up into the zenith, or alternatively from a space or airborne instrument to the surface of the Earth. The SCDs retrieved through the regression analysis of atmospheric spectra represent, as stated previously, the integrated concentration of a species over a particular light path. No information on the location of an absorber can be derived directly from the SCDs themselves, and SCDs are dependent on the position of the light source (solar zenith angle) in the sky. Thus, two measurements of the same vertical profile collected at different solar zenith angles will yield different SCDs ⁶¹. Interpretation of the spectral data, either SCDs themselves or the differential absorption spectra from which they are derived, can be interpreted by two different methodologies. The first method discussed here is that of converting slant column densities to their vertical representation. The second method is the statistical inversion of the differential absorption spectra to retrieve vertical profiles. These two different methodologies, starting from the spectral data itself, are outlined in Figure 6.1.

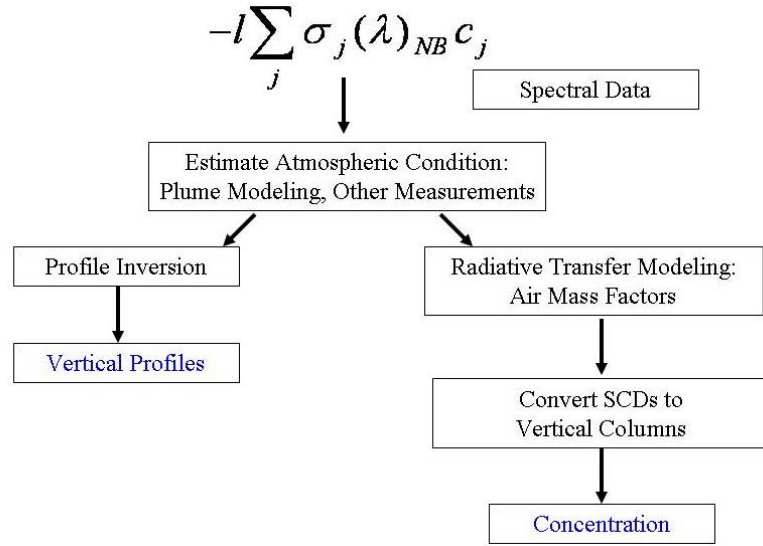


Figure 6.1: Flow-diagram of interpretation of scattered solar radiation data.

A much more useful quantity than the slant column density is the vertical column density, or VCD, which is independent of light path and viewing geometry, enabling the comparison of measurements taken at different solar zenith angles and locations. To convert slant column densities to vertical column densities requires the use of a conversion factor, or air mass factor.

6.2 Classical (geometric) Air Mass Factors

The traditional expression for the air mass factor, or AMF, is given by:

$$AMF = \frac{SCD}{VCD} \quad (6.3)$$

More appropriately, the AMF is expressed with its geometric dependencies as:

$$AMF(\lambda, \vartheta, \alpha, \phi) = \frac{SCD(\lambda, \vartheta, \alpha, \phi)}{VCD} \quad (6.4)$$

where λ denotes wavelength, ϑ denotes solar zenith angle, α denotes the elevation angle

of the instrument's telescope, and ϕ is the relative azimuth angle, the angle between the instrument direction and the sun¹. These geometries are illustrated in Figure 6.2.

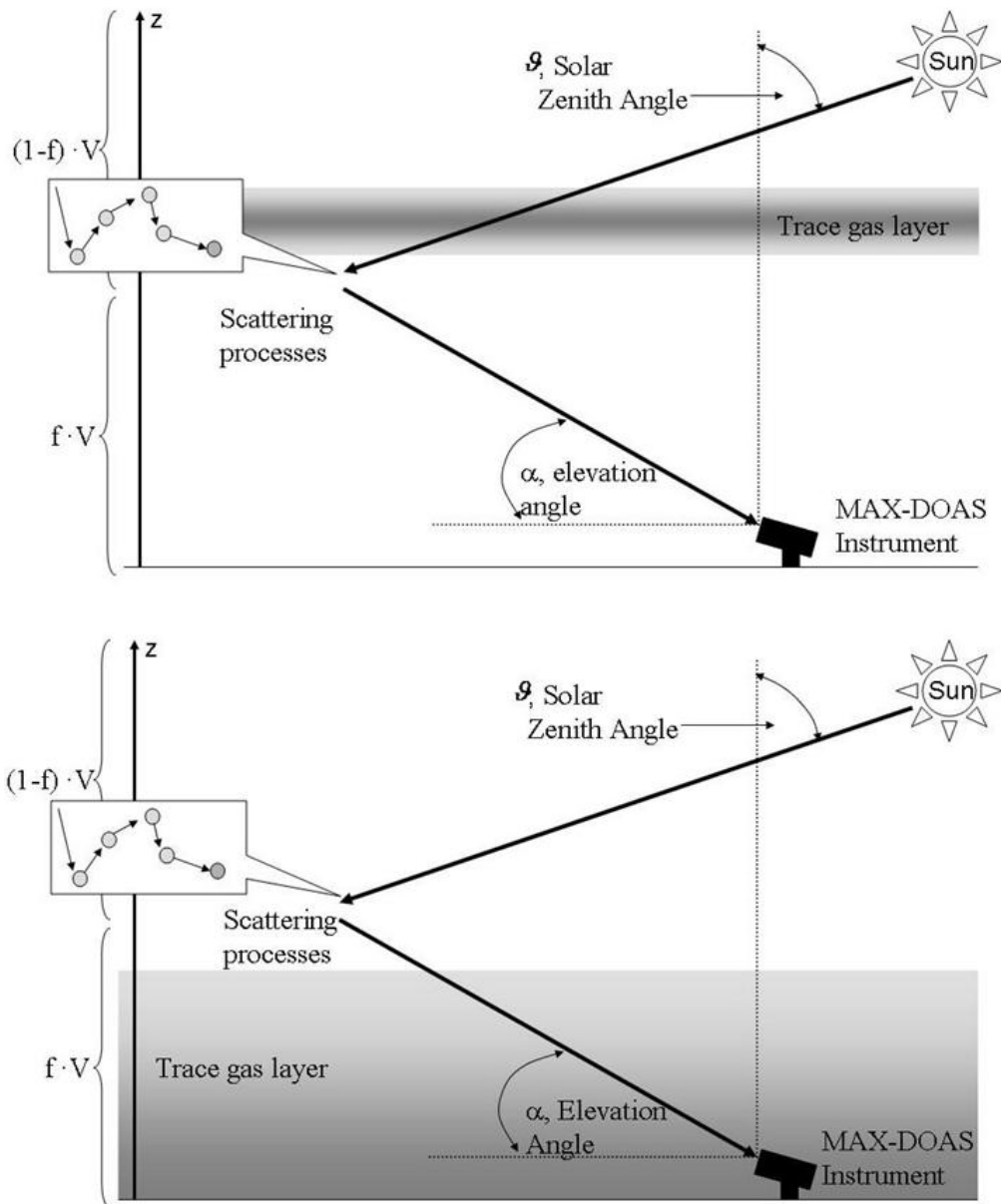


Figure 6.2: Geometries of ground-based MAX-DOAS, considering the single scattering case for an absorber located in the stratosphere (Top) and for an absorber in the troposphere (Bottom).

For simplicity, ϕ , the relative azimuth angle is assumed to be 180° . If f is taken as the fraction of the total vertical column V residing below the scattering altitude, the SCD is approximated as¹:

$$S \approx \left[a \cdot \underbrace{\frac{1}{\sin \alpha}}_{ABL} + (1-a) \cdot \underbrace{\frac{1}{\cos \vartheta}}_{A_{Strat}} \right] \cdot V \quad (a \leq 1) \quad (6.5)$$

By equation 6.5, an absorber in the boundary layer, A_{BL} , enhances the air mass factor approximately by the $\frac{1}{\sin \alpha}$ relationship, indicative of the strong relationship between AMF and the elevation angle of the instrument's telescope. For an absorber located in the stratosphere, A_{Strat} , the dependence of the AMF on solar zenith angle is approximated by the $\frac{1}{\cos \vartheta}$ relationship¹. The geometric methods for the calculation of air mass factors assume single scattering, and neglect many factors, such as surface albedo and Mie scattering. As such, they should only be considered approximations of the true air mass factor. More appropriate methods of air mass factor determination have been developed that enable the calculation of air mass factors for discrete intervals or atmospheric layers. Combined with sophisticated models of radiative transfer, more advanced treatments of the vertical distribution of trace gases can be used, which subsequently enable the estimation of the vertical profile or shape of a trace gas species from multiple measurements of the same profile at different elevation angles α .

6.3 Layer Air Mass Factors

Layer air mass factors, also referred to as box air mass factors, are an extension of the air mass factor concept presented in the previous Section that allows, through

radiative transfer modeling and inversion methods, the retrieval of vertical information for absorbing species, specifically the vertical distribution or profile of a species. It is necessary first to understand the primary data quantity, the slant column density, and its representations. Previously, the slant column density of an absorber was defined as the path integrated concentration of an absorbing species, or:

$$SCD = \int_0^l c(l)dl \quad (6.1)$$

For a single absorbing species, this can be discretized as the sum:

$$SCD = \sum_{j=1}^n c_j(\Delta l_j)\Delta l_j \quad (6.6)$$

Where Δl_j is the length of the j^{th} light path of n total light paths, and c_j is the concentration of the absorber averaged over segment Δl_j ⁸⁹. In the context of trace gas profile retrieval and atmospheric radiative transfer modeling, Δl_j represents discrete layers of the atmosphere, within which the concentrations of trace and abundant gases, aerosols, temperature, and pressure are assumed to be constant. To visualize the discretization of atmospheric absorbers, consider Figure 6.3, adapted from v. Friedeburg, 2003⁸⁹:

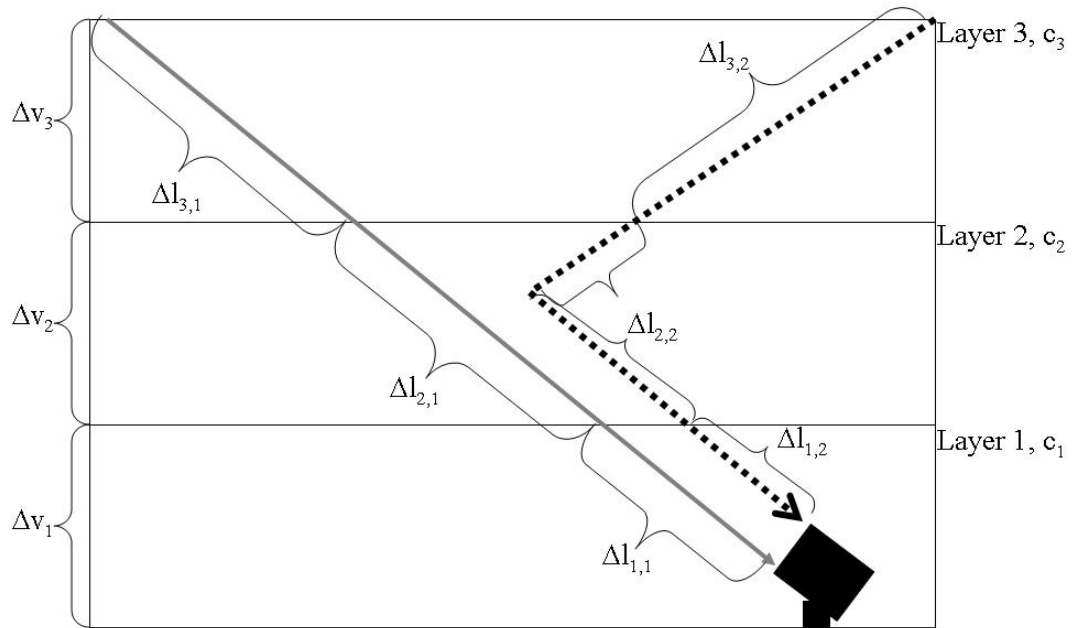


Figure 6.3: Schematic of the Layer Air Mass Factor concept with discrete vertical layers of the atmosphere indicated as Layer 1, 2, and 3, with concentrations c_1 , c_2 and c_3 , within each layer, respectively.

The solid gray line, extending from the top of the atmosphere to the detector, represents light that has not been attenuated. This un-attenuated light path covers Layers 1, 2 and 3. For each segment, Δl , the first index gives the segment or layer number, and the second indicates the light path number. The weight of the concentration in each segment along the un-attenuated path is therefore Δl . In the presence of scattering, however, the weights of each concentration can be changed, as in the light path represented by the dotted arrow. For this light path, which is scattered to the detector in Layer 2, the light paths are different than that of the un-attenuated beam. In Layer 1, light path $\Delta l_{1,2}$ is equal to light path $\Delta l_{1,1}$. However, in Layer 2, path $\Delta l_{2,2}$ is smaller than

that its un-scattered equivalent, $\Delta l_{2,1}$. In Layer 3, path $\Delta l_{3,2}$ is longer than its un-scattered equivalent, $\Delta l_{3,1}$. Thus, the weights of the concentration are smaller in Layer 2 and larger in Layer 3 relative to an un-scattered light path, and a purely geometrical approximation of the air mass factor would overestimate the vertical column density in Layer 2, and underestimate the vertical column density in Layer 3. This limitation can be overcome, however, by expressing the slant column density as the sum of each box in terms of its vertical extension Δv , and the air mass factor for each individual segment:

$$SCD = \sum_{j=1}^n c_j \Delta v_j A_j \quad (6.7)$$

The use of layer air mass factors enables a series of SCD measurements collected under different conditions, i.e., telescope elevation angle, to be combined in a series of linear equations. Thus, the k^{th} SCD can be expressed as:

$$SCD_k = \sum_{j=1}^n c_j \Delta v_j A_{j,k} \quad (6.8)$$

When several SCDs from a series of measurements are taken into account, a linear system can be expressed as ⁸⁹:

$$\begin{aligned} S_1 &= c_1 \Delta v_1 A_{1,1} + c_2 \Delta v_2 A_{2,1} + \dots + c_n \Delta v_n A_{n,1} \\ S_2 &= c_1 \Delta v_1 A_{1,2} + c_2 \Delta v_2 A_{2,2} + \dots + c_n \Delta v_n A_{n,2} \\ &\dots \\ S_o &= c_1 \Delta v_1 A_{1,o} + c_2 \Delta v_2 A_{2,o} + \dots + c_n \Delta v_n A_{n,o} \end{aligned} \quad (6.9)$$

The solution of the above equations, concentrations c at different altitude levels, can also be thought of as the vertical profile of a species. Thus, the layer air mass factors A can alternatively be thought of as “weighting functions” in the framework of DOAS inversion ⁴. In the inversion methods described here, the air mass factors A are formed into a

matrix \mathbf{A} which relates the measured slant column densities to the unknown trace gas profiles. The matrix \mathbf{A} and the noise present in the measured data determine the solvability of the problem. The relationship between this matrix \mathbf{A} the weighting function matrix WF , presented in the following section, can be expressed as⁹⁰:

$$A = -WF \cdot c / I / dz / \sigma \quad (6.10)$$

6.4 Statistical Inversion, Maximum A-posteriori Solution

6.4a: Mathematical description of the Maximum A-posteriori Solution

The layer air mass concept allows the concentration of a gas species to be defined at discrete layers within a model of the atmosphere and the enhancement of the absorption signal within a discrete layer due to scattering, geometry, and several other important parameters. As stated above, MAX-DOAS techniques have the disadvantage that the quantity that is measured has a complex relationship to the desired information, in this case, the vertical profile of a given trace gas⁹¹. Additionally, the problem is ill-posed, whereby there is no unique mathematical solution. Furthermore, there are components of the profiles which contribute no information to the measured quantities, and could, in theory, be infinite in size³. The function in question predicts the results of measurements given relevant physical parameters, and is referred to as the forward model function. Here, the forward model function is a linearized representation of the radiative transfer equation. Inverse methods deal with the inversion of this function, that is, mathematical techniques to retrieve information on the physical state based on remotely sensed data. The maximum a-posteriori method and its applications to the inversion of remotely sensed data have been detailed greatly in the literature, and the details of the

maximum a-posteriori method, following the form of Rodgers, are presented briefly here⁴.

The relationship between the forward model function and the measurement vector can be expressed by the statistical model:

$$y = F(x) + \varepsilon \quad (6.11)$$

where x represents the state vector containing the physical parameters of the measurement and ε represents random measurement noise. Given a forward model, measurements and their error statistics, as well as prior knowledge of the possible states, one can assign a probability distribution function to the possible states that are consistent with the measurements and prior knowledge. Here, square brackets denote probability distribution. Bayes theorem allows for the expression of the conditional posterior pdf of x given y , $[x|y]$, as:

$$[x | y] = [y | x][x] / [y] \quad (6.12)$$

where $[x]$ is the pdf of the prior state, $[y]$ the pdf of the measurement, and $[y | x]$ the conditional pdf of y given x . Taking -2 times the logarithm of the above, known as the Bayes theorem, (thus assuming Gaussian distributed distributions) gives:

$$-2 \ln[x | y] = -2 \ln[y | x] - 2 \ln[x] + 2 \ln[y]. \quad (6.13)$$

If Gaussian distributed measurement error, S_ε is included in the above equation, and $-2 \ln P(y)$ is replaced with a constant, c , the previous equation can now be expressed as:

$$-2 \ln[x | y] = (y - F(x))^T S_\varepsilon^{-1} (y - F(x)) - 2 \ln[x] + c. \quad (6.14)$$

Differentiation of equation 6.14 with respect to state x , indicating the derivative of the forward model with respect to state x , $\delta F/\delta x = K$, and setting the result equal to zero yields:

$$\delta \ln[x | y]/\delta x = K^T S_\epsilon^{-1}(y - F(x)) + (1/[x])(\delta[x]/\delta x) = 0. \quad (6.15)$$

This is an explicit expression for the desired state to retrieve. The matrix K , containing the partial derivatives of intensity with respect to each state parameter at a given altitude and wavelength, is referred to in the remote sensing literature as the weighting function matrix. Continuing under the assumption of Gaussian distributed pdfs, a scalar cost function can be defined using the above equations as:

$$\chi^2 = (y - Kx)^T S_\epsilon^{-1}(y - Kx) + (x - x_a)^T S_a^{-1}(x - x_a). \quad (6.16)$$

It is readily apparent from this cost function that the best solution is one that minimizes both the difference between the measured data and the model (the likelihood), and the information in the prior. Minimization of this cost leads to the maximum a-posteriori solution for the desired state vector, namely:

$$\hat{x} = x_a + (K^T S_\epsilon^{-1} K + S_a^{-1})^{-1} K^T S_\epsilon^{-1}(y - Kx_a). \quad (6.17)$$

The maximum a-posteriori method presented above has been implemented in this study as a program written in the Matlab mathematical programming language. Briefly, the algorithm performs all tasks necessary for a complete inversion of MAX-DOAS measurements. Firstly, the algorithm executes the forward model SCIATRAN, and subsequently collects the weighting function matrices K for the desired state vectors (trace gas or aerosol profiles), as well as model intensities at the wavelengths and altitudes specified in the forward model control files. Both, of course, are a function of

the state vector for that iteration. Following execution of the forward model, external files containing the measured spectral data to be inverted, the a priori profiles of the atmospheric species, and the measured and a priori co-variances are read by the algorithm. Prior to inversion, the measured and modeled data are conditioned for suitability in the algorithm. By the DOAS method presented in Chapter 5 of this manuscript, the measured and modeled data are processed to derive the differential optical depth for each line of sight over the wavelength region of interest, using the corresponding intensity from the zenith viewing angle as the reference intensity $I_0(\lambda)$. Analogous to the spectral data, the weighting functions of each species are also converted to their differential form. Calculation of the differential optical depths and the differential weighting functions are the most time intensive component of the inversion algorithm, aside from the calculation of the weighting functions themselves. The differential weighting function and optical depths are then subjected to the maximum a-posteriori method. An iterative approach is necessary, as the problem is posed as a linear representation of a non-linear process. The results are assessed for convergence according to pre-defined criteria, the algorithm continuing if convergence is not achieved, terminating if convergence is achieved. In this algorithm, the inversion is terminated if the relative change in the scalar cost function is less than a set value, or if a pre-determined number of iterations have been executed. At each iteration, both covariance matrices remain constant.

6.4b: Noise Considerations in Profile Inversion

Throughout this work the assumption of Gaussian noise in the measurements was made. For differential optical absorption spectra, this assumption is often not fully valid,

and some explanation is therefore needed. In most light detection applications, including MAX-DOAS, the noise introduced by the collection of photons by a photodetector (shot-noise) can be described by Poisson statistics. However, in most MAX-DOAS applications, sufficient amounts of photons are collected, and the error contribution of shot noise is rendered very small compared to the optical depths of absorbing species. A second source of error in the spectral data is that of reproducible structure in the residuals. This is often caused by detector artifacts and the absorption features of one or several unknown or un-quantifiable absorbers. Such errors can be non-Gaussian in nature, and be highly correlated. In most instances, however, the fit of a common residual can, in large part, eliminate errors of this kind. Lastly, the occurrence of irregular and non-reproducible artifacts, which can be interpreted falsely as absorption features, are a particular challenge to the classification of errors for the purposes of inversion⁸⁴. The effect of these artifacts is to render typical measures of evaluation error partially invalid. For example, the root means square value of the residual is often used as a measure of the quality of fit in DOAS analysis, and is often used as a measure of the measurement covariance in various Bayesian inversion schemes for remotely sensed data. In the presence of non-random errors, however, this value typically overestimates the degree of error significantly. Categorization of true errors in MAX-DOAS measurements is a significant challenge which, to date, has not been sufficiently addressed. Thus, the assumption of Gaussian error at this point is neither correct nor incorrect relative to other assumed error distributions.

However, in most applications, the magnitude of the errors is typically 2×10^{-5} to 2×10^{-4} , approximately one order of magnitude lower than that of the measured optical depths⁸⁴.

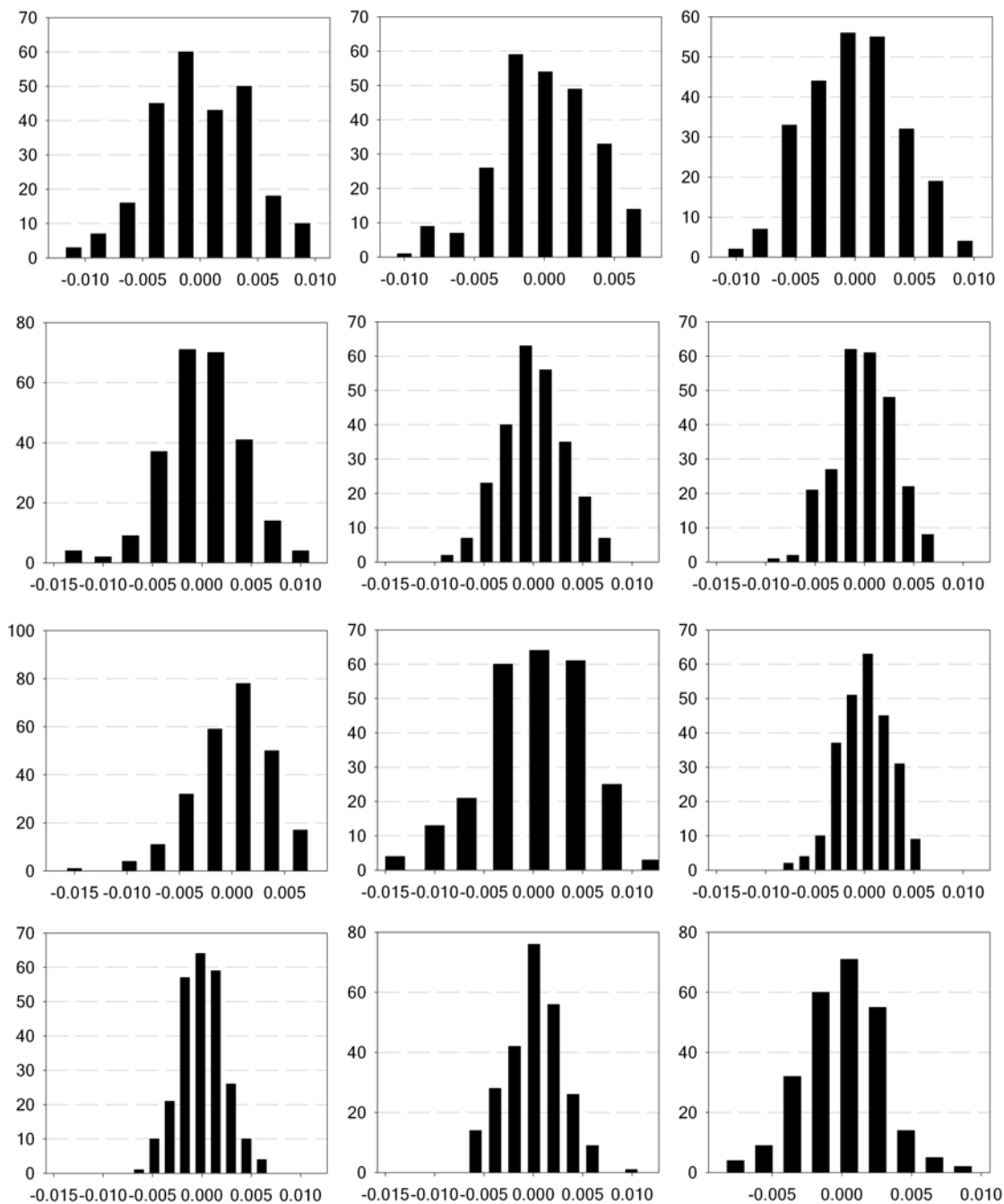


Figure 6.4: Histograms of the residuals from the MAX-DOAS analysis of NO₂.

In Figure 6.4, histograms of residuals from twelve randomly selected analyses of NO₂ from the July 16, 2008 data collected in the Ohio River Valley are shown. The non-

Gaussian distribution of the individual residuals is apparent in several of these plots. When the entirety of the July 16, 2008 NO₂ residuals are considered, however, the results are much more normal in their distribution, as can be seen in Figure 6.5.

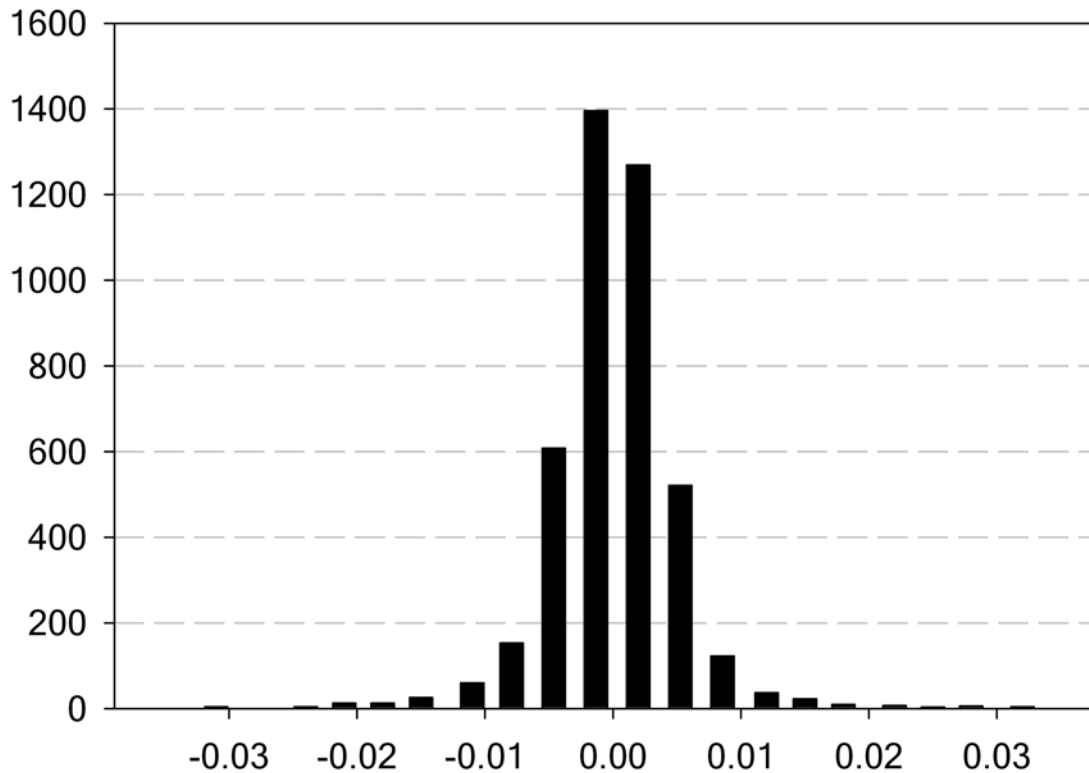


Figure 6.5: Histogram of the full NO₂ analysis for the July 16, 2008 data set.

Thus, for any individual spectrum (line of sight), the residuals may not be perfectly normal in their distribution, but the residuals for a large data set, for example, a complete 12 hour collection period, approximate a normal distribution. It is fully acknowledge that while the distribution of errors may be incorrectly specified for individual spectra, under

most DOAS conditions the magnitude of the errors relative to the measured optical depths is assumed to render this misspecification of minor importance to the resultant inversion. This is especially true when considering large numbers of spectra, such as that shown in Figure 6.5.

A frequency analysis of the residuals of single spectra from the same data set was also performed. For this, a complex fast Fourier transform was performed on the residuals using Mathcad 13 software. In addition to the residuals, an FFT was also performed on a white-noise spectra generated using Mathcad 13 with zero mean and standard deviation 3.9×10^{-3} , as well as on a synthetic differential absorption spectra generated using absorption cross-sections and the resultant coefficients of the DOAS analysis, containing absorption features of NO_2 , O_4 , and HCHO. This synthetic spectrum contains only a small degree of noise, with an RMS value of approximately 10^{-7} . The results of the frequency analysis are shown in Figure 6.6:

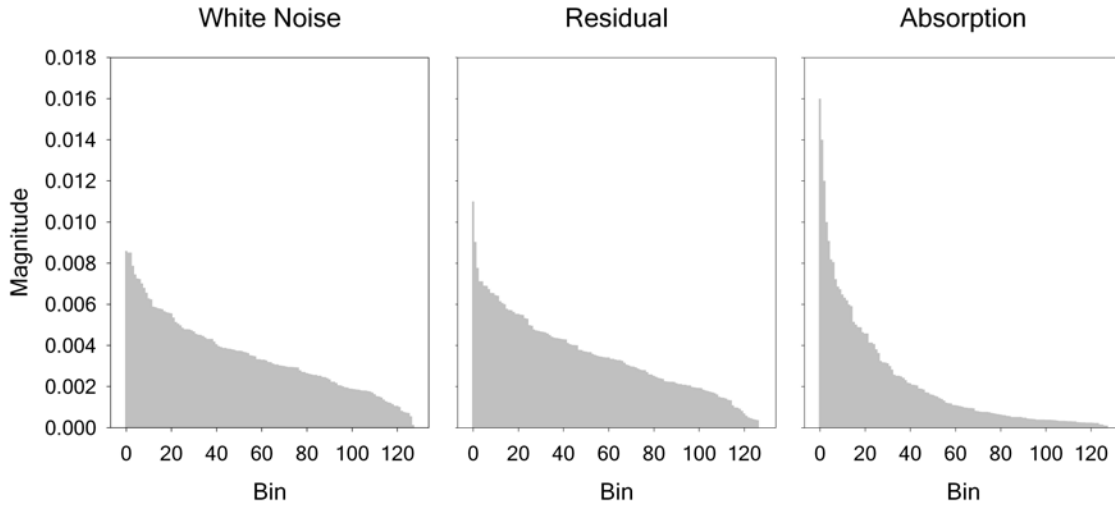


Figure 6.6: Amplitudes of Fourier Transformed synthetic white noise, the residuals resulting from a DOAS analysis of NO₂ from the July 16, 2008 data set, and a synthetic absorption spectra.

The frequency analysis reveals several interesting characteristics of the residual spectra. Firstly, a large proportion of the frequencies of the residual are very similar to that of the pure white noise spectra. This information allows for various carefully chosen noise-reduction techniques to be applied within the DOAS analysis to reduce the magnitude of this white noise. Reductions in the RMS value of the residuals of 40% or better were achieved in this research using carefully chosen de-noising criteria. Such methods introduced only slight differences in the retrieved slant column densities, often 5% or less. However, further inspection of the frequency content of the residual shows that some low frequency information is present. These frequencies are very similar to those in the synthetic absorption spectra, the rightmost trace of Figure 6.6. Thus, it can be assumed that the residuals contain absorption or absorption-like features which cannot be eliminated by common de-noising techniques without affecting information on the absorption of trace species. Therefore, characterization of the statistical distribution of

the low-frequency component of the residuals is critical. These features, however, represent only a small proportion of the error present in DOAS analyses presented in this research. The clear dominance of white noise in the residuals, however, provides a measure of validation to the treatment of spectral measurement error in the inversions of aerosol extinction coefficients in this research as normally distributed with a magnitude given by their root mean square.

6.4c: Inversion of Synthetic Data

Inversion using the maximum a-posteriori method was demonstrated using simulated off-axis spectra generated by the forward model SCIATRAN. This experiment also served to validate the inversion routine developed for this research. Here, the state vector is composed of vertical profiles of the trace gases O₃, NO₂, and HCHO. These profiles were generated using the standard deviation at each altitude from the MPI Mainz climatology database⁹². For O₃, the initial standard deviations for the lowest altitude regions were artificially increased for the purposes of this research, as the initial data set varied very little. Additionally, the concentrations of HCHO were increased from their initial climatology values. Other species, specifically O₂, N₂, H₂O, CO₂, were also included in the simulation, but lack the absorption features necessary for inversion. These species were therefore kept constant for all simulations and inversions. Distributions of O₂, N₂, H₂O, and CO₂ were taken also from the MPI Mainz climatology database for the month of August, at 45° North latitude. The profiles for the three absorbing trace gas species are shown in Figure 6.7:

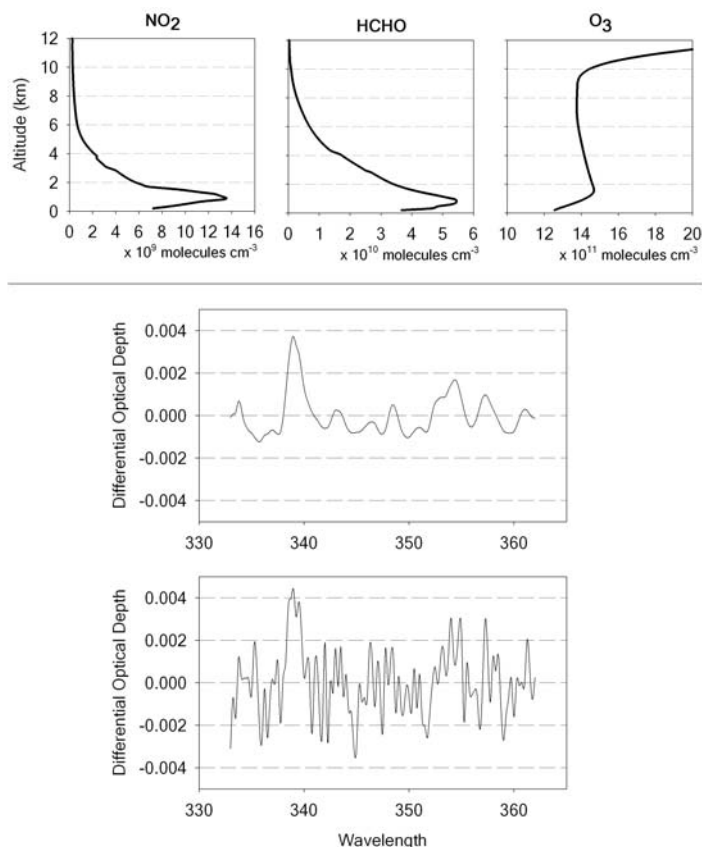


Figure 6.7: NO₂, HCHO, and ozone profiles used to generate synthetic MAX-DOAS data. The synthetic differential optical depth spectra for the 2.5° line of sight is also shown in the lower two traces, both before and after addition of random noise.

A set of five spectra (at the telescope angles 2.5°, 5°, 7°, 10°, 20° and 90°) were generated by the forward model at a constant solar zenith angle of 35°, and an instrument azimuth angle of 95°, for the wavelength region 333 to 363 nm. This particular solar geometry provides a significantly enhanced pathlength through the atmosphere without approaching the angular limitations of the forward model, SCIATRAN. The wavelength region was selected as the absorption by HCHO is quite strong here and spectral analysis within this window is frequently used in other DOAS applications to determine various aerosol optical properties. The observer elevation was treated as being 0.2 km above sea

level, and the top of the atmosphere (TOA) was set at 60 km. To the simulated spectra, Gaussian noise of zero mean and standard deviation 0:0014 was added. The noise-added data are shown for the 2.5° line of sight in Figure 6.6. Using the same synthetic spectra, a second set of data was also generated, this time adding a smaller degree of Gaussian noise, with zero mean and standard deviation 0:000035. These data sets are referred to throughout this research as high-noise and low-noise data, respectively. Both sets of data (low-noise and high-noise) were used as the measurement vector y in separate runs of the maximum a-posteriori inversion algorithm detailed above. A third inversion, using the measurement vector prior to the addition of any artificial noise, was also conducted as a point of comparison.

Using the synthetic differential optical depths with the lower degree of added Gaussian noise as the measurement vector y , the profiles of O₃, NO₂, and HCHO were successfully retrieved using the maximum a-posteriori algorithm. For this inversion, the diagonal elements of the inverse measurement covariance matrix S_{ϵ} , containing the inverse variances of the measured data, was set to 6:0x10⁻⁸. This value was determined from the root mean square of the fit residual resulting from a DOAS spectral analysis described in Chapter 5 of the 10° line of sight, using the 90° line of sight spectrum as the reference intensity. Similar values of the residual RMS were obtained from the other lines of sight. As no correlation was assumed for the fit residuals, the off-diagonal elements of the noise covariance matrix were set to zero. The diagonal elements of the a-priori covariance matrix, S_a were set for each species as the variance at each altitude for the climatology detailed above. The a-priori and first standard deviations for each species are shown in Figure 6.8:

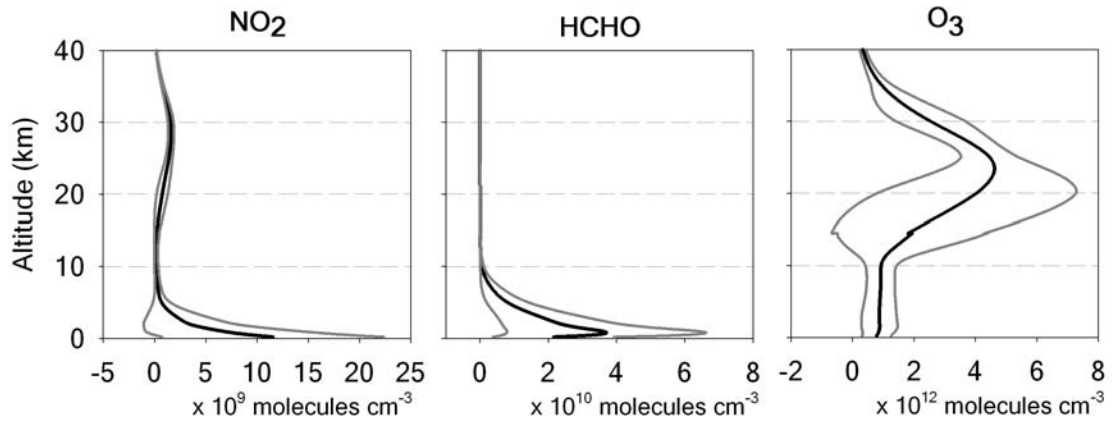


Figure 6.8: A-priori profiles for each of the three species included in the retrieval. Also shown in the figures (light gray traces) are the upper and lower boundaries of the climatology used here. These traces represent the first standard deviation for each species.

As no difference was introduced in the trace gas concentrations between the a-priori profiles and the true profiles above 12 km, the a-priori covariance at these altitudes were set to 0.01% of the a-priori profile, effectively cutting-off the retrieval above 12 km. In addition to stabilizing the retrieval, limiting the altitudes at which the inversion is conducted also reflects the lack of sensitivity of ground based MAX-DOAS measurements to trace gas profiles above approximately 5 km. The results of the inversion using low-noise data are shown in Figure 6.9:

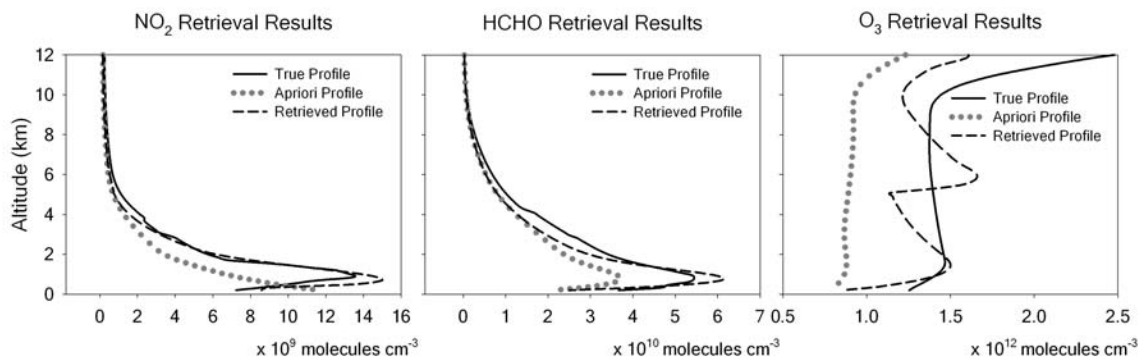


Figure 6.9: True, a-priori, and retrieved profiles retrieved from synthetic differential optical depth spectra with a small degree of Gaussian noise, mean zero, standard deviation 0.000035.

The retrieved profiles from the low-noise data shown in Figure 6.9 demonstrate the performance of the maximum a-posteriori technique. The retrieved profile for O₃ shows a slight agreement with the true profile, capturing the concentration enhancement of the true profile relative to the a-priori, but failing to resolve the shape of the true profile. This result was not un-anticipated, as the high concentrations of O₃ present in the stratosphere lead to a strong O₃ absorption signal in the reference (zenith) spectrum. Consequently, the logarithmic ratio of the off-axis and zenith lines of sight contains only a small amount of information on the O₃ absorption in the troposphere. Thus, the majority of information is contributed from the a-priori, and the presence of O₃ here can be considered a negative control within the experiment. The average absolute difference between the true O₃ profile and retrieved profile below 12km is 11%, with the greatest agreement occurring between 0.58 and 3.2 km. In this region, the absolute percent difference is less than 10% for all altitudes. For NO₂, a higher degree of agreement at all altitude levels up to approximately 4 km was achieved. Lack of structure in the a-priori profile of NO₂ did not significantly impact the retrieved values, and the enhancement of

NO₂ between 1 and 2 km was effectively retrieved, although the exact altitude of peak enhancement was not. The average absolute percent difference for the retrieved NO₂ profile was 19%. Within the altitudes of enhanced NO₂ concentration, the average percent difference is 6%. Lastly, the retrieved HCHO profile also shows strong agreement with the true profile, especially at altitudes below 2 km. Above 2 km, the level of agreement is not as pronounced, capturing the shape but not absolute values, of the HCHO profile. The overall absolute percent difference is 17%, but, as was the case for NO₂, within the region of enhanced concentration, agreement was 12%. The percent variation between the true and retrieved profiles is shown in Figure 6.10. For comparison, using data to which no additional noise was introduced, the average absolute percent differences for O₃, NO₂, and HCHO were 11, 20, and 11%, respectively.

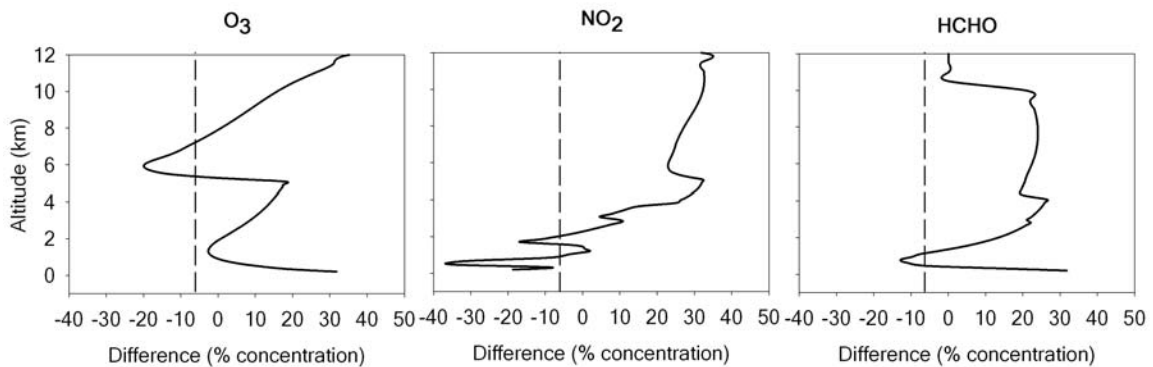


Figure 6.10: Percent difference between the true and retrieved profiles inverted from synthetic spectral data with a small degree of added white noise.

Despite varying degrees of agreement between the true and retrieved profiles, the resultant retrieved spectral data shows remarkable agreement with the measurement vector. At the 20° line of sight, where the smallest differential optical depths occur, the root mean square of the residual was 2.78×10^{-4} , or 36% of the root mean square value of the measured differential optical depth. This is approximately equal to the 0.42 noise-to-signal rms ratio of the original measurement vector. A comparison between the measured and retrieved differential optical depths is shown in Figure 6.11:

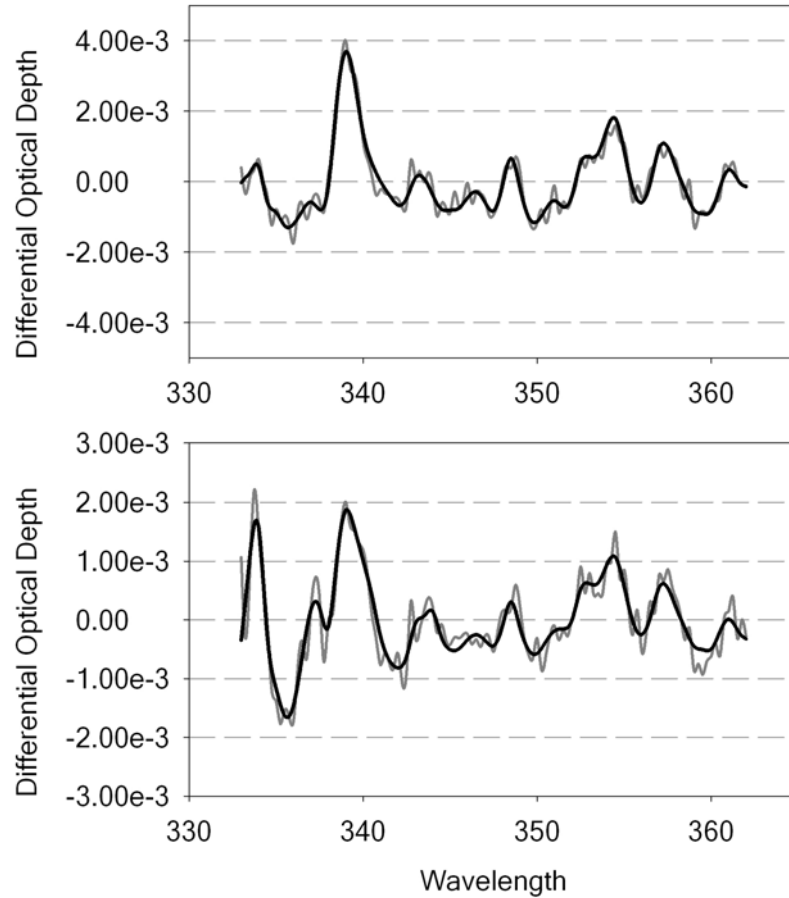


Figure 6.11: Retrieved differential optical depths resulting from the inversion of synthetic data with a small degree of added Gaussian noise, shown with the corresponding measured synthetic data, at the 2.5° and 20° lines of sight.

Analogous to the inversion using the low-noise data, the profiles of O_3 , NO_2 , and HCHO were also successfully retrieved using the maximum a-posteriori algorithm and the differential optical depths to which Gaussian noise of 0.00014 standard deviation had been added. To reflect the additional noise present in the data, the diagonal elements of the inverse measurement covariance matrix S_ϵ were set to 1.3×10^{-6} , as determined from the RMS value of the fit residual at the 10° line of sight. Diagonal elements of the a-

priori covariance matrix S_a were the same as in the inversion using the noise free measurement vector, and again no correlation between altitudes was considered. The resultant profiles from this inversion are shown in Figure 6.12:

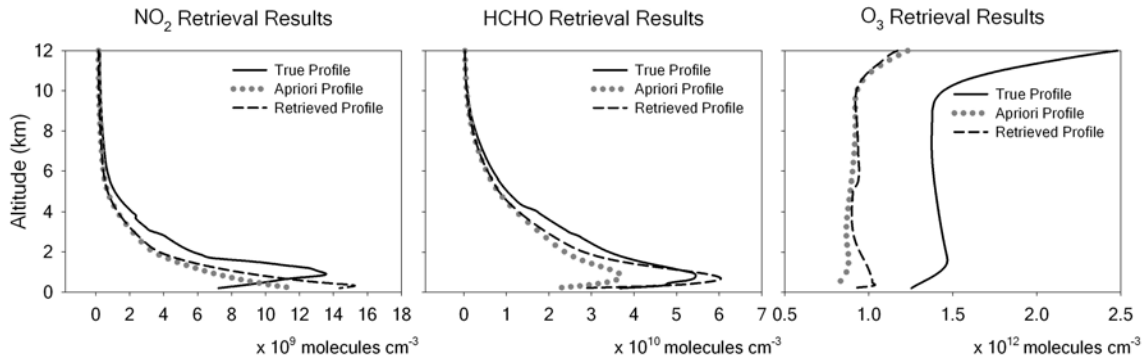


Figure 6.12: True, a-priori, and retrieved profiles resulting from the inversion of synthetic spectral data to which a higher degree of Gaussian noise has been added.

As anticipated, the agreement between the retrieved and true profiles is considerably less than that achieved with the low-noise measurements. The best agreement was obtained with the HCHO profile, likely due to the high concentrations, and therefore large spectral signature in the measured data, as well as the relatively close match in shape between the a-priori profile and the true profile. The average absolute percent difference between the true and retrieved HCHO profile in this case was 17%. As with the inversion of the low noise spectral data, the agreement in the region of enhanced concentration is considerably better than other altitude regions. The inversion fails to capture the enhancement in the NO₂ profile between 1 and 2 km, but some degree of enhanced concentration is retrieved.

For NO₂, the average absolute percent difference is 37% approximately twice that achieved with the low noise data. In this inversion, the retrieved O₃ profile changed very little from the a-priori profile, and little to no information on the true profile was retrieved. The percent difference between the true and retrieved profiles are shown in Figure 6.13:

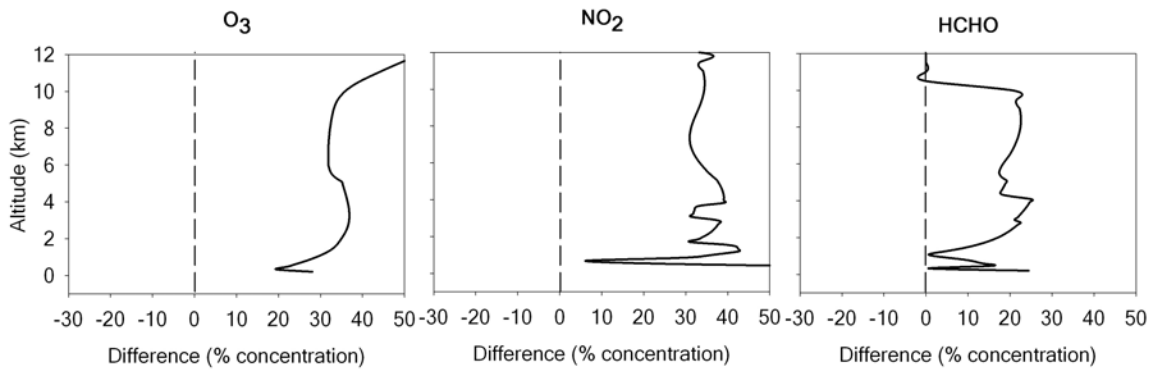


Figure 6.13: Percent difference between the true and retrieved profiles to 12 km, for synthetic spectral data to which a higher degree of Gaussian noise has been added.

As with inversion of the low-noise data set, the retrieved spectral data, shown in Figure 6.14, shows agreement with the measured data despite the considerable difference between the true and retrieved profiles of NO₂ and O₃. Examination of the root mean square values of the residuals at the 2.5° and 20° lines of sight, 1.3×10^{-3} and 1.1×10^{-3} respectively, reveals that convergence was achieved within the level of noise added to the measurements, approximately 9.7×10^{-4} .

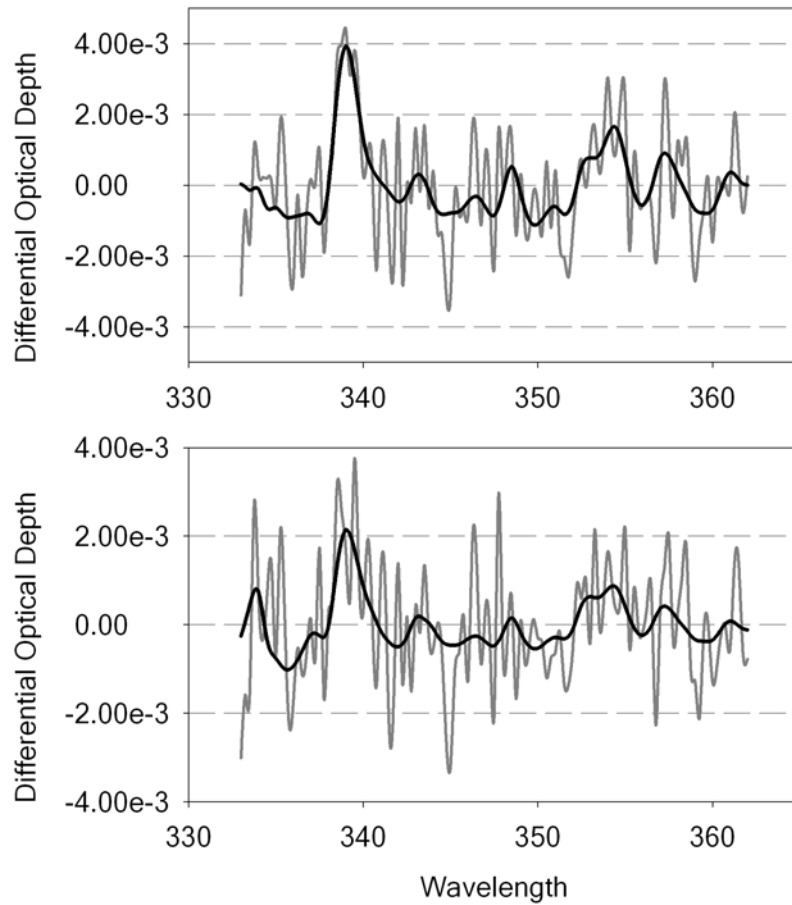


Figure 6.14: Retrieved differential optical depths to which a high degree of Gaussian noise has been added, for the 2.5° and 20° lines of sight.

The maximum a-posteriori method implemented in this work was successful in inverting the simulated measurements, and achieving convergence in agreement with the level of noise added to both sets of simulated data. However, these inversions also demonstrate the potential for solutions that, while statistically optimal, do not accurately represent the true atmospheric state. This can be interpreted in a geometric sense as the convergence to a local minimum on the chi-square error surface, a not-uncommon occurrence in the inversion of non linear problems using Gauss-Newton or Levenberg-

Marquardt type methods⁹³. It should also be noted that the level of noise added to the spectra in the inversion of the high-noise data for this work is significantly greater than what is typically encountered in actual MAX-DOAS applications, where residual root mean square values are approximately 10% of the differential optical depth, dependent upon the instrument, signal strength, and the wavelength region that is analyzed. Improvements to the retrieved profiles presented in this work could have likely been achieved through optimization of the retrieval altitude grid. In addition to the issue of local minima, maximum a-posteriori estimates determined by traditional non-linear search algorithms often reflect a strong dependence on the shape of the a-priori values. This is a reflection of the second term of the cost function, which has an increasingly strong contribution when solutions are far from the a priori state(s)⁹³. The strong influence of the shape of the a-priori profile is undesirable, excepting the case where the prior state is well characterized. However, despite the shortcomings of the maximum a-posteriori method, there are many appealing characteristics of the method, not the least of which are the many post-inversion statistics that can be generated by the method. These include methods to characterize, for example, the contribution of the a-priori values to the solution, and methods to estimate the vertical resolution of the measurement system⁴. The maximum a-posteriori cost function is also useful in instances where a well characterized a-priori profile and covariance data is unavailable. In such instances, a realistic profile shape is assumed, and the off diagonal elements of the a-priori covariance matrix can be artificially constructed as to constrain the shape or smoothness of the retrieved profiles. This method follows the form of Twomey-Tikhonov type regularization, where the maximum and minimum possible values are un-constrained,

whereas the shape of the profile is^{94,95}. In general, the maximum a-posteriori method is an effective tool in the inversion of vertical profiles using remotely sensed data, given the availability of quality a-priori profiles and spread statistics, as well measurements which have well-characterized and minimal noise.

CHAPTER 7: AEROSOL EXTINCTION PROFILES AND TRACE GAS CONCENTRATIONS IN THE OHIO RIVER VALLEY

7.1 Introduction

The MAX-DOAS spectrometer described in Chapter 4 was deployed in the Ohio River Valley for nine days in the summer of 2008; July 15th, 16th, and 17th, August 11th, 12th, and 13th, and September 17th, 18th, and 19th. The area of study, located approximately 20 km south of Wheeling, West Virginia at Latitude 39.92°, Longitude -80.76° is strongly influenced by three coal-fired power plants. Shown in Figure 7.1 is a topographic map of the study area, showing the three coal-fired power plants in question, as well as the two sampling locations, located 1.3 and 6.9 km from Power Plant #1. Spectra were recorded at elevation angles of 0°, 2.5°, 5°, 7°, 10°, and 20° for the July and August sampling periods, with a typical measurement set collected within 25 minutes. During the September sampling period, the 20° observation angle was replaced with a 15° elevation angle. Spectra were recorded at Sampling Site #1, located 1.3 km away from Power Plant #1 on July 15, and September 17 to September 19. Spectra were collected at Sampling Site #2, 6.9 km away from Power Plant #1, on July 16 and 17, as well as August 11, 12, and 13. The MAX-DOAS spectrometer was directed to scan perpendicularly across the emissions plume of Power Plant #1, using an azimuth angle of 162° at Sampling Site #1, and an azimuth angle of 173° at Sampling Site #2. Integration

times for collection ranged from 150 to 6000 ms, depending on atmospheric conditions and solar position, and dark current was subtracted by the instrumentation software.

It has been assumed here that the zenith elevation angle, used as the reference spectrum in the analysis of collected spectra, represents background conditions outside of the plume. In some previous studies of volcanic plumes, reference spectra were collected at different azimuth angles, pointing well away from the plume^{96,97}. This was done to

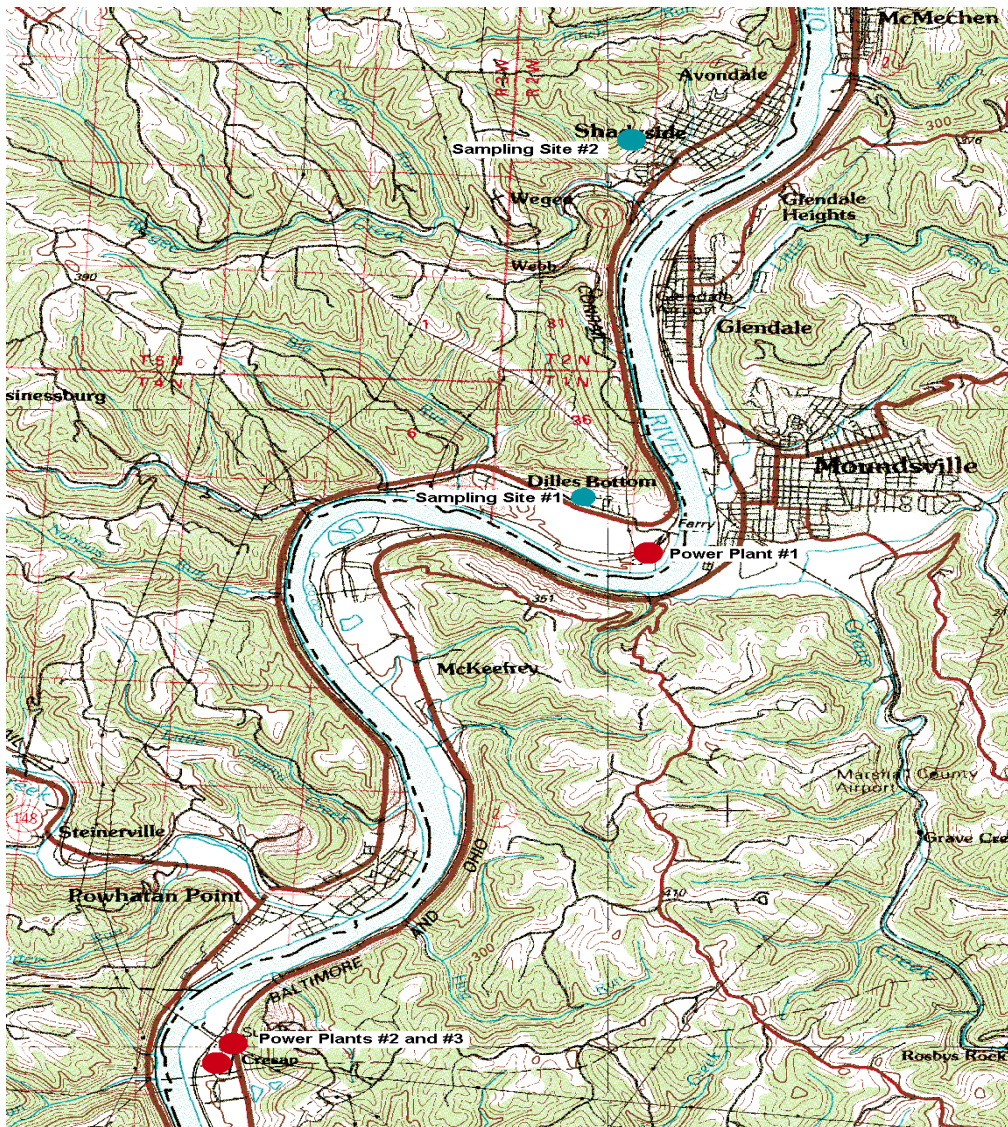


Figure 7.1: Topographic map of the study area. Blue dots represent the two sampling locations, where the MAX-DOAS instrument was deployed. Red dots represent coal fired power plants.

ensure that the slant column densities from spectra collected looking into the plume were the result of only the absorption signature of the plume itself. For the measurement conditions of this research, such lines of sight, along a different azimuth angle, were unavailable, due to line of sight obstructions. Therefore, the slant column density of the highest angular line of sight, determined using the zenith spectra of each measurement series as the reference, taken above the plume, was subtracted from the other off-axis measurements, serving to isolate the slant column density of the plume itself from the total atmosphere.

The Ohio River Valley, a heavily industrialized region, has long been known to be a source of atmospheric NO_x , SO_2 , O_3 , and particulate matter. Long-range transport of these species is of particular concern to the Mid-Atlantic region of the United States, where these species and their deposition is a serious environmental concern. It has been previously estimated that the Upper Ohio River Valley contributes as much as 37% of the total sulfur deposition in this region⁸. Industrial activity in addition to coal combustion, such as chemical manufacturing and metal smelting, contribute a significant amount of particulate matter and particulate matter precursors to the atmosphere in Ohio. 2004 measurements of ambient $\text{PM}_{2.5}$ at The Ohio University Surface Air Monitoring Station by a Tapered Element Oscillating Microbalance estimated number densities of $15.3 \pm 8.1 \mu\text{g m}^{-3}$, slightly above EPA National Air Quality Standards of $15.0 \mu\text{g m}^{-3}$ annual average⁹⁸. Thus aerosols and particulate matter are serious health and environmental concern in the Ohio River Valley. The aim of this study was therefore to utilize the MAX-DOAS technique to monitor remotely the emissions of a coal fired power plant and to retrieve the extinction coefficients of aerosols in this region.

7.2 Aerosol Optical Properties and Prior Profile Determination

In Chapter 6, the interpretation of data collected using MAX-DOAS techniques and the need for accurate radiative transfer modeling to this end was discussed. As aerosols are involved significantly in the scattering of light in the atmosphere, and are much more variable than the distributions of the major gaseous scattering species (O_2 and N_2), determination of their vertical distribution is necessary for accurate radiative transfer in subsequent gaseous species analysis. Aerosols, while not directly measurable by most passive remote sensing instruments, can be measured by using the absorption signal of O_4 , a collisional complex of O_2 , whose concentration is proportional to the square of the O_2 pressure⁹⁹. As the vertical distribution of O_2 , and thus O_4 , is well known, the species serves as a standard whose strength of absorption is largely dependent on the distribution of atmospheric scattering species, in this case, aerosols. It is convenient to MAX-DOAS applications in the UV-visible region that O_4 has several strong absorption bands in this wavelength region, as shown previously in Figure 5.4⁴⁶. Here, the inversion of atmospheric aerosol extinction coefficient profiles using the absorption bands of O_4 is presented.

Prior to the inversion of aerosol extinction coefficient profiles, the optical properties of aerosols within the Ohio Valley were estimated. As a first step, the vertical distribution of aerosols in the study area was modeled using the EPA regulatory model AERMOD, a sophisticated Gaussian plume model which accounts for both local meteorology and the effects of elevated terrain. AERMOD is composed of three distinct components, named AERMET, AERMAP, and AERMOD. AERMET is a meteorological data processor which accepts as input hourly surface and twice daily

upper air soundings from the National Weather Service and conditions these data for input into the AERMOD programming structure and calculates boundary layer stability conditions¹⁰⁰. Surface observation data were obtained from the National Weather Service Station located at the Wheeling/Ohio County Airport, ID 469482. Upper air soundings were obtained from the National Weather Service Station KPIT, located at the Greater Pittsburgh International Airport. The AERMAP module is a terrain processor that characterizes the terrain for elevation and surface roughness and generates a grid of receptors that serve as virtual sampling sites in the AERMOD model. AERMAP uses Digital Elevation Maps (DEM) from the United States Geological Survey. These maps were downloaded from the USGS National Map Seamless server, and encompass a 30 by 30 km region centered on the coordinates of the sampling location, Latitude 39.92°, Longitude -80.76°. The AERMOD module corrects for any differences in the coordinate systems used in the DEM files. The receptor grid for aerosol modeling applications used in this research was defined on a polar grid centered on the sampling location and extending for 640 points on the map grid. A horizontal spacing of 1000 m was used between each ring of the sampling grid to a distance of 20 km. At each grid point, flagpole receptors were defined from the surface to 3 km, spaced every 100 m to 750 meters, 250 meters to 1 km, and every 1000 m to 3km. Within the AERMOD module itself, the source or sources are specified by emission type, location on the map grid, stack height, exit velocity, and exit gas temperature. All relevant statistics for the three sources impacting the area of study were obtained from the Ohio Environmental Protection Agency Emissions Inventory and the West Virginia Department of Environmental Protection Emissions Inventory for 2008. Locations of the sources were

acquired from digital raster images downloaded from the USGS National Map Seamless Server. For each study period modeled within AERMOD, the aerosol vertical profile, given as $\mu\text{g m}^{-3}$ was collected as a 24 hour average from the flagpole receptors 10 km distant from the sampling location and in the direction of the prevailing winds for that period.

The vertical profiles modeled with AERMOD account only for those $\text{PM}_{2.5}$ aerosols directly emitted from the sources in question. Additionally, the inversion algorithm used in this research assumed that the aerosol distribution was horizontally homogeneous and not concentrated within the emission plumes. Thus, as stated above, the profile was constructed from receptors 10 km distant from the center of the modeling domain, to simulate as closely as possible the more regional distribution of aerosols as opposed to those aerosols freshly emitted from a point source. The assumption that the aerosols are not concentrated in the plumes is supported by typical aerosol concentration values initially modeled within AERMOD, ranging from 0.001 to $3.65 \mu\text{g m}^{-3}$. It is fully acknowledged that some degree of error has been introduced to the inversion based on this assumption, as a very few modeled periods exceeded $100 \mu\text{g m}^{-3}$. Additional information on the validity of this assumption is given in Section 7.5. As such, the profiles are not a completely accurate description of the true aerosol distribution, lacking consideration for aerosol chemistries and formation. Thus, the concentration values were not directly used, instead only the shape of the vertical profile was used in this research, scaled to match previously published data on the optical properties of aerosols in this region. To overcome the lack of modeled aerosol concentration data, the optical properties of aerosols in the Ohio River Valley were simulated within the software

package OPAC (Optical Properties of Aerosols and Clouds)¹⁰¹ using the aerosol composition data collected at The Ohio University Air Quality Center in Athens, Ohio in 2004 and 2005 by M. Kim and others¹⁰². Within OPAC, the particle number density was varied until the peak aerosol extinction coefficient was 0.30 km^{-1} at 350 nm, based on seasonal haze measurements in the Eastern United States¹⁰³. Subsequent points from the modeled vertical distribution were scaled in like manner. For altitudes above 3 km, extinction coefficients were derived in like manner from the U.S. Standard Atmosphere, 1976¹⁷. This profile of aerosol extinction coefficient was taken as the a-priori profile in the Bayesian inversion scheme, as described in Chapter 6. The a-priori variance of the profile was set as 0.32, based on the standard deviation of previous measurements of aerosol concentration in the Ohio Valley by R.L.N. Yatavelli and others⁹⁸. The aerosol extinction coefficient profile is shown in Figure 7.2.

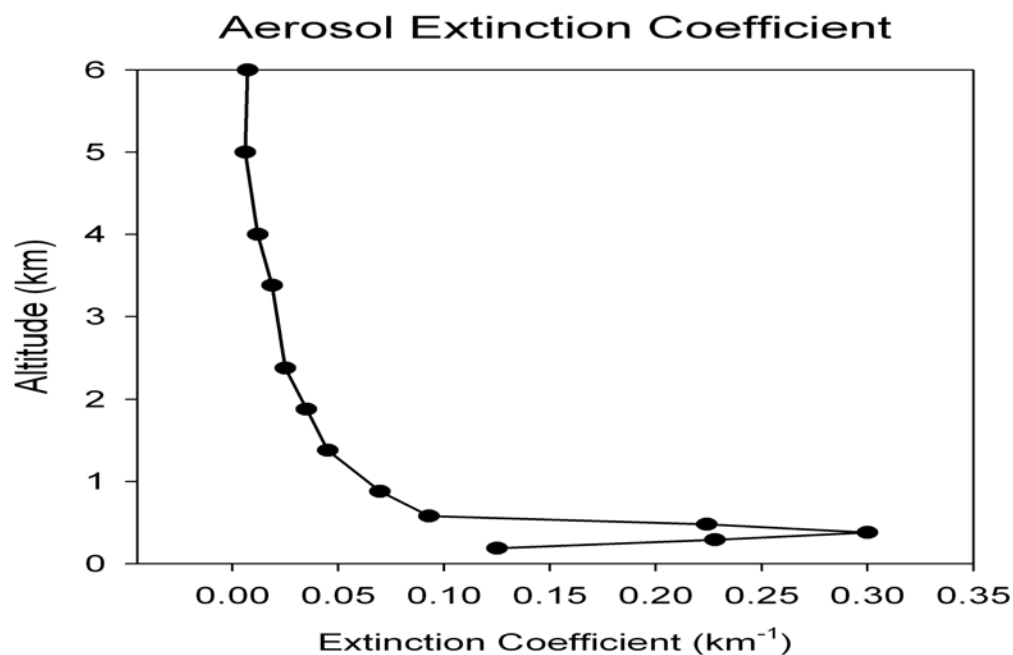


Figure 7.2: Aerosol extinction coefficient profile as derived from Gaussian plume model AERMOD and scaled to previously measured optical properties of aerosols in the Ohio River Valley.

In addition to the aerosol extinction coefficient, OPAC generates, based on composition, other optical properties of atmospheric aerosols necessary for the forward model SCIATRAN used in this inversion. In this case, the Henyey-Greenstein asymmetry factor and phase function were also calculated. For the aerosol composition used in this research, the asymmetry factor was calculated to be 0.756. It was assumed that this value was uniform from the surface to the maximum altitude used in the inversion routine, 10 km.

7.3 DOAS Analysis of O₄

The inversion methodology described in Section 6.4 was adapted for the inversion of aerosol profiles using the O₄ absorption signal. For inversion of trace gas species, the weighting function matrix for each species represents the change in optical depth due to a change in concentration of that species. This is true also for the weighting functions of aerosol extinction coefficients calculated by the forward model SCIATRAN, excepting that the weighting function will represent the change in all absorptions due to a change in aerosol extinction. Thus, the forward model must be limited to only the O₄ absorption, so that the weighting function matrix is limited to representing only the change in O₄ absorption due to a change in aerosol extinction, and not the change of absorption by additional species. As such, the measured data y in the inversion scheme must be only the differential absorption of the O₄ species. These data were generated by performing the differential analysis detailed in Chapter 5. Details of the DOAS regression performed for O₄ are described here.

The fitting window chosen for this analysis was 336 to 368 nm, which contains two O₄ absorption bands. In addition to the O₄ absorption cross-section⁴⁶, cross-sections of NO₂³⁸, O₃⁴⁵, HCHO⁴¹, Glyoxal¹⁰⁴, and BrO¹⁰⁵ were included in the regression. Also included in the regression was a 2nd order polynomial and a synthetic Ring spectrum calculated from a high resolution solar spectrum⁸². In all cases, the zenith line of sight spectrum for angle collection series was used as the reference intensity. All fitting operations were done using the DOAS analysis software WinDOAS⁷³. The root mean square (RMS) value of the residuals for each line of sight serves as the noise-covariance

matrix in the inversion scheme described in Chapter 6. This value was typically 2×10^{-3} or less for all lines of sight.

7.4 Inversion of Aerosol Extinction Coefficient Profiles

Aerosol extinction coefficient profiles were inverted using the Matlab inversion routine as described in Chapter 6, using the aerosol extinction coefficient profile described in Section 7.2 as the a-priori profile with a variance of 0.32. Weighting function matrices of aerosol extinction coefficients were generated using the forward model SCIATRAN. The inversion was performed for the data measured during September 2008, the most cloud-free collection period. Each profile was inverted from spectra collected at elevation angles 2.5° , 5° , 7° , 10° , and 15° degrees, using the zenith line of sight as the reference intensity. As the problem is a non-linear one, multiple iterations were required to reach convergence, defined here as a change in the scalar cost function (equation 6.16) less than or equal to 5%. Convergence was typically achieved in two or three iterations. The results of the inversions for the September collection period are shown in Figures 7.3 to 7.5. Each series represents a two-hour time step for each day of collection.

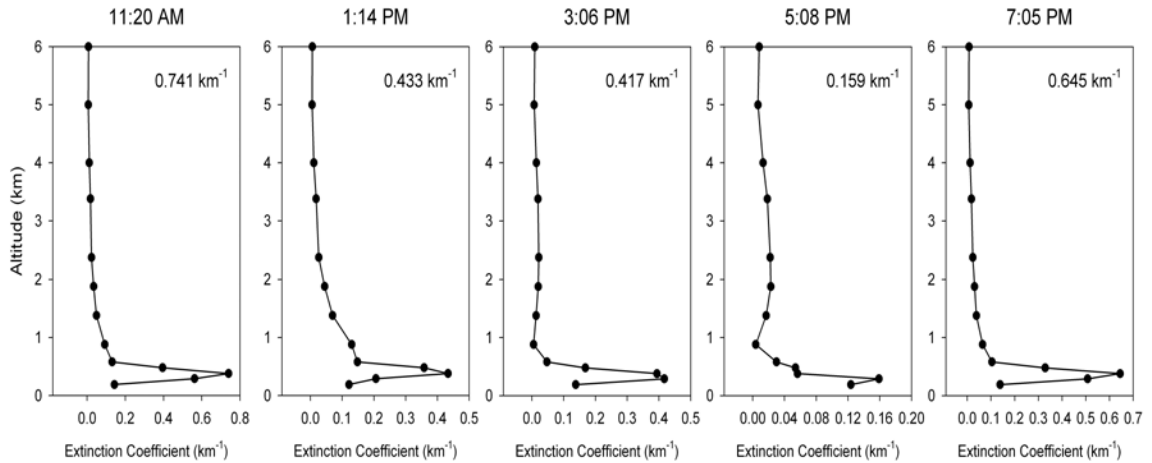


Figure 7.3: Aerosol extinction coefficient profiles for September 17, 2008. The peak value of each profile is shown in the upper right corner of each trace. The profiles are inverted from O_4 absorption spectra collected at viewing angles 2.5° , 5° , 7° , 10° , and 15° .

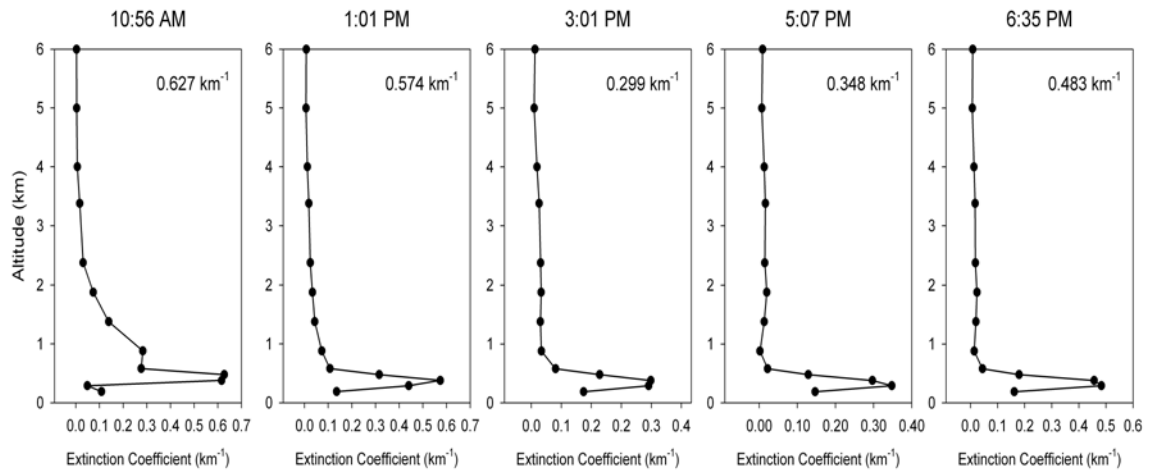


Figure 7.4: Aerosol extinction coefficient profiles for September 18, 2008. The peak value of each profile is shown in the upper right corner of each trace. The profiles are inverted from O_4 absorption spectra collected at viewing angles 2.5° , 5° , 7° , 10° , and 15° .

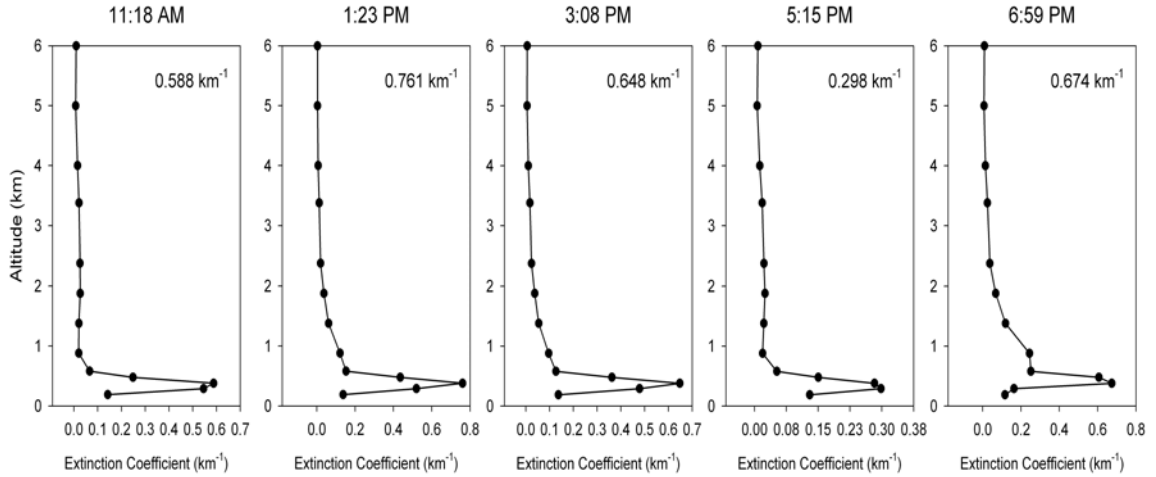


Figure 7.5: Aerosol extinction coefficient profiles for September 19, 2008. The peak value of each profile is shown in the upper right corner of each trace. The profiles are inverted from O_4 absorption spectra collected at viewing angles 2.5° , 5° , 7° , 10° , and 15° .

The optimal estimation method used for the inversion of the aerosol extinction profiles attempts to retrieve the best possible solution (profile) from an infinite set of possible solutions. Constraints, represented by the noise and measurement covariance matrices, allow this solution to be determined. Inversion of this type can be characterized by the averaging kernel, A . The averaging kernel represents the sensitivity of the retrieved state to the true state. Averaging kernels are calculated by^{3,4,91}:

$$A = \left(K^T S_\epsilon^{-1} K + S_a^{-1} \right)^{-1} K^T S_\epsilon^{-1} K. \quad (7.1)$$

The rows of A are the averaging kernels, and at each point describe how the true atmospheric state is smoothed by the retrieval. Under ideal circumstances, the averaging kernel would be an identity matrix, although such circumstances are rarely encountered in remote sensing. Typical averaging kernels for the inversion of aerosol extinction

coefficients at 350 nm taken from the inversion of data collected on September 17, 2008 at 1:14 PM are shown in Figure 7.6.

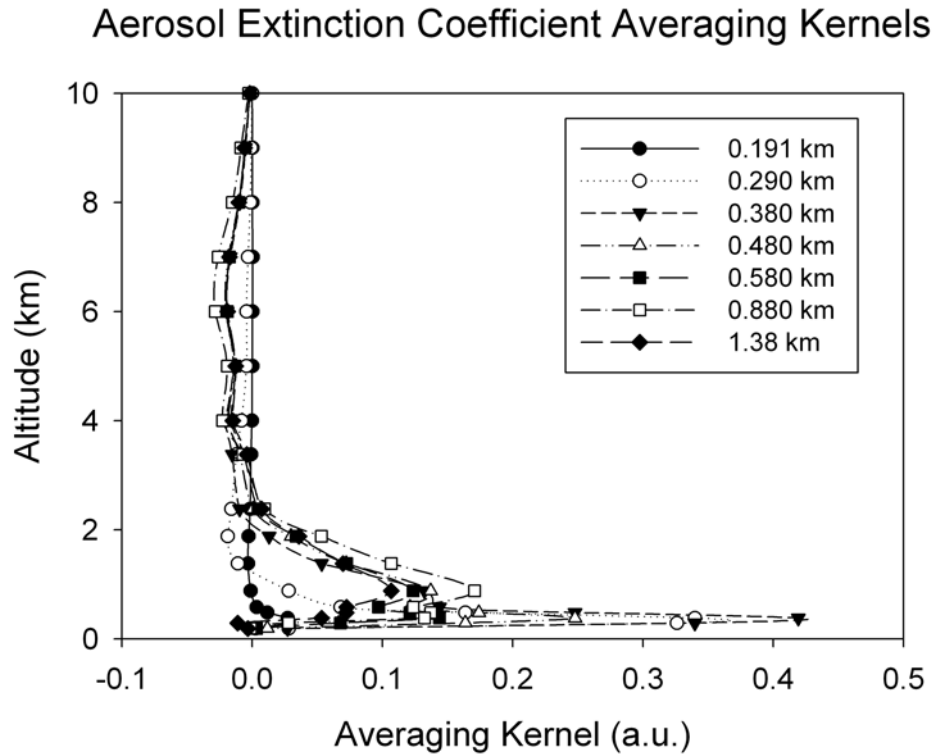


Figure 7.6: Averaging kernels for the first seven altitudes used in inversion of aerosol extinction coefficients for September 17, 2008, at 1:14 PM.

Several important pieces of information can be gathered from examination of the averaging kernels^{3,4,91}. Firstly, it is apparent that the majority of sensitivity is found below 2 km, with the bulk of the information in the measurements coming from the lowest 500 meters. Secondly, the width of each averaging kernel (i.e. FWHM) serves as an indicator of the resolution of the measurement. To approximately 0.480 km, the

vertical resolution was estimated to be 200 m. Above 0.480 km, the vertical resolution of the measurements is much less, approximately 1.2 km. Lastly, as stated above, ideal averaging kernels would have a value of 1. Peak averaging kernel values in the inversion presented here have a typical value of 0.4, indicating that a significant portion of the information in the retrieval is derived from the a-priori profile and not the measurements themselves. This is largely a product of the deficit of information on the vertical distribution of aerosol profiles in the Ohio River Valley and the highly variable nature of the available aerosol measurement data sets. In these inversions, this uncertainty was reflected in the relatively large a-priori covariance, 0.32. The weak constraint on the profiles indicates the uncertainty in the a-priori profile, resulting in the interpretation of spectral noise as data⁴. The constraint on the aerosol profiles, and thus the averaging kernels, could be improved through both vertical profile soundings in this region and more extensive chemical/physical modeling beyond the capabilities of AERMOD.

Despite the shortcomings of the a-priori profile and its covariance, the retrieved profiles of aerosol extinction yielded excellent agreement with measured O₄ absorption spectra. The average root mean squares of the residuals were 1.1×10^{-3} , 1.1×10^{-3} , and 1.6×10^{-3} , for September 17, 18, and 19, respectively. These can be compared to typical O₄ differential optical depths of 4×10^{-3} to 6×10^{-3} . Figure 7.7 shows the measured and modeled O₄ differential absorption spectra for the 7° line of sight of September 17, 2008 at 1:14 PM.

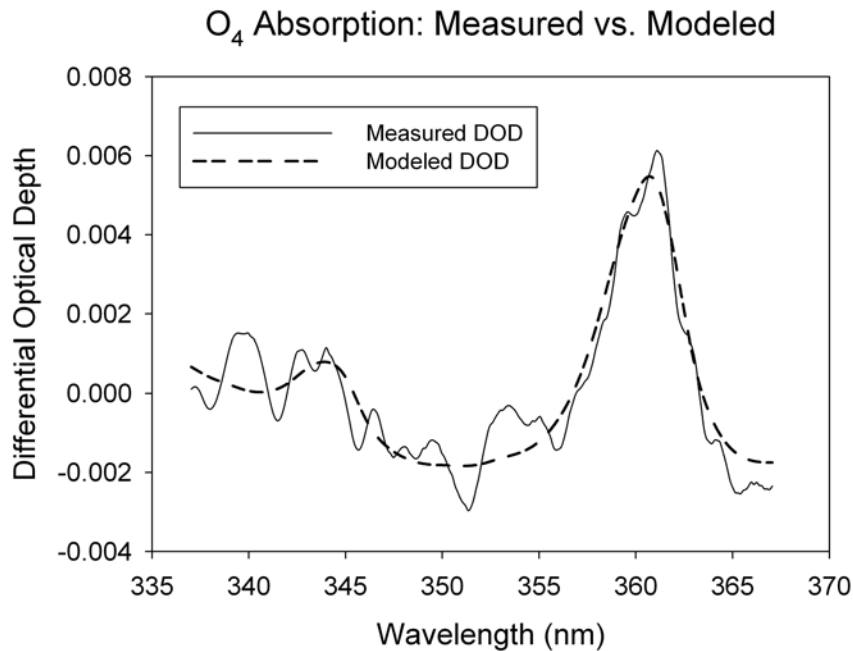


Figure 7.7: Measured and modeled O₄ differential optical depth spectra. The modeled data is a result of a forward model (F(x)) run using the retrieved profile of aerosol extinction at 350 nm for September 17, 2008 at 1:14 PM.

As the secondary purpose of the aerosol inversion was to define a vertical profile of aerosol extinction to improve the accuracy of subsequent radiative transfer modeling, for example, the calculation of air mass factors for trace gas species, the close agreement between the measured and modeled data indicates that the effects of mis-specification of the aerosol profile on the radiative transfer modeling of other atmospheric species have been minimized. That is, any spurious spectral data of other gas species have been assumed to arise from the spectral analysis or the quality of the measured data itself and not from the incorrect specification of aerosol extinction properties in the radiative transfer model. To this end, all other radiative transfer modeling in this work used the

average extinction coefficient profile from the entire September 2008 collection period. This data is shown in Figure 7.8.

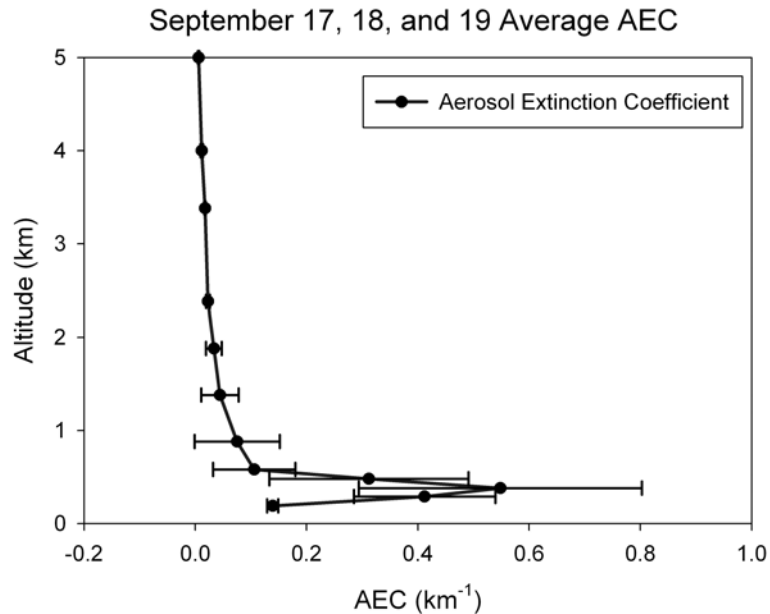


Figure 7.8: Average aerosol extinction coefficient profile for the entire September 2008 collection period. Error bars represent the standard deviation of the data set. The aerosol profile shown here was used for all subsequent radiative transfer applications in this research

7.5 Conclusions, Aerosol Extinction Coefficient Inversion

Optical properties of aerosols were calculated from previous measurements of the composition of aerosols in the Ohio River Valley using the software package OPAC and used to scale a modeled vertical distribution of aerosols in this region generated using the EPA regulatory model AERMOD. Using this profile as the a-priori in the Bayesian inversion scheme described in Chapter 6 implemented in a Matlab program coupled to the radiative transfer model SCIATRAN, vertical profiles of the aerosol extinction

coefficient at 350 nm for the September 2008 collection period were retrieved using measured differential optical depth spectra of the O₄ species. The O₄ species is a collisional dimer of O₂ and therefore its distribution is well known. Thus, this species serves as an atmospheric constant whose absorption signal is primarily a function of scattering and the optical properties of the atmosphere. The retrieved aerosol profiles show remarkable agreement with the measured spectral data, but, due to the lack of information available on the distribution of aerosols in this region, are strongly dependent on the a-priori values. The weakly constrained problem leads to the interpretation of spectral noise as data. An average aerosol extinction coefficient profile for the September 2008 collection period was calculated from all retrieved profiles in the data set, with a peak aerosol extinction coefficient of 0.549 km⁻¹. This profile was implemented in all other radiative transfer applications in this research.

During the daylight hours of the September 2008 study period, peak aerosol extinction coefficient values show a distinct trend of decreasing values from the morning measurements to a late afternoon minimum, followed by an increase near sunset. Although there is some difficulty in correlating data collected with remote sensing measurements with bulk atmospheric properties, the daily trend in aerosol extinctions can in this case be understood by examination of the time series of relative humidity. Outside of aerosol composition, relative humidity is major factor in controlling the aerosol extinction values. Figure 7.9 shows the peak aerosol extinction coefficient values for the September 2008 sampling period, plotted with relative humidity, collected from the National Weather Service monitoring station located at the Wheeling/Ohio County Airport, ID 469482.

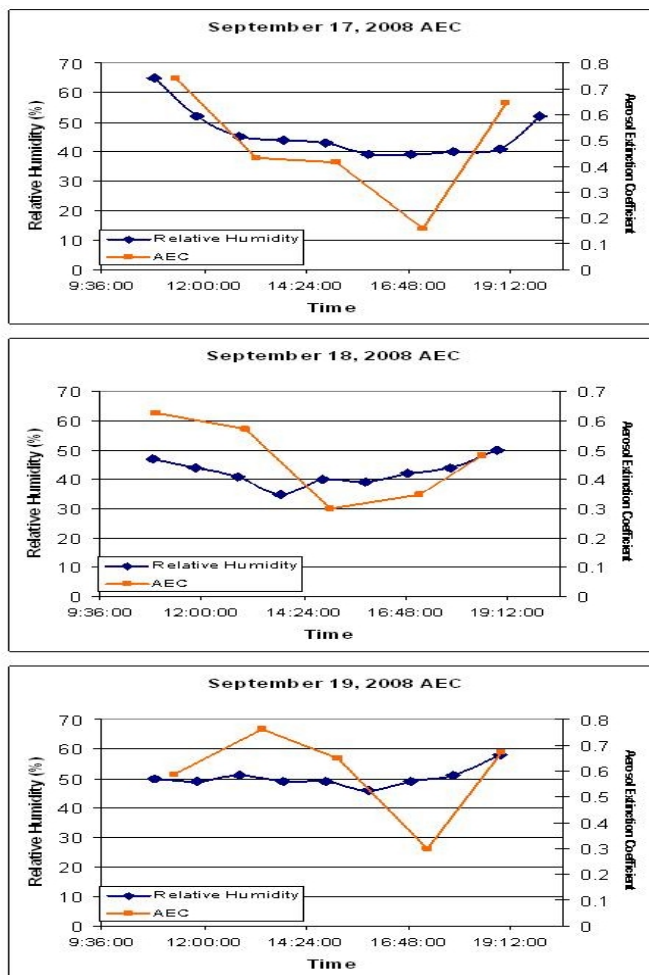


Figure 7.9: Aerosol extinction coefficient (km^{-1}) plotted with relative humidity values.

The correlation between aerosol extinction coefficient and relative humidity is apparent in the traces shown in Figure 7.9. Inorganic aerosols, the dominant species of aerosol in the Ohio River Valley⁹⁸, are primarily hygroscopic in nature. Uptake of atmospheric water vapor by hygroscopic particulate matter increases the diameter of the aerosol, and therefore the extinction coefficient of that particular aerosol species. A relative humidity increase from 50% to 90% can lead to an enhancement in aerosol extinction coefficients by as much as 250%¹⁰⁶.

The correlation between aerosol extinction coefficient and relative humidity lend support to the assumption that the treatment of aerosols as a horizontally homogeneous species, as opposed to an anomaly in the atmospheric distribution, for the purposes of inversion. Gillani and Wilson defined a three-stage process in the formation of aerosols within plumes, the earliest stage of which representing a young plume approximately 1 hr in age. This earliest stage is characterized primarily by lack of interaction of the plume with the background atmosphere, based on observations of O_3 and aerosol formation¹⁰⁷. This earliest stage is characterized primarily by a deficit of O_3 due to reaction with NO , by R7.1¹⁰⁷:



As described in Chapter 2, the photo-stationary cycle of O_3 concentration can be broken by addition of other molecules to the NO_x/O_3 system, allowing additional O_3 production pathways to occur. It is expected that the plume examined here can be characterized by this early stage, based on the estimated downwind distance where the line of sight of the DOAS instrument transects the plume, approximately 900 m. A deficit in O_3 relative to the background was also observed as negative slant column densities of O_3 throughout the entire measurement period. As stated previously, the lack of interaction between the plume and the ambient air would inhibit the relative humidity mediated growth of aerosols in this stage of plume development. Thus, were the plume the primary contributor to the O_4 absorption signal (and thus aerosols), it is likely the correlation to relative humidity would not be observed. It can therefore be concluded that the average aerosol extinction coefficient profile shown in Figure 7.8 represents the regional distribution of aerosol extinction at 350 nm in the Ohio River Valley, and that

the plume, while a source of particulate matter, is not dominant above background aerosols given the relatively young age, dependence on the retrieved values on ambient relative humidity, and observation of an O₃ deficit within the plume suggesting minimal interaction between the plume and the ambient atmosphere.

7.6 DOAS Analysis of SO₂, NO₂, and HCHO

In addition to the O₄ species, the collected scattered solar radiation spectra were analyzed to determine the slant column densities of SO₂, NO₂, and HCHO. For each species, as with the O₄ analysis, the zenith line of sight spectra from each angular collection series was used as the reference intensity. A description of the fitting operations used to calculate the slant column densities and implemented in the DOAS analysis software WindDOAS for each of these three species is presented here.

7.6a SO₂ Fitting Window

The SO₂ fitting window used in this research was 303 to 324 nm. To each differential optical depth spectra, the differential absorption cross-sections of SO₂¹⁰⁸, NO₂³⁸, BrO¹⁰⁵, O₃⁴⁵, and a synthetic Ring correction spectra were fitted⁸². All parameters were subjected to a shift and stretch algorithm, as described in Chapter 5, to correct for wavelength misalignments between the reference cross-sections and the DOAS spectrometer. In addition to the absorption cross-sections above, a 2nd order polynomial was included in the regression to account for broad-band extinction processes. An example of the SO₂ regression, showing the fitted SO₂ absorption and the measured SO₂ differential optical depth is shown in Figure 7.10.

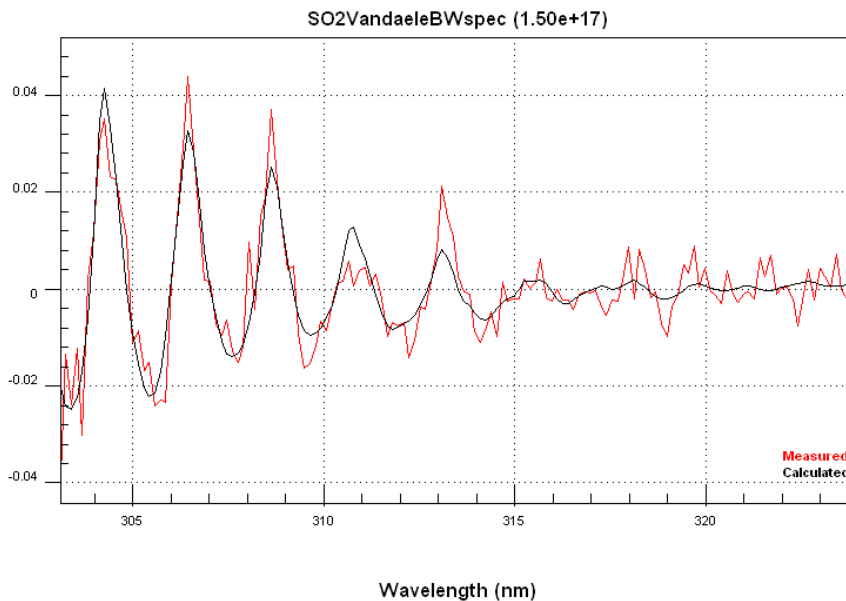


Figure 7.10: Example of the analysis of SO₂ from the WinDOAS analysis software from the July 16, 2008 collection period.

7.6b NO₂ Fitting Window

The wavelength window used for the analysis of NO₂ was 399 to 420 nm. In this window, the absorption cross-sections of NO₂³⁸, O₃⁴⁵, O₄⁴⁶, and a Ring correction spectrum⁸² were fitted to the differential optical depth. A polynomial of 3rd order was also included in each regression. Again, the zenith line of sight spectrum for each angular measurement series was used as the reference intensity. All cross-sections were subjected to a non-linear shift and stretch algorithm to correct for any wavelength misalignments between the absorption cross-sections and the DOAS spectrometer.

7.6c HCHO Fitting Window

The fitting window for HCHO was 311 to 347 nm. In this wavelength window, the absorption cross-sections of HCHO, NO₂³⁸, O₃⁴⁵, and O₄⁴⁶, as well as a Ring

correction spectrum⁸² were included in each regression analysis. Broad-band features were accounted for using a 4th order polynomial, and the zenith sky spectrum for each angular measurement series was used as the reference intensity. All cross-sections were subjected to a non-linear shift and stretch algorithm to correct any wavelength misalignments.

7.7 Gaussian Plume Modeling of NO₂ and SO₂

As with the O₄ species, proper interpretation of the results of the DOAS spectral analysis for SO₂ and NO₂ required vertical profiles of these species representative of the atmospheric condition. Due to the horizontally inhomogeneous distribution of these species close to the point source (Power Plant #1), a true optimal inversion, as was conducted for the aerosol extinction coefficients, was not possible. Thus, alternative methods to estimate the concentration of these species from the spectral data were applied. The concept of the air mass factor, as introduced in Chapter 6, was used. This being the case, it is not necessary to determine the absolute concentrations of the species to be analyzed prior to radiative transfer modeling, only the relative shape of the vertical profile, as air mass factors are independent of the absolute concentration⁹⁰. Regardless of this stipulation, AERMOD simulations of the entire measurement period were conducted with the same eye to accuracy used in the modeling of aerosol profiles. A modified polar grid of 24 angles radiating from Power Plant # 1, located at 50 m distant, then every 100 m to a final distance of 900 m was used. At each of these 240 receptor points, ten flagpole receptors, from 100 m to 1000m altitude were also included. As with the aerosol simulation, emissions were specified in the AERMOD using the Emissions Inventory of the Ohio Environmental Protection Agency and the West Virginia Department of

Environmental Protection for the three coal-fired power plants simulated. The profiles of NO₂ and SO₂ were assembled from the highest 3-hour averages of each species at the receptor radius of 900m, within 45° of the prevailing winds, for the month of July 2008. Additionally, background profiles of each species were selected from the highest 3-hour averages of each species at the receptor location nearest sampling site 1, well outside of the prevailing winds and influence of the plume emissions. Above 1000m, the modeled concentrations were merged with concentration data from the U.S. 1976 Standard Atmosphere¹⁷. The vertical profiles of NO₂ and SO₂ representing the emission plume are shown in Figure 7.11.

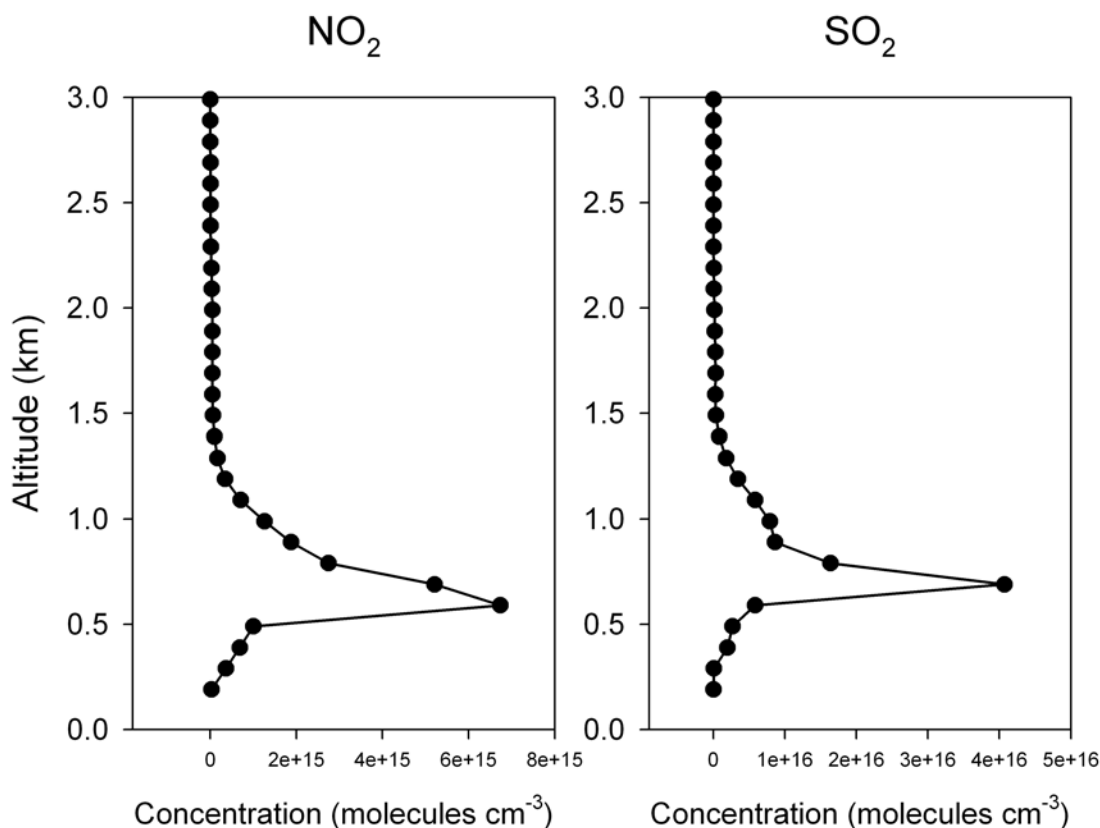


Figure 7.11: NO₂ and SO₂ profiles generated from the EPA Gaussian Plume model AERMOD and compiled from the highest 3-hour averages for the month of July, 2008.

7.8 Radiative Transfer Modeling of NO₂ and SO₂ Air Mass Factors

The horizontal in-homogeneities of NO₂ and SO₂ necessitate the use of a radiative transfer model in which such profiles can be specified. For this research, the radiative transfer model MCARaTS was used to calculate air mass factors for the conversion of SO₂ and NO₂ slant column densities to vertical column densities, and subsequently concentrations. Within MCARaTS, horizontally homogeneous parameters are specified as simple vertical profiles. Within each pixel of the three dimensional grid, these parameters are equal in the x and y directions. Horizontal in-homogeneities of

atmospheric properties are specified as perturbations to the homogenous profiles within specific pixels. In addition to the amount of perturbation, the location in the three dimensional Cartesian grid must also be specified. In the z direction, this is a simple matter, but specification in the x and y directions require an estimate of the plume size. From the AERMOD modeled profiles, the plume width was estimated to be 235 m in diameter, and this value was used to specify the location of the plumes within the Cartesian grid. The cross-sectional view of the NO₂ plume, as specified in MCARaTS, is shown in Figure 7.12. The length of the plume was assumed to span the entire length of the modeling domain.

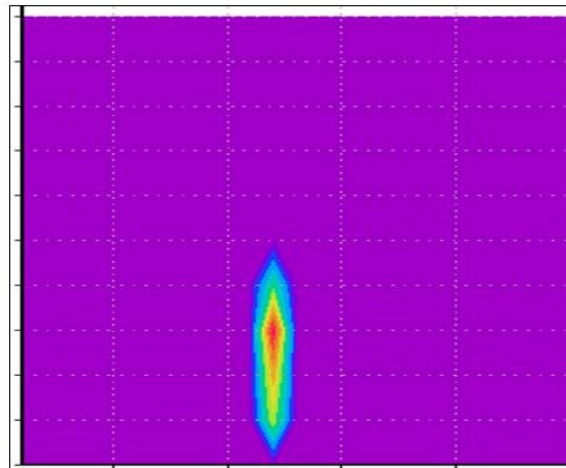


Figure 7.12: Cross-sectional view of the NO₂ plume as specified in the three-dimensional grid of the MCARaTS radiative transfer model as a perturbation to the horizontally homogeneous atmosphere.

Air mass factors for NO₂ and SO₂ were simulated for each measurement collected during the nine-day study. Each measurement is specified in the model as a solar

azimuth, solar zenith, and instrument observation angle. For each measurement, 1×10^9 photons were simulated, at 413.45 and 304 nm, for NO_2 and SO_2 , respectively. Air mass factors within MCARaTS are calculated as the layer average pathlength normalized by the vertical size of each layer.

A 2009 paper on the radiative transfer in volcanic plumes and the application to passive DOAS systems introduced the novel concept of a plume air mass factor, abbreviated here as PAMF¹¹. Traditional AMFS, described by equation 6.3:

$$AMF = \frac{SCD}{VCD} \quad (6.3)$$

are calculated as the ratio of the slant column density to the vertical column density, and the respective *VCD* for any measured *SCD* is calculated by division of the *SCD* by the respective air mass factor. Analogous to this concept are the AMFs calculated by MCARaTS, which represent the pathlength of scattered radiation in the atmosphere divided by the vertical height of a particular layer. The PAMF concept extends the air mass factor by calculating the ratio of the measured slant column density to the slant column along a straight line through the plume, as opposed to the vertical direction. Again, this concept can be extended to the AMFs calculated by MCARaTS, using the pathlength of the scattered radiation and the straight path through the plume calculated from the measurement geometry at each line of sight. This relationship is expressed by equation 7.3 as:

$$PAMF = \frac{LightPath_{measured}}{LightPath_{geometric}} \quad (7.3)$$

Plume air mass factors were calculated using equation 7.3, geometric path lengths for each line of sight for the measurement period, and the total vertical height of the

modeling domain within MCAraTS, as well as the modeled air mass factors described above. These plume air mass factors were used to convert the measured slant column densities of NO₂ and SO₂. It should be noted that the differential form of the air mass factors, analogous to the differential slant column densities resulting from the regression analysis of DOAS data were used for this conversion. These differential air mass factors were calculated by subtracting the air mass factor of the zenith line of sight for each measurement series from the air mass factors calculated for the off-axis elevation angles.

7.9 Plume Mixing Ratios, NO₂ and SO₂

As detailed above, plume air mass factors calculated from the radiative transfer model MCAraTS were used to convert measured NO₂ and SO₂ slant column densities to their geometric pathlength analog of vertical column densities, in units of molecules cm⁻². Using the estimated size of the plume, 235 m, the vertical column densities of NO₂ and SO₂ were converted to concentration, and subsequently mixing ratios. A temperature of 298 K was assumed in the conversion of concentration to mixing ratio (ppb). The time series of peak mixing ratios, assumed to correspond with center of the emission plume, are shown in Figure 7.13 and 7.14 for NO₂ and SO₂, respectively.

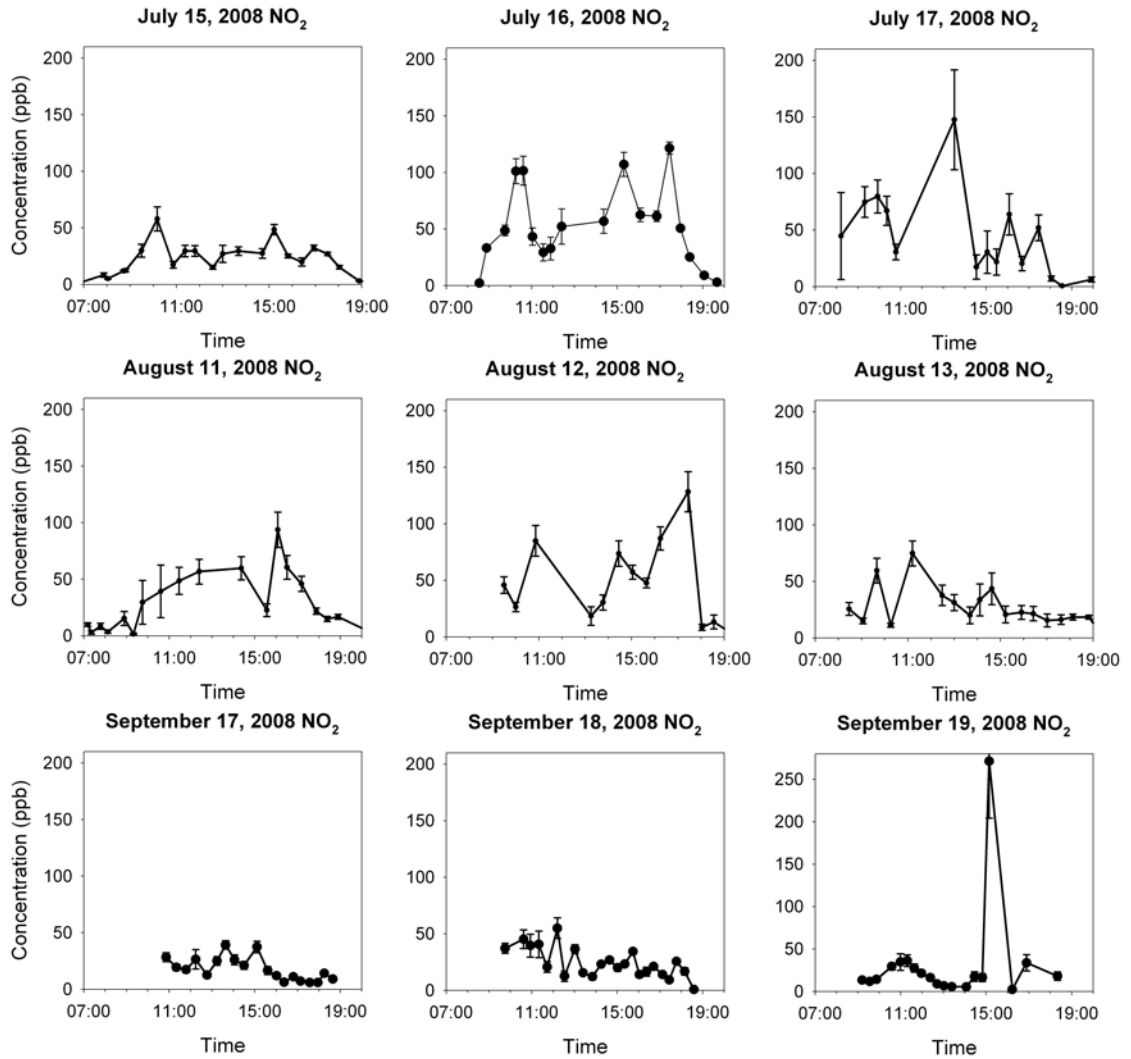


Figure 7.13: Peak mixing ratios of NO₂ determined from measured slant column densities. Error bars indicate the Root Mean Squared Error of the regression.

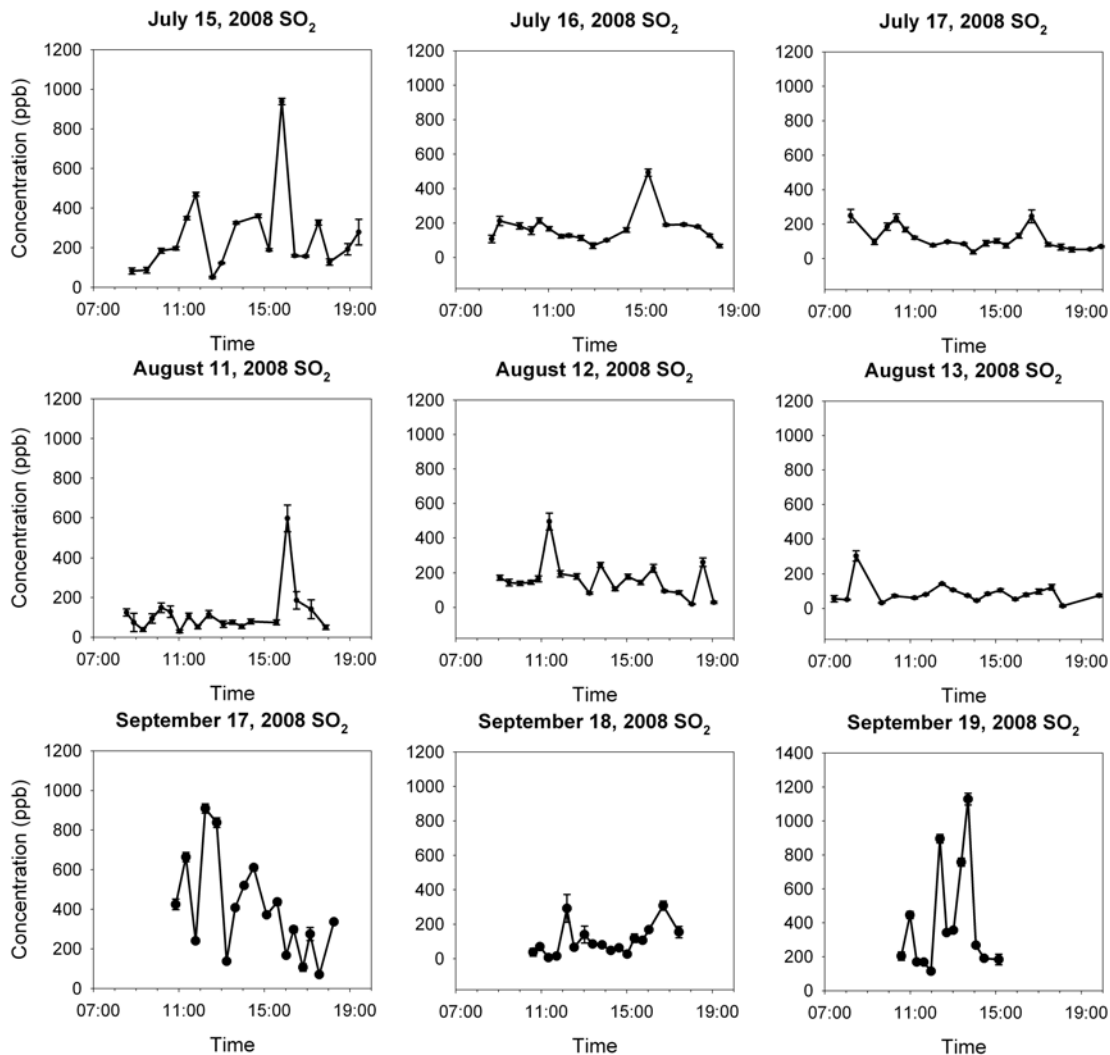


Figure 7.14: Peak mixing ratios of SO₂ determined from measured slant column densities. Error bars indicate the Root Mean Squared error of the regression.

Although in-plume measurements of power plant plumes are not readily available as a source of outside confirmation of remotely sensed data, estimations of flux can be compared to available emissions inventories. Using the average plume concentration for the measurement period, 192.31 ± 190 ppb of SO₂, and the average wind speed for the measurement period, 4.7 ± 3.9 mph, the annual flux of SO₂ from Power Plant #1, closest

to the sampling locations, was calculated. The size of the plume was estimated based on the plume width, 235 m, and the approximate sampling distance downwind of the source, 900 m. Using a sampling time of 25 minutes, the annual flux of SO₂ was estimated to be 1551 tons year⁻¹. This is significantly different from the stated annual emissions of Power Plant #1, approximate 14,000 tons year⁻¹, from the 2008 Ohio EPA Emissions Inventory. However, extrapolation of a full year of emissions from nine days of data unquestionably introduces error, and, given the highly variable nature of both the wind speed and concentrations within the plume, the estimate seems less poor. Only for an extended period of monitoring could the variations in the type of coal being burnt and proprietary information on the combustion rates from a particular source, as well as variations in wind speed, be accounted for in a flux estimation. Application of the same assumptions for NO₂ yielded a flux of 71.2 tons year⁻¹, although this measurement cannot be compared directly to emissions data, which report only NO_x. Despite the significant discrepancies in the estimate of annual flux from the nine-day measurement period shown here, the average concentration of SO₂ for the collection period, 192.31 ± 190 ppb, is very similar to the highest average value of SO₂ for the entire measurement period, 208 ppb, obtained from AERMOD simulations. Although not as reliable as secondary measurements within the plume itself, the agreement between these values is exceptional given the only hourly time resolution of the AERMOD model and the limited angular resolution of the MAX-DOAS instrument itself, and provides a measure of validation for the methodology developed in this work.

Application of MAX-DOAS techniques to the monitoring of anthropogenic emissions plumes is under-represented in the scientific literature. At the time of writing

this document, a single example was available. In that research, scans were made perpendicular to a plume to monitor the concentration of ClO, SO₂, and NO₂⁶. Based on geometric analysis, the size of the plume was estimated, and the concentration calculated by dividing the measured slant column densities by this plume size. Realistic values of all three species were obtained. However, that study, published prior to the introduction of the plume air mass factor, as proposed by Kern¹¹ and applied in this research, neglects the effects of radiative transfer in the horizontally in-homogeneous plume. It was found in this work that failure to consider the effects of radiative transfer in estimating the concentration of SO₂ and NO₂ can result in concentration values, on average, 85% higher than those methods accounting for radiative transfer, and under-estimations of NO₂ concentration by an average of 5.9%. These results are not surprising, based on the approximate order of magnitude difference in scattering efficiencies for wavelengths 413 and 305 nm, using the relationship $1/\lambda^4$. It is therefore crucial in the monitoring of SO₂ plumes to account for the effects of radiative transfer.

7.10 Formaldehyde

Spectral data collected during the measurement period demonstrated strong, clear absorptions attributed to the atmospheric species formaldehyde, HCHO. However, only slant columns from the July 15, 2008 data set had acceptable levels of error in the regression results. HCHO itself is not considered to be a product of coal combustion, and is typically associated with the combustion of petroleum¹⁰⁹. The slant column densities of HCHO also did not show the clear plume structure (enhancement at lines of sight pointing within the plume) demonstrated by both SO₂ and NO₂. Therefore, it was assumed that the observed HCHO was not present in the plume, but rather distributed

throughout the atmosphere, as was the case for aerosols in this research. As such, the radiative transfer model SCIATRAN was used to simulate the air mass factors of HCHO for the July 15, 2008 collection period, using vertical profiles from the MPI Mainz climatology database⁹². These air mass factors (differential) were subsequently used to calculate the vertical column densities of HCHO.

From this analysis, vertical column densities of HCHO were determined from the 2.5, 5, and 7 lines of sight. Although little information can be garnered from a single day of measurement, indeed, there is a considerable deficit in the literature on the global distribution of HCHO in general, the average vertical column of HCHO measured from the July 15th, 2008 was 2.3×10^{16} molecules cm^{-2} . Within the available literature, only a single point of comparison, based on the simulation of HCHO columns in North America using the three-dimensional model GEOS-Chem. The results of this simulation predict a vertical HCHO column of approximately 1.5×10^{16} molecules cm^{-2} ¹¹⁰:

The modeled column of HCHO over the Upper Ohio River Valley, approximately 1.5×10^{16} molecules cm^{-2} , is comparable to the average measured value from July 15, 2008 over the same region. Given the deficit in available data, this comparison serves only to confirm that the chosen analysis method, that is, simulating the air mass factors of HCHO treating the species as horizontally homogeneous and the wavelength region chosen for the analysis of HCHO are adequate. Further investigation and measurement would be required to draw any further conclusions on the distribution of HCHO over this region. However, the assumed horizontally homogeneous nature of HCHO in this region would lend itself to the Bayesian inversion techniques presented previously for the extinction coefficient of aerosols, should a suitable a-priori profile and spread statistics

become available in the future. Application of a photochemical model could produce similar data in the absence of vertical soundings of HCHO.

CHAPTER 8: SUMMARY AND CONCLUSIONS

8.1 Summary

In this research, it was hypothesized that the MAX-DOAS method could be applied to the monitoring of anthropogenic plumes, accounting fully for radiative transfer within the isolated plume, a methodology applied previously only in theory¹¹. Additionally, it was hypothesized that sophisticated Gaussian plume models could be used in both the interpretation of MAX-DOAS data collected by scanning vertically across the height of a plume and in the evaluation of that data for accuracy. To this end, a nine-day field study in the Upper Ohio River Valley near Wheeling, West Virginia was conducted, during which spectra of scattered solar radiation were collected at multiple elevation angles perpendicular to the plume of a coal-fired power plant. This data was subsequently analyzed to determine the absorption contributions of SO₂, NO₂, and O₄.

To ensure accurate radiative transfer simulations for the interpretation of MAX-DOAS data, the O₄ absorption signal was used in a maximum a-posteriori inversion methodology to retrieve the vertical distribution of aerosols over the region. Based on this inversion, an average profile of aerosol extinction coefficient at 350 nm was obtained. This profile had a peak extinction coefficient of 0.549 km⁻¹ at approximately 500 m above the ground. Additionally, the retrieved aerosol profiles demonstrated a degree of correlation to changing atmospheric conditions over the course of each day, in particular to relative humidity, a well-known controlling factor in the growth, and

therefore change, in aerosol extinction coefficients and optical properties¹⁵. To generate the a-priori aerosol profile used in the inversion, the EPA regulatory model AERMOD was used in conjunction with previous measurements of aerosol composition in the Ohio River Valley^{98,102} and a model of aerosol optical properties¹⁰¹. The averaged extinction coefficient profile obtained from the inversion was used in all subsequent radiative transfer modeling applications in this research.

The spectral data collected during the nine-day field study was also analyzed to determine the absorption contribution of NO₂ and SO₂, important atmospheric species released in large amounts by coal-fired power plants. Proper interpretation of plume data, previously based on the assumption that the light path through a plume was defined as a straight line, required the use of a model of radiative transfer capable of simulating the effects of an isolated plume within an otherwise horizontally homogeneous atmosphere. Accounting for radiative transfer within the plume itself was previously demonstrated only in theoretical calculations, in which the concept of the Plume Air Mass Factor, PAMF, was introduced¹¹. In this research, PAMFs were simulated using the radiative transfer model MCARaTS, a Monte Carlo radiative transfer program which defines the modeling domain as a three-dimensional grid of cells, within which the concentration of a species can be defined in each individual cell. To determine the size, shape, and altitude of the SO₂ and NO₂ emissions plumes, the EPA regulatory model AERMOD was again used to simulate the distribution of these two gases within a similar three-dimensional grid. The plumes generated by AERMOD were based on the emissions inventory of the facilities emitting pollutants in this region, provided by the Ohio Environmental Protection Agency and the West Virginia Department of Environmental Protection.

Additional meteorological data, also used as input to the model AERMOD, were gathered from the National Weather Service. The Plume Air Mass Factors simulated within MCARaTS were used to convert measured slant column densities of SO₂ and NO₂ to plume column densities. Based on geometric and AERMOD simulations, the size of the plume, 235 m, was used to convert the plume column densities to mixing ratios within the plume itself. Although a direct comparison of NO₂ would only be possible using a sophisticated chemical/physical dispersion model, the SO₂ mixing ratios within the plume can be readily compared to values obtained with the AERMOD simulation. In this case, the measured, average concentration over the nine day sampling period was determined to be 192.31 ± 190 ppb, and the highest average value of SO₂ was determined to be 208 ppb. As stated previously, while not a direct, secondary measurement of the plume concentration, the modeled results provide a measure of validation to the MAX-DOAS results. Accounting for the radiative transfer within the horizontally inhomogeneous atmosphere, in addition to giving results comparable to modeled data, can be compared to more traditional methods of concentration estimation within a plume; that is, ignoring the effects of radiative transfer. For the data set used in this research, failure to account for the effects of radiative transfer yielded SO₂ mixing ratios 85% higher than this method, accounting for radiative transfer, and under-estimations of NO₂ concentration by an average of 5.9%. This is not surprising, based on the increased scattering of photons at lower wavelengths.

In addition to SO₂ and NO₂, the absorption signal of HCHO, a product of atmospheric oxidation of gaseous hydrocarbons, was analyzed. The quality of the regression analysis for this species was quite poor and only limited information on the

species could be derived. In this case, the vertical column density of HCHO was determined to be 2.3×10^{16} molecules cm^{-2} , comparable to modeled results over the Ohio River Valley¹¹⁰. Despite the deficit of usable data on HCHO gathered from this field study, these preliminary results suggest firstly that the vertical profile of HCHO can be treated as being distributed homogeneously over the region, thus lending itself to inversion using traditional radiative transfer models and the maximum a-posteriori inversion methodology. Secondly, the deficit of HCHO data within the literature, both for the Ohio River Valley itself but also globally, provides ample opportunity for future work in this field. As few profiles of HCHO have been measured vertically, determination of the vertical distribution of this species is an ideally application of more sophisticated physical/photochemical models.

8.2 Recommendations for Future Work

During the course of this research, shortcomings to the methodology were recognized. Several recommendations, including modifications to the instrument, application of emerging inversion methodologies, are given here. Firstly, the instrument itself, initially designed as a sequential, manually operated MAX-DOAS, would benefit greatly from the addition of automated spectral collection. For this automation to be implemented properly, any control software must assure that the correct saturation levels of the detector are achieved prior to collection. Secondly, rather than collecting singular spectra at each elevation angle sequentially, a CCD array should be implemented in place of the single row detector used in this research. In this manner, multiple telescopes, each set to a pre-defined elevation angle, could be used, and the light collected by each telescope directed to different regions of the CCD array by split fiber optic cables.

Addition of single, wide field-of-view telescope, coupled to a secondary CCD array, would serve as a UV-visible camera, capable of imaging the plume in question. Temporally resolved images of the plume could provide real time information on the shape and size of the plume being probed, and would be beneficial in flux estimates requiring plume volume estimates. Such an instrument would have a temporal resolution limited only by the strictures of properly collecting scattered solar radiation and not the adjustment of the elevation angle during sequential scans. Additional telescopes could also be positioned at different azimuth angles, an emerging technique in the retrieval of aerosol micro-physical properties using inversion methodologies⁷. An instrument of this type would be capable of collecting angularly resolved spectral data with excellent temporal resolution. The great deal of data which could theoretically be collected with such an instrument would lend itself to emerging retrieval methodologies which do not require the calculation of the large weighting function matrices which typify traditional inversion methods, including the maximum a-posteriori method used in this research.

It is suggested here that Markov Chain Monte Carlo methods, implemented previously for the inversion of oceanic circulation profiles¹¹¹ and satellite data¹¹², would be ideal for interpreting data collected by next-generation DOAS instruments. This method does not require the computationally intensive calculation of weighting function matrices, nor is the method prone to converging at a local minimum on the Chi-squared surface of the cost function, a common problem with traditional non-linear search algorithms¹¹³. Application of the Markov Chain Monte Carlo method, coupled to a three-dimensional radiative transfer model, could also be extended to the inversion of horizontally in-homogeneous species, in which case the calculation of a weighting

function matrix would be cumbersome. Future applications of the MAX-DOAS method to the monitoring of anthropogenic plumes should seek to improve the angular and temporal resolution of the instrument and take advantage of emerging inversion techniques, which can be quickly adapted to the inversion of profiles, plumes, and microphysical properties.

REFERENCES

1. G. Hönninger, C. V. Friedeburg, and U. Platt, *Atmospheric Chemistry and Physics*, 4, 231–254 (2004).
2. R. W. Sanders, S. Solomon, J. P. Smith, et al., *Journal of Geophysical Research*, 98, 7219-7228 (1993).
3. C. D. Rodgers, *Reviews of Geophysics and Space Physics*, 13, 609-624 (1976).
4. C. D. Rodgers, *Inverse Methods for Atmospheric Sounding: Theory and Practice*, World Scientific, Singapore, 2000.
5. B. Galle, C. Oppenheimer, A. Geyer, et al., *Journal of Volcanology and Geothermal Research*, 119, 241-254 (2002).
6. C. Lee, Y. J. Kim, H. Lee, et al. in *Advanced Environmental Monitoring*; Y. J. Kim, and U. Platt, Eds.; Springer, 2008.
7. T. Wagner, B. Dix, C. v. Friedeburg, et al., *Journal of Geophysical Research*, 109(2004).
8. S. E. Schwartz, *Science*, 243, 753-763 (1989).
9. B. F. Taubman, J. C. Hains, A. M. Thompson, et al., *Journal of Geophysical Research*, 111(2006).
10. S. E. Schwartz, and M. O. Andreae, *Science*, 272, 1121-1122 (1996).

11. C. Kern, T. Deutschmann, L. Vogel, et al., *Bulletin of Volcanology*, 71(2009).
12. D. J. Jacob, *Introduction to Atmospheric Chemistry*, Princeton University Press, Princeton, New Jersey, 1999.
13. M. Hausmann, U. Brandenburger, T. Brauers, et al., *Journal of Geophysical Research*, 102, 16011-16022 (1997).
14. B. J. Finlayson-Pitts, and J. N. Pitts Jr., *Chemistry of the Upper and Lower Troposphere*, Academic Press, San Diego, California, 2000.
15. J. H. Seinfeld, and S. N. Pandis, *Atmospheric Chemistry and Physics: From Air Pollution to Climate Change*, John Wiley and Sons, Inc., New York, 1998.
16. C. Hak, I. Pundt, S. Trick, et al., *Atmospheric Chemistry and Physics*, 5, 2881-2900 (2005).
17. COESA. NOAA, 1976, p 227.
18. S. Chandrasekhar, *Radiative Transfer*, Dover, New York, 1960.
19. L. C. Henyey, and J. L. Greenstein, *Astrophysics Journal*, 93, 70-83 (1941).
20. H. Iwabuchi, *Journal of the Atmospheric Sciences*, 63, 2324-2339 (2006).
21. A. Rozanov, V. Rozanov, M. Buchwitz, et al., *Advances in Space Research*, 36, 1015-1019 (2005).
22. A. Rozanov, V. Rozanov, and J. P. Burrows, *Journal of Quantitative Spectroscopy and Radiative Transfer*, 69, 491-512 (2001).
23. V. V. Rozanov, K.-U. Eichmann, R. de Beek, et al., *Advances in Space Research*, 29, 1831-1835 (2002).
24. A. Rozanov, V. Rozanov, and J. P. Burrows, *Journal of Geophysical Research*, 105, 22937-22943 (2000).

25. D. A. Skoog, F. J. Holler, and T. A. Nieman, *Principles of Instrumental Analysis*, Saunders College Publishing, 1971.
26. J. M. C. Plane, and N. Smith. in *Spectroscopy in Environmental Science*; R. J. H. Clark, and R. E. Hester, Eds.; John Wiley and Sons, Inc., 1995.
27. U. Platt. in *Air Monitoring by Spectroscopic Techniques*; M. W. Sigrist, Ed.; John Wiley and Sons, New York, 1994, p 27-84.
28. C. Frohlich, and G. E. Shaw, *Applied Optics*, 19, 1773-1775 (1980).
29. D. R. Bates, *Planetary and Space Science*, 32, 785-790 (1984).
30. U. Platt, D. Perner, and H. W. Patz, *Journal of Geophysical Research*, 84, 6329-6338 (1979).
31. U. Platt, and D. Perner, *Springer Ser. Opt. Sci.*, 39, 95-105 (1983).
32. J. M. C. Plane, and C.-F. Nien, *Rev. Sci. Instrum.*, 63, 1867-1876 (1992).
33. D. Perner, and U. Platt, *Geophysical Research Letters*, 6, 917-920 (1979).
34. J. D. Ingle, and S. R. Crouch, *Spectrochemical Analysis*, Prentice Hall, Upper Sadle River, New Jersey, 1988.
35. H. Okabe, *Photochemistry of Small Molecules*, Wiley-Interscience, New York, 1978.
36. H. Keller-Rudek, and G. K. Moortgat. Max-Planck-Institut für Chemie, Atmospheric Chemistry Division, Mainz, Germany.
37. B. A. Thompson, P. Harteck, and R. R. R. Jr., *Journal of Geophysical Research*, 68, 6431-6436 (1963).
38. S. Voigt, J. Orphal, and J. P. Burrows, *Journal of Photochemistry and Photobiology A: Chemistry*, 149, 1-7 (2002).

39. J. Stutz, E. S. Kim, U. Platt, et al., *Journal of Geophysical Research*, **105**, 14585-14592 (2000).
40. K. Bogumil, J. Orphal, T. Homann, et al., *Journal of Photochemistry and Photobiology A: Chemistry*, **157**, 167-184 (2003).
41. C. A. Cantrell, J. A. Davidson, A. H. McDaniel, et al., *Journal of Physical Chemistry*, **94**, 3902-3908 (1990).
42. T. Etzkorn, B. Klotz, S. Sørensen, et al., *Atmospheric Environment*, **33**, 525-540 (1999).
43. F. G. Simon, W. Schnieder, G. K. Moortgat, et al., *Journal of Photochemistry and Photobiology A: Chemistry*, **55**, 1-23 (1990).
44. D. M. Wilmouth, T. F. Hanisco, N. M. Donahue, et al., *Journal of Physical Chemistry*, **103**, 8935-8945 (1999).
45. S. Voigt, J. Orphal, K. Bogumil, et al., *Journal of Photochemistry and Photobiology A: Chemistry*, **143**(2001).
46. G. D. Greenblatt, J. J. Orlando, J. B. Burkholder, et al., *Journal of Geophysical Research*, **95**, 18577-18582 (1990).
47. G. W. Kattawar, A. T. Young, and T. J. Humphreys, *The Astrophysical Journal*, **243**, 1049-1057 (1981).
48. D. J. Fish, and R. L. Jones, *Geophysical Research Letters*, **22**, 811-814 (1995).
49. G. Barrefors, *The Science of the Total Environment*, **189/190**, 287-292 (1996).
50. S. R. Aliwell, M. V. Roozendaal, P. V. Johnston, et al., *Journal of Geophysical Research*, **107**, 10-11-10-20 (2002).

51. J. Stutz, R. Ackermann, J. D. Fast, et al., *Geophysical Research Letters*, **29**(2002).
52. P. K. Dasgupta, J. Li, G. Zhang, et al., *Environmental Science and Technology*, **39**, 4767-4783 (2004).
53. A. Heckel, A. Richter, T. Tarsu, et al., *Atmospheric Chemistry and Physics*, **5**, 909-918 (2005).
54. Y. Yoshii, H. Kuze, and N. Takeuchi, *Applied Optics*, **42**, 4362-4368 (2003).
55. Y. Xue, J. Niu, W. Liu, et al., *Japanese Journal of Applied Physics*, **39**, 622-627 (2000).
56. C. v. Friedeburg, I. Pundt, K.-U. Mettendorf, et al., *Atmospheric Environment*, **39**, 977-985 (2005).
57. B. J. Allan, J. M. C. Plane, H. Coe, et al., *Journal of Geophysical Research*, **107**(2002).
58. J. F. Noxon, R. B. Norton, and W. R. Henderson, *Geophysical Research Letters*, **5**, 675-678 (1978).
59. T. Wagner, C. Otten, K. Pfeilsticker, et al., *Geophysical Research Letters*, **27**, 3441-3444 (2000).
60. U. Platt, L. Marquard, T. Wagner, et al., *Geophysical Research Letters*, **24**, 1759-1762 (1997).
61. S. Solomon, A. L. Schmeltekopf, and R. W. Sanders, *Geophysical Research Letters*, **92**, 8311-8319 (1987).
62. A. Petritoli, F. Ravegnani, G. Giovanelli, et al., *Applied Optics*, **41**, 5593-5599 (2002).

63. T. Wagner, C. v. Friedeburg, M. Wenig, et al., *Journal of Geophysical Research*, 107(2002).
64. R. Sinreich, U. Frieß, T. Wagner, et al., *Faraday Discussions*, 130, 153-164 (2005).
65. P. Wang, A. Richter, M. Bruns, et al., *Atmospheric Chemistry and Physics*, 6, 329-338 (2006).
66. N. Bobrowski, G. Honninger, B. Galle, et al., *Nature*, 423, 273-276 (2003).
67. J. Stutz, and U. Platt, *Applied Optics*, 35, 6041-6053 (1996).
68. D. Goorvitch, *Journal of Quantitative Spectroscopy and Radiative Transfer*, 67, 253-257 (2000).
69. E. Hecht, *Optics*, Addison Wesley, San Francisco, California, 2002.
70. S. W. Smith, *The Scientist and Engineer's Guide to Digital Signal Processing*, California Technical Publishing, San Diego, California, 1997.
71. W. H. Press, S. A. Teukolsky, W. T. Vetterling, et al., *Numerical Recipes in C: The Art of Scientific Computing*, Cambridge University Press, Cambridge, 1988.
72. SCIATRAN. Institute of Remote Sensing, University of Bremen, Germany, Bremen, Germany, 2007.
73. M. van Roozendael, and C. Fayt, (2001).
74. H. K. Roscoe, D. J. Fish, and R. L. Jones, *Applied Optics*, 35, 427-432 (1996).
75. C. Caspar, and K. Chance. Third European Remote-Sensing Satellite Scientific Symposium: Space at the Service of Our Environment, The Netherlands, 1997, pp 609-614.
76. J. H. G. M. van Geffen, and R. F. v. Oss, *Applied Optics*, 42, 2739-2753 (2003).

77. J. F. Noxon, *Science*, 189, 547-549 (1975).
78. D. L. Albritton, A. L. Schmeltekoph, and R. N. Zare. in *Molecular Spectroscopy: Modern Research*; K. N. Rao, Ed.; Academic Press, New York, 1976, p 1-67.
79. OceanOptics. Ocean Optics, Incorporated, Dunedin, FL, 2007.
80. P. Pelikan, M. Ceppan, and M. Liska, *Applications of Numerical Methods in Molecular Spectroscopy*, CRC Press, Boca Raton, 1994.
81. M. Vountas, V. V. Rozanov, and J. P. Burrows, *Journal of Quantitative Spectroscopy and Radiative Transfer*, 60, 943-961 (1998).
82. K. V. Chance, and R. J. D. Spurr, *Applied Optics*, 36, 5224-5230 (1997).
83. M. Wenig, B. Jahne, and U. Platt, *Applied Optics*, 44, 3246-3252 (2005).
84. M. Hausmann, U. Brandenburger, T. Brauers, et al., *Applied Optics*, 36, 462-475 (1999).
85. J. Stutz, and U. Platt, *Applied Optics*, 36, 1105-1115 (1997).
86. N. Smith, J. M. C. Plane, C.-F. Nien, et al., *Atmospheric Environment*, 29, 2887-2897 (1995).
87. J. Harder, and G. H. Mount. in *Remote Sensing of Atmospheric Chemistry*; J. L. McElroy, and R. J. McNeal, Eds.; SPIE, 1991.
88. L. C. Marquard, T. Wagner, and U. Platt, *Journal of Geophysical Research*, 105, 1315-1327 (2000).
89. C. v. Friedeburg. in *Natural Sciences and Mathematics*; Ruperto-Carola University of Heidelberg, Heidelberg, Germany, 2003, p 244.

90. T. Wagner, J. P. Burrows, T. Deutschmann, et al., *Atmospheric Chemistry and Physics*, **7**, 1809-1833 (2007).
91. R. Schofield, B. J. Connor, K. Kreher, et al., *Journal of Quantitative Spectroscopy and Radiative Transfer*, **86**, 115-131 (2004).
92. C. Bruhl, and P. J. Crutzen. in *The Atmospheric Effects of Stratospheric Aircraft, Nasa Reference Publication 1993*, 1993, p 103-104.
93. M. J. Reider, and G. Kirchengast, *Radio Science*, **35**, 45-56 (2000).
94. A. N. Tikhonov, *Dokl. Acad. N.*, **151**, 501-504 (1963).
95. S. Twomey, *Journal of the Association for Computing Machinery*, **10**, 97-101 (1963).
96. M. Edmonds, R. A. Herd, B. Galle, et al., *Bulletin of Volcanology*, **65**, 578-586 (2003).
97. G. G. Salerno, M. R. Burton, C. Oppenheimer, et al., *Journal of Volcanology and Geothermal Research*, **181**, 141-153 (2009).
98. R. L. N. Yatavelli, J. K. Fahrni, M. Kim, et al., *Atmospheric Environment*, **40**, 6650-6665 (2006).
99. D. Perner, and U. Platt, *Geophysical Research Letters*, **7**, 1053-1056 (1980).
100. USEPA. U. S. Environmental Protection Agency Office of Air Quality Planning and Standards, Emissions Monitoring and Analysis Division, Research Triangle Park, North Carolina, 2004.
101. M. Hess, P. Koepke, and I. Schult, *Bulletin of the American Meteorological Society*, **79**, 831-844 (1998).

102. M. Kim, S. R. Deshpande, and K. C. Crist, *Atmospheric Environment*, **41**, 9231-9243 (2007).
103. B. A. Schichtel, R. B. Husar, S. R. Falke, et al., *Atmospheric Environment*, **35**, 5205-5210 (2001).
104. A. Horowitz, R. Meller, and G. K. Moortgat, *Journal of Photochemistry and Photobiology A: Chemistry*, **146**, 19-27 (2001).
105. O. C. Fleischmann, M. Hartmann, J. P. Burrows, et al., *Journal of Photochemistry and Photobiology A: Chemistry*, **168**, 117-132 (2004).
106. S.-C. Yoon, and J. Kim, *Atmospheric Environment*, **40**, 4328-4338 (2006).
107. N. V. Gillani, and W. E. Wilson, *Annals of the New York Academy of Sciences*, **38**, 276-296 (1980).
108. A. C. Vandaelea, A. Tsoulis, M. Carleerb, et al., *Environmental Pollution*, **116**, 193-201 (2002).
109. B. P. Wert, M. Trainer, A. Fried, et al., *Journal of Geophysical Research*, **108**, 8.1-8.14 (2003).
110. D. B. Millet, D. J. Jacob, S. Turquety, et al., *Journal of Geophysical Research*, **111**(2006).
111. I. W. McKeague, G. Nicholls, K. Speer, et al., *Journal of Marine Research*, **63**, 683-704 (2005).
112. H. Haario, M. Laine, M. Lehtinen, et al., *Journal of the Royal Statistical Society*, **66**, 591-607 (2004).
113. L. Tierney, *The Annals of Statistics*, **22**, 1701-1728 (1994).

